POLITECNICO DI MILANO

SCHOOL OF INDUSTRIAL AND INFORMATION ENGINEERING

DEPARTMENT OF ELECTRONICS, INFORMATION AND BIOENGINEERING

Master of Science in Biomedical Engineering

Dosimetric Impact of Geometric Distortions in an MRI-Only Proton Therapy Workflow for Extracranial Sites

Supervisor:	Prof. Guido BARONI
Co-supervisors:	Prof. Marco RIBOLDI
	Dr. Chiara PAGANELLI

Author:	Hatice Selcen DUMLU
ID:	894176

Academic Year 2019/2020

ACKNOWLEDGMENTS

Firstly, I would like to specially thank Professor Marco Riboldi for providing me with the opportunity of working on a project within his research group, giving me the chance to conduct this project in Ludwig Maximilians University (LMU), Munich, and dedicating a part of his research time always with pleasure for discussion. The door to his office was always open whenever I need his help and advice. With the freedom and enthusiasm, he gave to develop my project with my own ideas, always steering me in the right direction with his immense knowledge whenever I need, I really enjoyed working on this project and exploring more about my research topic.

I would like to thank Prof. Guido Baroni for accepting to join his lab group and providing this opportunity to me.

My special thanks also go to Dr. Chiara Paganelli, who enabled this project pointing out possible collaboration with LMU and supported with patience and attention since the beginning. I am grateful to her for always being open to discussion and support guiding me with her valuable advice. Even though being kilometers away, she was always keeping track of how I was proceeding and finding a solution for any problem that I have. I feel really lucky to know that she was always just a mail away.

This project would not have been possible without a collaboration with the LMU university clinic Großhadern. Particularly, I would like to thank Dr. Florian Kamp for supporting the clinical site of our work and Dr. Christopher Kurz and Dr. Guillaume Landry for their guiding advice.

Many thanks to Ms. Giorgia Meschini for sharing her knowledge and experience, helping me with learning about some concepts and also sharing with me a part of her research, which contributed a lot to my work.

Special thanks to my LMU family, colleagues, and friends for welcoming me in the chair. The friendly and supportive environment in the chair has been a big motivation during this period, making this experience very special and unforgettable for me. I would like to especially thank Liheng Tian for his willingness and patient to help me with the CERR program, Hans-Peter Wieser, Dr. Sebastian Mayer and Dr. Marco Pinto for their valuable advice and discussions.

Lastly, I would like to express my very profound gratitude to my family for their infinite support and whole-hearted care to make everything possible, being always an inspiration for me and motivating me in the hardest times from miles away. They are truly the touchstones of my life to become an independent and strong woman always dedicated to improvement. Without them, nothing would be indeed possible.

INDEX

FIGURE INDEX v

TABLE INDEX x

LIST OF ABBREVIATIONS xii

SUMMARY xiv

SOMMARIO xxi

1 INTRODUCTION TO PROTON THERAPY 1

1.1 Cancer 1

1.2 Conventional and Particle Radiation Therapy 3

1.3 Proton Therapy 6

1.4 Physical Characteristics of Proton Therapy 6

1.4.1 Stopping Power and LET 7

1.4.2 Relative Biological Effectiveness 8

1.5 Beam Delivery in Proton Therapy 8

Active Beam Scanning 9

1.6 Treatment Planning 9

1.6.1 Imaging and Planning 10

Image Registration 11

1.6.2 Margins 12

1.6.3 Dose Calculation 14

Monte Carlo Simulations 14

Pencil Beam Algorithms (PBA) 15

1.7 Uncertainties in Proton Therapy 17

1.8 Range Calculation Uncertainties in the Treatment Planning System 19

1.8.1 Inaccuracies arising from CT 19

1.8.2 Inaccuracies arising from Dose Calculation Algorithm 20

1.9 Discrepancies between Planned and Delivered Dose 21
1.9.1 Set-up Uncertainties 21
1.9.2 Organ Motion 21
Treatment Planning in Moving Districts 23
2 INTRODUCTION TO MRI IN RADIATION THERAPY 25
2.1 MRI in Radiation Therapy 25
2.2 MRI-Only Radiation Therapy 27
Synthetic CT Generation 29
2.3 Challenges in MRI-Only Radiation Therapy 31
2.3.1 System-Dependent Distortions 32
Gradient Nonlinearities 32
Magnetic Field Inhomogeneities 34
2.3.2 Patient-Dependent Distortions 34
Magnetic Susceptibility 35
Chemical Shift 36
3 AIM OF THE WORK 37
4 MATERIALS and METHODS 39
4.1 Image Datasets 39
4.1.1 4D CT/ MRI Digital Phantom 39
Generation of COMBAT Phantom 39
COMBAT Phantom in TP 42
4.1.2 4D CT Clinical Dataset 44
4.1.3 Processing of the Image Dataset before TP 44
4.2 Utilized Software 45
4.2.1 CERR 45
4.2.2 Raystation 47
4.2.3 Plastimatch 47

4.3 Treatment Plan Design 48
  4.3.1 Motion Compensation 49
  4.3.2 Target Volume Definition 49
    Beam-specific PTV Generation 50
    Sparing of OAR 51
  4.3.3 Field Set-Up and Dose Prescriptions 51
    Lung Cases 52
    Liver Cases 53
    Pancreas Cases 53
  4.3.4 Optimization 54
4.4 Simulation of Distortion Aspects of MRI-Only Workflow 55
  4.4.1 Quantification of Deformation Field 55
  4.4.2 Application of Deformation Field 57
4.5 Determination of Dosimetric Impact of Geometric Distortions 58
  4.5.1 Workflow 1 59
  4.5.2 Workflow 2 60
4.6 Assessment of Dosimetric Impact of Geometric Distortions 61
  4.6.1 Analysis on Target Structure 61
  4.6.2 Analysis on OAR 62
  4.6.3 Statistical Analysis 63
5 RESULTS & DISCUSSION 65
5.1 Comparison of Workflow 1 & Workflow 2 65
5.2 Results of Dosimetric Analysis on Phantoms 68
  Results in Target Structure 68
  Results in Organs at Risk 72
5.3 Results of Dosimetric Analysis on Thorax Clinical Data 74
  Results in Target Structure 74

Results in Organs at Risk 80
5.4 Results of Dosimetric Analysis on Abdominal Clinical Data 82
5.4.1 Liver Cases 82
Results in Target Structure 82
Results in Organs at Risk 84
5.4.2 Pancreas Cases 85
Results in Target Structure 85
Results in Organs at Risk 88
5.5 Statistical Analysis of the Results 89
5.5.1 Analysis on Target Structure 90
5.5.2 Analysis on Organs at Risk 91
5.6 Comparison of Target Results Among Different Regions 91
6 CONCLUSIONS 95
7 IMPROVEMENTS & FUTURE DEVELOPMENTS 99
8 Appendix A - Treatment Plan Simulations for COMBAT Phantoms 100
9 Appendix B - Treatment Plan Simulations for Lung Cancer Patients 102
10 Appendix C - Treatment Plan Simulations for Liver Cancer Patients 106
11 Appendix D – Treatment Plan Simulations for Pancreas Cancer Patients 108
12 BIBLIOGRAPHY 110

FIGURE INDEX

Figure 1 Depth Dose Profiles for Conventional and Particle Beam Radiation Therapy where the latter exhibits the Bragg peak, which permits a conformal treatment. (Fokas, Kraft, An & Engenhart-Cabillic, 2009)........xiv

Figure 2 Clinically used workflow of radiation therapy treatment planning and delivery in which the image registration of CT and MRI is involved (Chandarana, 2018)........xv

Figure 3 Workflow of the developed method for the quantification of the dosimetric impact of the system- and patient-induced geometric distortions in MRI in MRI-only radiation therapy........xviii

Figure 4 Normal vs. Cancer Cells. (World Health Organization, 2019a)........1

Figure 5 Depth Dose Profiles for Conventional and Particle Beam Radiation Therapy........5

Figure 6 Image Registration Workflow representation with the components of the registration algorithm. Retrieved from ‘Motion modelling techiques in radiotherapy: Deformable image registration’, by C. Paganelli, 2018, Lecture Notes, Politecnico di Milano........11

Figure 7 Demonstration of target volumes with their margins........13

Figure 8 Description of the geometric configuration considered in the dose calculation of an elementary beamlet where beam axis is represented as a straight line and the ray axis z^* as a dotted line.(Deplanques, 2015)........16

Figure 9 Sources of Range Uncertainties in Proton Therapy (McGowan, 2015)........18

Figure 10 Schematic representing the 4D CT Retro respective phase sorting workflow with the inputs of images from CT scan, respiration signal when the X-ray imaging signal is on (Vedam et al., 2003)........24

Figure 11 Differences in the soft-tissue contrast from MRI and CT scans in pancreas region in which arrow points the pancreatic head (A) CT scan, (B) T1-weighted gradient echo sequence of MR, (C) contrast administered MRI, (D) Diffusion-weighted MRI (Lee, E. S. & Lee, J. M., 2014)........25

Figure 12 Workflow of radiation therapy treatment planning and delivery when image registration of CT and MRI is involved (Chandarana, 2018)........26

Figure 13 Conventional CT image on the left and sCT image generated from T2 weighted MRI on the right (Gustafsson, 2019)........29

Figure 14 Representation of the spatial encoding gradient relationship with radial distance, dashed line shows the ideal linear gradient whereas solid line represents the non-linear gradient (Jamtheim Gustafsson, 2019) 33

Figure 15 CT images of lung phantom (a) axial plane (b) sagittal plane (c) coronal plane views 41

Figure 16 Corresponding MR images of lung phantom (a) axial plane (b) sagittal plane (c) coronal plane views 41

Figure 17 Upper abdomen phantom (a) axial plane (b) sagittal plane (c) coronal plane views 42

Figure 18 Manually contoured two lung phantoms which have tumors at different locations. The contours in the images are skin: in yellow, tumors: in blue, lungs: in green and spinal cord: in purple 43

Figure 19 Manually contoured (a) liver phantom (skin: in yellow, tumor: in blue, pancreas: in purple, liver: in green) and (b) Pancreas phantom (skin: in yellow, tumor: in orange, pancreas: in purple, liver: in green) 43

Figure 20 An example from the clinical dataset with the axial plane views of (a) lung case (b) liver case and (c) pancreas case where Internal Target Volumes (ITVs) are contoured in yellow in the images 44

Figure 21 User Interface of CERR Software Platform 46

Figure 22 CERR user interface for IMPT 46

Figure 23 User interface of Raystation TPS 47

Figure 24 Treatment planning workflow used in this study 48

Figure 25 Generation of the ITV (in blue) by the combination of 3 GTVs around end-exhale phase (in red, pink and green) 49

Figure 26 An example from the patient lung cases on which all the margins are shown. ITV: in yellow, CTV: in purple, bsPTV and OAR for beam 1: in light purple, bsPTV and OAR for beam 2: in green. Since OAR rings are generated from the bsPTVs, in the figure inner ring of OAR sparing rings represent bsPTVs 51

Figure 27 Construction sketch of the four modular phantom with total dimensions of (369×300×500) mm3. Each phantom subunit houses 5 distortion grids and can be filled with water. (Kroll, 2018) 56

Figure 28 CT images of a lung case on which deformation field representing the system-dependent and patient-dependent geometric distortions in MRI is applied (a) axial plane view (b) sagittal plane view (c) coronal plane view 58

Figure 29 Flow chart showing the treatment simulation steps for the undistorted and distorted CT scans 59

Figure 30 Flow chart of Workflow 1 in which the blocks in black frame show the operations common in both workflows and the other block shows analysis made in workflow 1 60

Figure 31 Flow chart of Workflow 2 in which the blocks in black frame show the operations common in both workflows and the blocks outside the frame show the operations applied for final analysis in workflow 2 61

Figure 32 Treatment Plan simulations with Workflow 2 on (a) lung phantom, (b) pancreas phantom and (c) clinical lung case.. 65

Figure 33 Dose distributions and field set-up representations for (a) Lung phantom with a tumor close to the soft tissue (b) Lung phantom with a tumor isolated in lung parenchyma (c) liver phantom and (d)pancreas phantom 69

Figure 34 Dose Volume Histograms with Dose on the x-axis and fractional volume on the y-axis of (a) Lung phantom with a tumor close to soft tissue (b)Lung phantom with an isolated tumor in lung parenchyma, (c)liver phantom and (d)pancreas phantom. Red line represents the DVH of undeformed phantom whereas blue line represents the DVH of deformed phantom 70

Figure 35 Box plot for the phantom dataset in which dose differences between undeformed and deformed target dose for $D_{2\%}$, $D_{98\%}$ and D_{mean} parameters, normalized with respect to the prescribed dose, are shown in red, blue and green respectively with their y-axis on the left and DHI difference is shown in black with its y-axis on the right 72

Figure 36 Box plot for lung clinical data in which dose differences between undeformed and deformed target dose for $D_{2\%}$, $D_{98\%}$ and D_{mean} parameters, normalized with respect to the prescribed dose, are shown in red, blue and green respectively with their y-axis on the left and DHI difference is shown in black with its y-axis on the right 76

Figure 37 Results for Lung Patient 1 with (a) Dose distribution for the deformed scan (b) DVH plot of undeformed, in red, and deformed scans, in blue with the x-axis representing the dose and y-axis representing the fractional volume.. 77

Figure 38 Results for Lung Patient 3 with (a) Dose distribution for the deformed scan (b) DVH plot of undeformed, in red, and deformed scans, in blue with the x-axis representing the dose and y-axis representing the fractional volume.. 77

Figure 39 Results for Lung Patient 6 with (a) Dose distribution for the deformed scan (b) DVH plot of undeformed, in red, and deformed scans, in blue with the x-axis representing the dose and y-axis representing the fractional volume 77

Figure 40 Results for Lung Patient 7 with (a) Dose distribution for the deformed scan (b) DVH plot of undeformed, in red, and deformed scans, in blue with the x-axis representing the dose and y-axis representing the fractional volume 78

Figure 41 Results for Lung Patient 8 with (a) Dose distribution for the deformed scan (b) DVH plot of undeformed, in red, and deformed scans, in blue with the x-axis representing the dose and y-axis representing the fractional volume 79

Figure 42 Results for Lung Patient 10 with (a) Dose distribution for the deformed scan (b) DVH plot of undeformed, in red, and deformed scans, in blue with the x-axis representing the dose and y-axis representing the fractional volume 79

Figure 43 Box plot for liver clinical data in which dose differences between undeformed and deformed target dose for $D_{2\%}$, $D_{98\%}$ and D_{mean} parameters, normalized with respect to the prescribed dose, are shown in red, blue and green respectively with their y-axis on 83

Figure 44 Results for Liver Patient 2 with (a) Dose distribution for the deformed scan (b) DVH plot of undeformed, in red, and deformed scans, in blue with the x-axis representing the dose and y-axis representing the fractional volume 83

Figure 45 Results for Liver Patient 3 with (a) Dose distribution for the deformed scan (b) DVH plot of undeformed, in red, and deformed scans, in blue with the x-axis representing the dose and y-axis representing the fractional volume 84

Figure 46 Box plot for pancreas clinical data in which dose differences between undeformed and deformed target dose for $D_{2\%}$, $D_{98\%}$ and D_{mean} parameters, normalized with respect to the prescribed dose, are shown in red, blue and green respectively with their y-axis 87

Figure 47 Results for Pancreas Patient 2 with (a) Dose distribution for the deformed scan (b) DVH plot of undeformed, in red, and deformed scans, in blue with the x-axis representing the dose and y-axis representing the fractional volume 87

Figure 48 Results for Pancreas Patient 3 with (a) Dose distribution for the deformed scan (b) DVH plot of undeformed, in red, and deformed scans, in blue with the x-axis representing the dose and y-axis representing the fractional volume 88

Figure 49 Rank Results of Kruskal-Wallis test performed on (a)$D_{98\%}$ normalized dose difference and (b) DHI difference results in different anatomical regions 93

Figure 50 Box plot of the (a) $D_{2\%}$ differences normalized with respect to the prescribed dose (b) $D_{98\%}$ differences normalized with respect to the prescribed dose (c) D_{mean} differences normalized with respect to the prescribed dose (d) DHI differences in different anatomical regions 94

Figure 51 Dose distribution of deformed scan (on the left) and DVH plot (on the right with red line belonging to undeformed scan and blue line belonging to deformed scan) of Lung phantom with tumor close to soft tissue 100

Figure 52 Dose distributions of deformed scans (on the left) and DVH plots (on the right with red line belonging to undeformed scan and blue line belonging to deformed scan) of Lung phantom with tumor isolated inside lung parenchyma, liver phantom and pancreas phantom (from top to bottom) 101

Figure 53 Dose distribution of deformed scan (on the left) and DVH plot (on the right with red line belonging to undeformed scan and blue line belonging to deformed scan) of Lung patient 1 102

Figure 54 Dose distributions of deformed scans (on the left) and DVH plots (on the right with red line belonging to undeformed scan and blue line belonging to deformed scan) of Lung Patients 2, 3 & 4 103

Figure 55 Dose distributions of deformed scans (on the left) and DVH plots (on the right with red line belonging to undeformed scan and blue line belonging to deformed scan) of Lung Patients 5, 6 & 7 104

Figure 56 Dose distributions of deformed scans (on the left) and DVH plots (on the right with red line belonging to undeformed scan and blue line belonging to deformed scan) of Lung Patients 8, 9 & 10 105

Figure 57 Dose distribution of deformed scan (on the left) and DVH plot (on the right with red line belonging to undeformed scan and blue line belonging to deformed scan) of Liver patient 1 106

Figure 58 Dose distributions of deformed scans (on the left) and DVH plots (on the right with red line belonging to undeformed scan and blue line belonging to deformed scan) of Liver Patients 2, 3 & 4 107

Figure 59 Dose distribution of deformed scan (on the left) and DVH plot (on the right with red line belonging to undeformed scan and blue line belonging to deformed scan) of Pancreas patient 1 108

Figure 60 Dose distributions of deformed scans (on the left) and DVH plots (on the right with red line belonging to undeformed scan and blue line belonging to deformed scan) of Pancreas Patients 2, 3 & 4 109

TABLE INDEX

Table 1 Treatment Plan Design Characteristics 52

Table 2 Target and OAR Dose Constraints for Lung Cases 53

Table 3 Target and OAR Dose Constraints for Liver Cases 53

Table 4 Target and OAR Dose Constraints for Pancreas Cases 54

Table 5 Assessment of dosimetric change measured on DVH parameters in CTV volume following Workflow 1 and Workflow 2 in the lung and pancreas phantoms and in the clinical lung case ($D_{2\%}$, $D_{98\%}$, D_{mean} parameters are normalized to the prescribed dose and given in percentage whereas DHI is given as absolute difference) 66

Table 6 Normalized differences in mean and maximum dose in the percentage of target prescribed dose in OARs in the lung and pancreas phantoms and in the clinical lung case following Workflow 1 and Workflow 2 67

Table 7 Differences of Dosimetric Parameters in CTV region between undeformed and deformed dose distributions belonging to the phantom data ($D_{2\%}$, $D_{98\%}$, D_{mean} parameters are normalized with respect to the prescribed dose) 69

Table 8 Normalized differences in mean and maximum dose in the percentage of target prescribed dose, 2 Gy, in organs at risk in the lung phantom 73

Table 9 Normalized differences in mean and maximum dose in the percentage of target prescribed dose, 2 Gy, in organs at risk in the liver phantom 73

Table 10 Normalized differences in mean and maximum dose in the percentage of target prescribed dose, 3 Gy, in organs at risk in the pancreas phantom 73

Table 11 Differences of dosimetric parameters in CTV region between undeformed and deformed dose distributions belonging to clinical lung cases ($D_{2\%}$, $D_{98\%}$, D_{mean} parameters are normalized with respect to the prescribed dose,2 Gy, and given in percentage) 75

Table 12 Normalized differences in mean and maximum dose in the percentage of target prescribed dose, 2 Gy, in organs at risk in the clinical lung data 81

Table 13 Differences of dosimetric parameters in CTV region between undeformed and deformed dose distributions belonging to clinical liver cases ($D_{2\%}$, $D_{98\%}$, D_{mean} parameters are normalized with respect to the prescribed dose, 2 Gy, and given in percentage) 82

Table 14 Absolute differences in mean and maximum dose in the percentage of target prescribed dose, 2 Gy, in organs at risk in the clinical liver data 85

Table 15 Differences of Dosimetric Parameters in CTV region between undeformed and deformed dose distributions belonging to clinical pancreas cases ($D_{2\%}$, $D_{98\%}$, D_{mean} parameters are normalized to the prescribed dose,3 Gy, and given in percentage) 86

Table 16 Normalized differences in mean and maximum dose in the percentage of target prescribed dose, 3 Gy, in organs at risk in the clinical pancreas data 89

Table 17 Kruskal-Wallis test results for CTV dosimetric parameters performed on undeformed and deformed dose results in different regions where $D_{2\%}$, $D_{98\%}$, D_{mean} parameters are normalized with respect to the prescribed dose 90

Table 18 Wilcoxon signed-rank test results for CTV dosimetric parameters performed on undeformed and deformed pairs, where $D_{2\%}$, $D_{98\%}$, D_{mean} parameters are normalized with respect to the prescribed dose, on single dataset comprising of 3 investigated anatomical regions 91

Table 19 Kruskal-Wallis test results for target dosimetric parameters performed on differences of undeformed and deformed dose results in different regions where $D_{2\%}$, $D_{98\%}$, D_{mean} parameters are normalized with respect to the prescribed dose 92

Table 20 Treatment planning design parameters for phantoms 100

Table 21 Treatment planning design parameters for lung cancer patients 102

Table 22 Treatment planning design parameters for liver cancer patients 106

Table 23 Treatment planning design parameters for pancreas cancer patients 108

LIST OF ABBREVIATIONS

4D CT: 4-Dimensional Computed Tomography

B_0: Main Static Magnetic Field

B-field: Magnetic Field

bsPTV: beam-specific PTV

CERR: Computational Environment for Radiological Research

COMBAT: 4D CT/MRI Breathing Anthropomorphic Thorax

CT: Computed Tomography

CTV: Clinical Target Volume

$D_{2\%}$: Near-Maximum Dose

$D_{98\%}$: Near-Minimum Dose

DHI: Dose Homogeneity Index

DIR: Deformable Image Registration

DM: Distal Margin

$D_{\text{max, target}}$: Maximum Dose to Target

D_{max}: Maximum Dose

D_{mean}: Mean Dose

$D_{\text{min, target}}$: Minimum Dose to Target

DOF: Degrees of Freedom

DVF: Deformation Vector Field

DVH: Dose Volume Histogram

FLASH: Fast Low Angle Shot

FOV: Field of View

GTV: Gross Tumor Volume

Gy: Gray

HU: Hounsfield Unit

ICRU: International Commission on Radiation Units & Measurements

IGRT: Image Guided Radiotherapy

IMPT: Intensity Modulated Proton Therapy
ITV: Internal Target Volume
LET: Linear Energy Transfer
MC: Monte Carlo
MRI: Magnetic Resonance Imaging
NSCLC: Non-Small Cell Lung Cancer
OAR: Organs at Risk
PBA: Pencil Beam Algorithm
PET: Positron Emission Tomography
PM: Proximal Margin
PTCOG: Particle Therapy Co-operative Group
PTV: Planning Target Volume
RBE: Relative Biological Effectiveness
RIR: Rigid Image Registration
rsp: Relative Stopping Power
SCLC: Small Cell Lung Cancer
SFUD: Single Field Uniform Dose
SI: Superior-Inferior
SOBP: Spread-Out Bragg Peak
TCP: Tumor Control Probability
TP: Treatment Planning
TPS: Treatment Planning System
TrueFISP: Fast Imaging with Steady State Precession
VIBE: Volumetric Interpolated Breath-hold Examination
WET: Water Equivalent Thickness
XCAT: Extended Cardiac-torso

SUMMARY

Radiation therapy uses high doses of radiation to shrink the tumors and kill cancer cells by the destruction of the genetic material (DNA) of the tumor irreparably. Particle therapy, i.e. radiation therapy with charged particle beams, is an emerging technique in the field of cancer treatment exhibiting greater radiobiological effectiveness. Charged particles have different dosimetric characteristics than photons used in conventional radiotherapy. As demonstrated in Figure 1, while in conventional radiation, energy deposition takes place with an exponential decrease after a short build-up region with increasing depth in tissue, charged particle beams have a depth-dose profile characterized by a narrow peak, which is called as 'Bragg peak', at the end of their path. The depth-dose profile of the charged particle beams permits to deliver a more conformal dose to the target while sparing the organs at risk.

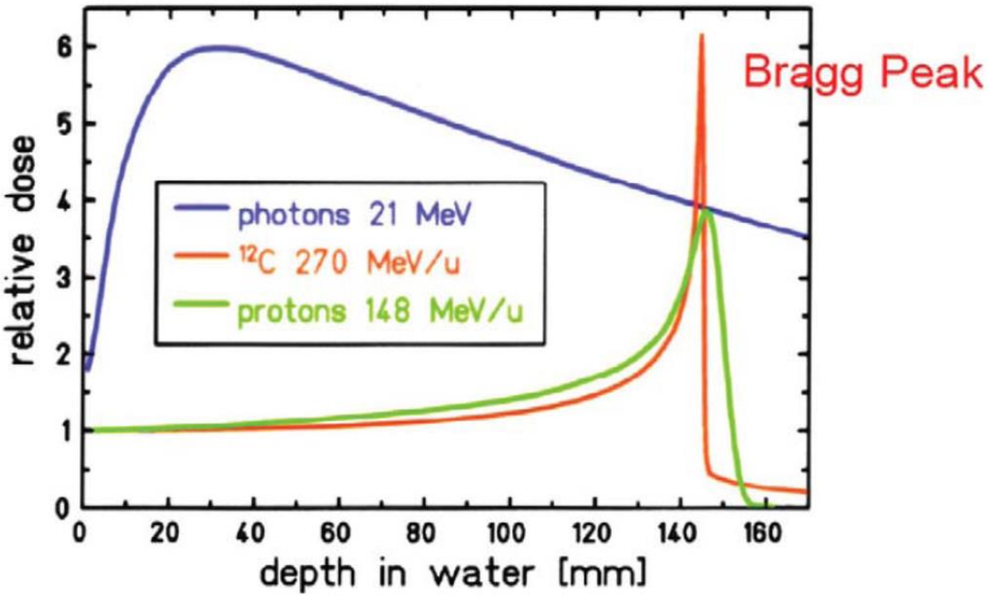

Figure 1 Depth Dose Profiles for Conventional and Particle Beam Radiation Therapy where the latter exhibits the Bragg peak, which permits a conformal treatment. (Fokas, Kraft, An & Engenhart-Cabillic, 2009*).*

In order to meet the prescribed dose distribution, the beam has to be correctly modulated in both shape (linked to the dose-target volume) and intensity (dose prescription). Providing greater flexibility for the target volume and reducing the dose in the nearby healthy tissues, active beam scanning is the commonly used beam delivery technique in the modern treatment facilities. It enables the delivery of Intensity Modulated Proton Therapy (IMPT), which renders it possible to concentrate the dose in the target volume.

For the delivery of a conformal dose to the target, while ensuring that the surrounding structures are exposed to a limited amount of dose within constraints, treatment planning is required to be patient-specific. Treatment planning includes the steps of acquisition of patient imaging data, contouring of tumor and organs, selection of treatment parameters, i.e. margins to manage uncertainties arising from range calculation, motion and set-up errors, radiation dose, and beam geometry, dose calculation, optimization and verification of the planned treatment. The main imaging modalities used in treatment planning include high resolution anatomical imaging techniques, which are Computed Tomography (CT), and Magnetic Resonance Imaging (MRI). Since MRI is better suited for contouring of the tumor volume with a superior soft tissue contrast visualization and CT is required for the accurate radiation dose computation, in the current clinical practice, radiation therapy treatment planning is based on a hybrid workflow, which is demonstrated in Figure 2.

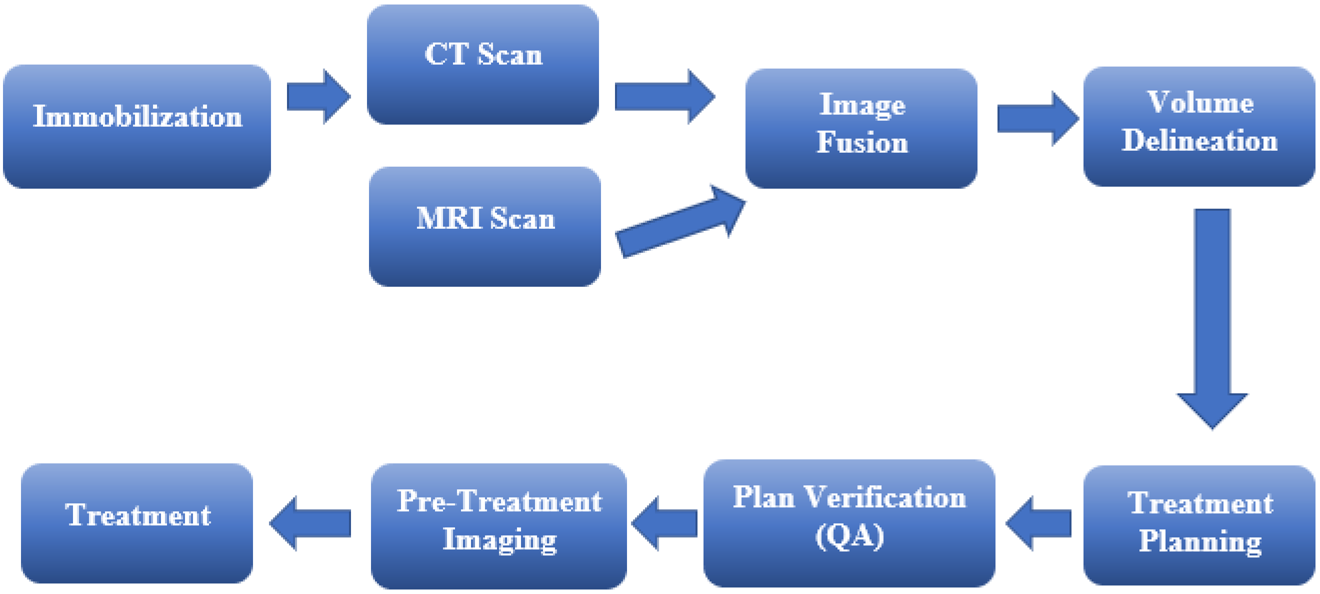

Figure 2 Clinically used workflow of radiation therapy treatment planning and delivery in which the image registration of CT and MRI is involved (Chandarana, 2018)

Combination of CT and MRI images by the image registration of these two modalities into a common geometric reference frame would allow to have both a good soft tissue contrast for accurate contouring and electron density (for photon therapy) or proton stopping power ratio relative to water (for proton therapy), which enables the dose calculation for treatment planning. However, CT/MRI hybrid workflow has some limitations arising from systematic spatial uncertainties due to image registration, exposure of the patient to ionizing radiation in the CT acquisition, inter-scanner differences between the two imaging sessions and overall cost considerations. Therefore, techniques excluding the CT from the workflow have been introduced which are referred to as ‘MRI-only’ or ‘MRI-based’ or ‘MRI-alone’ radiation therapy. As the image intensity and contrast in MRI is not directly related to electron density and relative stopping power ratio required for treatment planning, obtaining this information from the MRI images requires conversion process and the new images providing this information are referred as ‘synthetic CT’, ‘pseudo-CT’ or ‘substitute CT’.

MRI-only treatment planning would bring several advantages compared to conventional hybrid workflow, by the elimination of the image registration, patient exposure to ionizing radiation, and two different imaging sessions. Moreover, it would provide a cost-effective solution and help to save time, which is reported to be approximately 15 minutes (Tyagi et al., 2017). Furthermore, MRI-only radiation therapy has motivated the development of an in-room MRI-guidance system for real-time tumor tracking being a promising advance for the MRI guided radiation therapy. However, MRI introduces system-dependent and patient-dependent geometric distortions, which arise from the imperfections in the MRI-hardware and variations in magnetic properties of the patient under scan, respectively. While MRI system-induced geometric distortions can mainly stem from nonlinearities in spatial encoding gradients and inhomogeneities in the main static magnetic field (B_0), patient-induced geometric distortions stem from magnetic susceptibility and chemical shift effects.

MRI system- and patient-induced geometric distortions in the radiotherapy treatment planning images can cause radiation dose calculations on incorrect assumption or treatment delivery in wrong breathing. Thus, these would lead to insufficient irradiation of the tumor and over-dosage in normal tissues. In this work, a study in collaboration with Ludwig-Maximilians University (LMU) Munich has been conducted to quantify the dosimetric effect of geometric distortions arising from MRI in MRI-only workflow in Intensity Modulated Proton Therapy (IMPT). In order to simulate the distortion aspects in an MRI-only workflow and evaluate its impact on the planned dose distribution, an approach is developed in which CT images are distorted using an MRI displacement map and treatment planning is made on these CT images. The displacement map demonstrating the spatial distortion artifacts in MR-images, represented as deformation vector fields (DVFs), has been experimentally quantified using a self-designed distortion phantom (Kroll, 2018). In this study, deformation vector fields comprising of gradient nonlinearities, static magnetic field inhomogeneities and patient susceptibility variations for the FLASH (Fast Low Angle Shot) sequence have been used. The quantified DVF demonstrates a maximal mean landmark deformation per image slice of up to 3 mm in slice selection direction at a slice shifted 105 mm away from the isocenter and mean in-slice landmark deformation below 1 mm.

The analysis for this work has been applied to 4D imaging (3D+time) as it represents the current clinical standard for the treatment of organs subject to respiratory motion in the thoracoabdominal site. Specifically, a dataset comprising of a digital breathing 4D-CT/MRI phantom and 4D-CT clinical scans of the thoracoabdominal site in 18 patients has been considered. The 4D CT/MRI Breathing Anthropomorphic Thorax (CoMBAT) phantom developed by Paganelli et al. (2017) based on the extended cardiac-torso (XCAT) phantom is used to demonstrate the dosimetric changes on a realistic human model and provide a reference from which to evaluate and verify the results in clinical data. The thoracoabdominal clinical dataset consists of 4D-CT scans of 10 lung cancer patients, 4 liver cancer patients, and 4 pancreas cancer patients. Each patient data includes 10 respiratory phase volumes, and an average CT volume, which represents the mean position of the anatomy during the breathing cycle to be used for treatment planning. Since the extracranial sites are of concern in this study, usage of 4D CT data has played a crucial role in motion compensation through the gating technique (i.e. planning and treatment in a specific respiratory phase). In the treatment plan design, in order to simulate a possible gating treatment at the exhale phase, which is the respiratory phase where the tumor position is more stable and repeatable, three GTVs around the end-exhale phase are combined to generate the Internal Target Volume (ITV). After the ITV generation, the Clinical Target Volume (CTV) is generated by isotropic expansion of ITV in order to account for the neighboring microscopic subclinical malignant pathologies around the tumor. However, the designed treatment plans are optimized on the Planning Target Volumes (PTV). Since the isotropic margin expansion approaches in the PTV generation cannot adequately account for the changes in tissue densities along the beam path due to range uncertainties in proton therapy, a beam-specific PTV (bsPTV) is generated. In the treatment plan design, sparing of the organs at risk (OARs) around the target volume is ensured by the generation of an OAR sparing ring based on the isotropic expansion of bsPTV margin. After the steps of beam arrangement and target volume and OAR sparing ring definition, dose calculation and optimization is computed. The simulated treatment plan is chosen if it satisfies the dose constraints in the target volume and OARs.

A method has been developed in this study to determine and quantify the dosimetric uncertainties arising from the geometric distortions in MRI-only proton therapy without any need for synthetic CT generation. In order to simulate the geometric distortions, a deformation vector field is applied to the CT images creating the distorted CT images. A schematic representation of the implemented method is given in Figure 3.

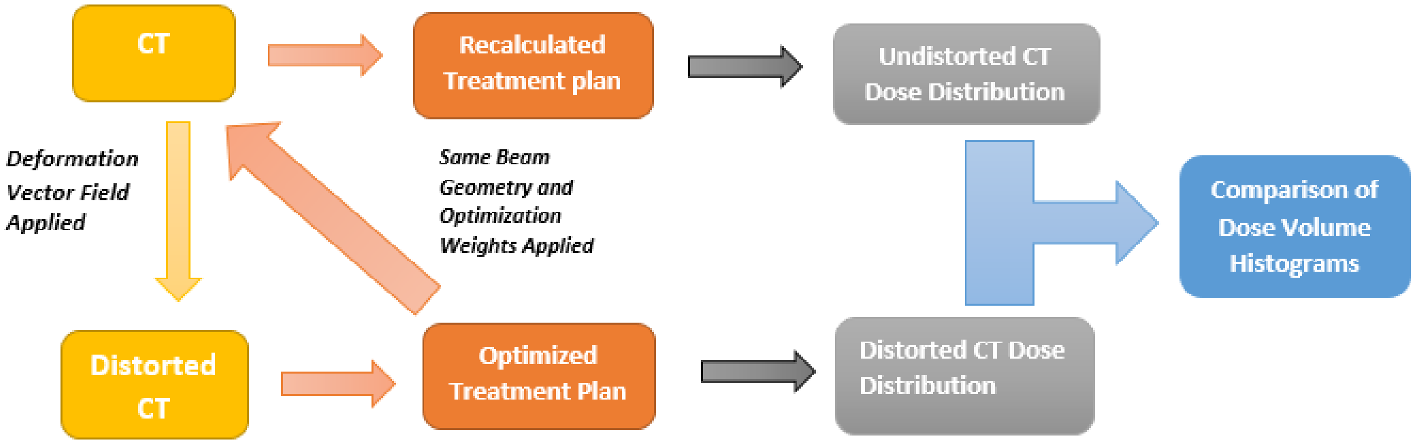

Figure 3 Workflow of the developed method for the quantification of the dosimetric impact of the system- and patient-induced geometric distortions in MRI in MRI-only radiation therapy

In order to obtain comparable dose distributions for undistorted and distorted CTs, which allows determining the dosimetric impact of geometric distortions in MRI-only workflow, the treatment is designed with the same beam angles, proton beam energies and dose prescriptions for both scans. The treatment plans are designed and optimized firstly on the distorted CT scans, in order to simulate an MRI-only workflow. The treatments are separately optimized for each field based on the beam specific PTV as the target, thus obtaining Single Field Uniform Dose (SFUD) for each field and the treatment isocenter is defined as the isocenter of the bsPTV. The final dose distribution for the distorted CT, denoted as $D_{distorted}$, is obtained by taking the average of the dose distributions generated from each single field optimization. The created treatment plan design is applied and dose is recalculated in undistorted CT using the same beam geometry and beam weights calculated in the optimization of distorted CT. Like in $D_{distorted}$ calculation, the final dose distribution for the undistorted CT, denoted as $D_{undistorted}$, is the average of the dose distributions generated from each single field optimization. Undistorted and distorted CT final dose distributions are analyzed and compared based on their dose volume histogram (DVH), which is a histogram used as a plan evaluation tool in the radiation therapy treatment planning relating the radiation dose to tissue volume. The dosimetric analysis is carried out on CTV volume, and OARs in the final dose distribution. The analysis on CTV volume is performed in terms of DVH parameters of near-minimum dose, denoted as $D_{2\%}$, near-maximum dose, denoted as $D_{98\%}$, mean dose, D_{mean}, and Dose Homogeneity Index (DHI). In the analysis of OARs, mean dose, D_{mean}, and maximum dose, D_{max}, parameters are evaluated. The dosimetric results in phantoms and clinical data are found to be in agreement with each other in each body region studied in the scope of this work. Thus, the conclusions on the dosimetric impact reached in a clinical dataset are confirmed by the phantom, which stands as a gold standard.

As a result of the analysis performed on the final dose distributions of the clinical dataset, the dosimetric differences between undeformed and deformed dose pairs were found to go up to 0.8%, 21.5%, and 3.750% of the prescribed dose in terms of the dose parameters $D_{2\%}$, $D_{98\%}$ and D_{mean}, respectively. For the DHI parameter, the difference was found to have a maximum value of 0.132. In order to determine if the differences between the paired undeformed and deformed dose are statistically significant, Wilcoxon signed-rank test was performed on the clinical dataset comprising of all of the studied regions. According to this test, the paired undeformed and deformed dosimetric results were found to be statistically different in the target structure dosimetric parameters at the 5% significance level (i.e. 95% confidence), which verify that the system- and patient-induced geometric distortions lead to statistically significant dosimetric changes in the target structure. Conversely, dosimetric differences were negligible in OARs and did not result significant. This result confirms the advantage of proton therapy in the delivery of conformal dose to the target and sparing of surrounding tissues over conventional radiotherapy.

As regards the results in the specific anatomical sites, the dosimetric impact of geometric distortions in the CTV structure was found to be the smallest in the abdomen regions rather than the thorax. Indeed, Kruskal-Wallis test performed on the difference of undeformed and deformed target dose (normalized with respect to the prescribed dose in the $D_{2\%}$, $D_{98\%}$, and D_{mean} dose parameters) has concluded that the difference dose in the lung has statistically different dose distributions than liver and pancreas in terms of $D_{98\%}$ and DHI parameters. Specifically, we noticed that geometric distortions cause smaller dosimetric changes in the target structure for the tumors located close to or covered by the soft tissue. This is not the case for the lung site, where the tumor can be either close to soft tissue or isolated inside the lung parenchyma. In this latter case, higher dose differences were found, due to the fact that the beam travels on a path with high density variations in the lung region and thus potentially leading to the miss of the target. Therefore, in these cases, where the tumor is isolated from the soft tissue, it is suggested to avoid MRI-only proton therapy workflow. Excluding these cases, in the clinical scenario, the differences found between the undeformed and deformed target dose are small with respect to the prescribed dose.

The work described in this thesis was aimed to quantify the dosimetric impact of geometric distortions in MR imaging in an MRI-only proton therapy workflow in the extracranial sites. The results of the study, therefore, suggests the potential applicability of MRI-only proton therapy, provided that MRI distortions do not cause clinically relevant dosimetric variations when the tumor is close to or covered by the soft tissue. As the studies based on MRI-only proton therapy workflow in the thoracoabdominal regions are limited in the literature, we put forward this study as a starting point for further research to carry MRI-only proton therapy workflow in the extracranial sites into clinical practice. An analysis on a larger dataset including different body regions with more samples would definitely contribute to strengthening our findings in order to take an MRI-only workflow safely into the clinical practice. Lastly, in order to consider all the real-life application aspects of MRI-only proton therapy and test the clinical applicability, this study requires to be continued with a further analysis including the uncertainties introduced by the synthetic CT generation methods in the workflow.

SOMMARIO

La radioterapia utilizza alte dosi di radiazioni per ridurre i tumori e neutralizzare le cellule tumorali mediante la distruzione irreparabile del materiale genetico (DNA). La terapia con particelle, ovvero la radioterapia con fasci di particelle cariche accelerate, è una tecnica emergente in campo oncologico in virtù della maggiore efficacia radiobiologica. Le particelle cariche hanno caratteristiche dosimetriche diverse rispetto ai fotoni utilizzati nella radioterapia convenzionale. Come mostrato in Figura 1, mentre nella radiazione convenzionale la deposizione di energia avviene con una diminuzione esponenziale con una profondità crescente nei tessuti dopo un breve incremento iniziali, i fasci di particelle cariche hanno un profilo di dose-profondità caratterizzato da un picco stretto, che è chiamato "picco di Bragg", alla fine del loro percorso. Il profilo della dose di profondità dei fasci di particelle cariche consente di erogare una dose più conforme al bersaglio risparmiando gli organi a rischio.

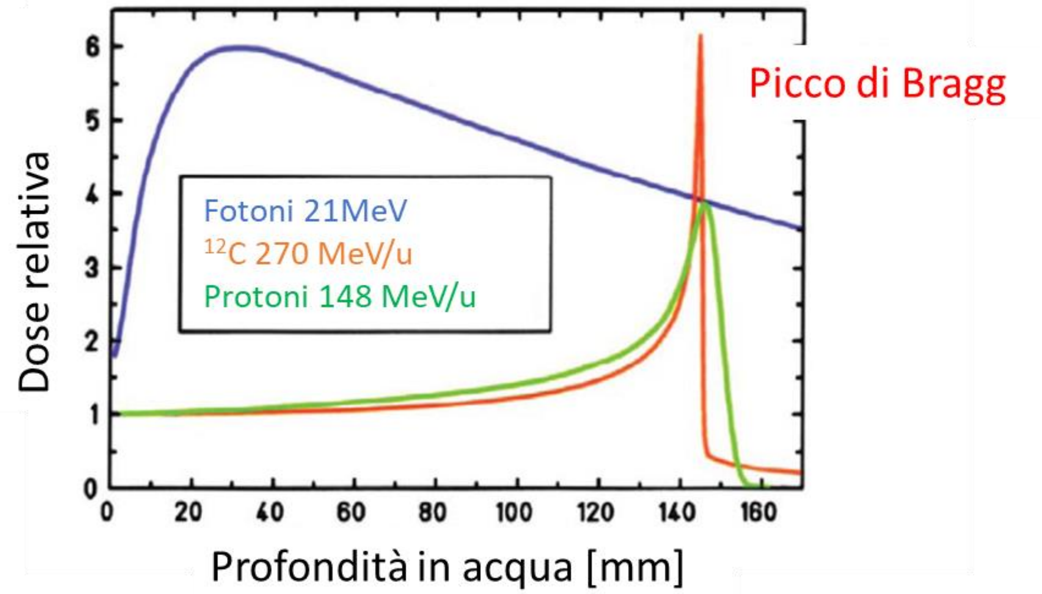

Figura 1 Profile della distrobuzione di dose per radioterapia convenzionale (photons) e terapia con particelle, che evidenzia il cosiddetto picco di Bragg, che permette l'erogazoine di trattamenti piú precisi. kas, Kraft, An & Engenhart-Cabillic, 2009).

Al fine di soddisfare la distribuzione della dose prescritta, il fascio deve essere correttamente modulato sia nella forma (collegata al volume target) sia nell'intensità (prescrizione della dose). Fornendo una maggiore flessibilità per il volume target e riducendo la dose nei tessuti sani vicini, la scansione attiva del fascio è la tecnica di erogazione del fascio comunemente usata nei centri più moderni per il trattamento. La scansione attiva consente l'erogazione della terapia protonica modulata per intensità (IMPT), che rende possibile concentrare la dose nel volume target.

Per l’erogazione di una dose conforme al target, garantendo nel contempo che le strutture circostanti siano esposte a una quantità limitata di dose, è necessario che la pianificazione del trattamento sia specifica per ogni paziente. La pianificazione del trattamento comprende le fasi di acquisizione dei dati di imaging del paziente, la segmentazione del tumore e degli organi, la selezione dei parametri di trattamento, ovvero i margini per gestire le incertezze derivanti dal calcolo della profonditá di penetrazione, gli errori di movimento e di set-up geometrico, la dose di radiazione e la geometria del fascio, il calcolo della dose, l’ottimizzazione e la verifica del trattamento pianificato. Le principali modalità di imaging utilizzate nella pianificazione del trattamento includono tecniche di imaging anatomico ad alta risoluzione, che sono la tomografia computerizzata (CT) e la risonanza magnetica (MRI). Poiché la risonanza magnetica è più adatta per la segmentazione del volume del tumore con una visualizzazione del contrasto dei tessuti molli superiore e la TC è necessaria per il calcolo accurato della dose di radiazioni, nella pratica clinica attuale, la pianificazione del trattamento di radioterapia si basa su un approccio ibrido, come mostrato Figura 2.

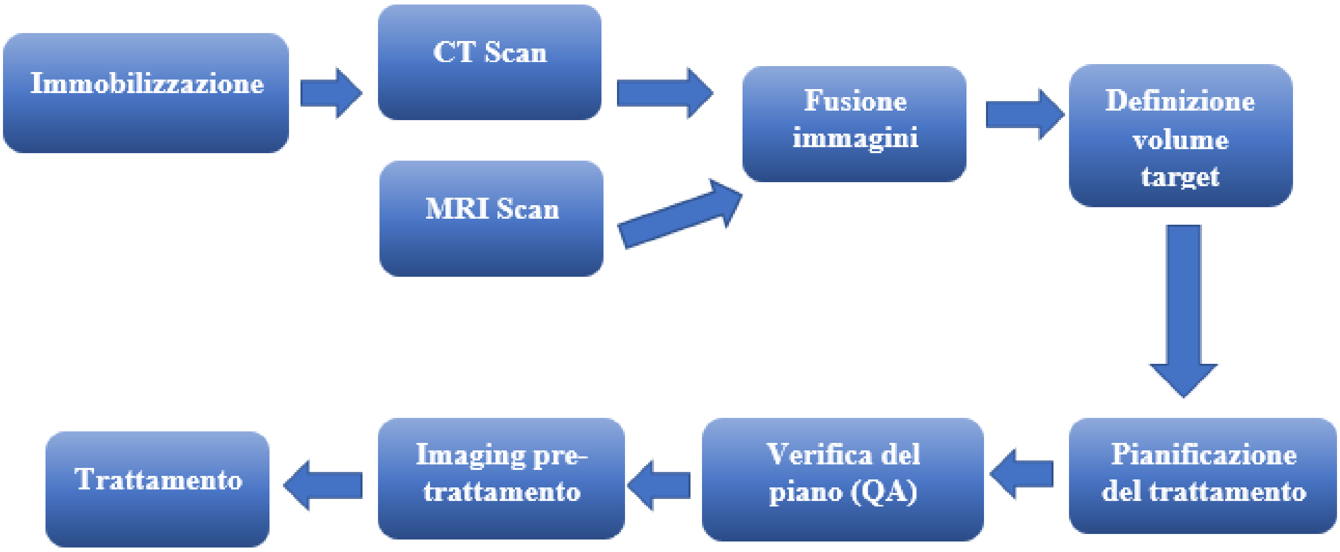

Figura 2 Schema a blocchi per la pianificazione e il trattamento in radioterapia, nel quale é prevista la registrazione di immagini CT ed MRI(Chandarana, 2018)

La combinazione di immagini CT e MRI, mediante la registrazione delle immagini in un sistema di riferimento geometrico comune, consentirebbe di avere sia un buon contrasto dei tessuti molli per contorni accurati che informazioni sulla densità di elettroni (per radioterapia convenzionale a fotoni) o sulla capacitá di arresto dei protoni relativo all'acqua (per la terapia a protoni), che consente il calcolo della dose per la pianificazione del trattamento. Tuttavia, l’approccio ibrido CT / MRI presenta alcune limitazioni derivanti da incertezze spaziali sistematiche dovute alla registrazione di immagini, esposizione del paziente a radiazioni ionizzanti nell'acquisizione di CT, differenze inter-scanner tra le due sessioni di imaging e considerazioni sui costi complessivi. Pertanto, sono state introdotte tecniche che escludono la CT dal flusso di lavoro, che sono denominate radioterapia "'MRI-only' o 'MRI-based' o 'MRI-alone'. Poiché l'intensità e il contrasto dell'immagine nella risonanza magnetica non sono direttamente correlati alla densità elettronica e alla capacitá di arresto dei protoni richiesta per la pianificazione del trattamento, l'ottenimento di queste informazioni dalle immagini MRI richiede un processo di conversione e le nuove immagini che forniscono tali informazioni sono denominate "CT sintetica", 'pseudo CT' o 'CT sostitutiva'.

La pianificazione del trattamento con sola risonanza magnetica porterebbe diversi vantaggi rispetto ad un approccio ibrido convenzionale, eliminando la registrazione dell'immagine, l'esposizione del paziente alle radiazioni ionizzanti e due diverse sessioni di imaging. Inoltre, fornirebbe una soluzione economica e aiuterebbe a risparmiare tempo, quantificabile in circa 15 minuti (Tyagi et al., 2017). Inoltre, la radioterapia MRI-only ha motivato lo sviluppo di sistemi di monitoraggio del tumore in tempo reale basati su MRI, rappresentando un'innovazione molto promettente per la radioterapia guidata da immagini MRI. Tuttavia, la risonanza magnetica introduce distorsioni geometriche dipendenti dal sistema e dipendenti dal paziente, che derivano dalle imperfezioni dell'hardware MRI e dalle variazioni delle proprietà magnetiche del paziente sottoposto a scansione, rispettivamente. Mentre le distorsioni geometriche indotte da MRI possono derivare principalmente dalle non linearità nei gradienti di codifica spaziale e dalle disomogeneità nel campo magnetico statico principale (B0), le distorsioni geometriche indotte dal paziente derivano dalla suscettività magnetica e dagli effetti di chemical shift.

Le distorsioni geometriche indotte dal sistema MRI e dal paziente nelle immagini di pianificazione del trattamento di radioterapia possono causare calcoli della dose di radiazioni in caso di assunzione errata o erogazione del trattamento in una fase erronea del respiro. Pertanto, ciò comporterebbe un'irradiazione insufficiente del tumore e un sovradosaggio nei tessuti sani. In questo lavoro, è stato condotto uno studio in collaborazione con la Ludwig-Maximilians University (LMU) di Monaco per quantificare l'effetto dosimetrico delle distorsioni geometriche derivanti dalla risonanza magnetica in un approccio MRI-only per Intensity Modulated Proton Therapy (IMPT). Al fine di simulare gli aspetti di distorsione in un approccio basato solo su MRI e valutare il suo impatto sulla distribuzione della dose pianificata, é stato sviluppato un approccio in cui le immagini CT vengono distorte utilizzando una quantificazione delle distorsioni in risonanza, e la pianificazione del trattamento viene effettuata su queste immagini CT. La mappa di spostamento che mostra gli artefatti della distorsione spaziale nelle immagini MRI, rappresentati come campi vettoriali di deformazione (DVF), è stata quantificata sperimentalmente usando un fantoccio sviluppato ad-hoc (Kroll, 2018). In questo studio, sono stati utilizzati campi vettoriali di deformazione che comprendono nonlinearità del gradiente, disomogeneità del campo magnetico statico e variazioni di suscettibilità del paziente per la sequenza FLASH (Fast Low Angle Shot). Il DVF quantificato mostra una deformazione media massima fino a 3 mm nella direzione di selezione della fetta in corrispondenza di una fetta spostata a 105 mm di distanza dall'isocentro e una deformazione media nella fetta inferiore a 1 mm.

L'analisi per questo lavoro è stata applicata a immagini 4D (3D+tempo) poichè rappresentano il corrente standard clinico per il trattamento di organi soggetti a movimento respiratorio nel distretto toraco-addominale. In dettaglio, un set di dati comprendente un fantoccio digitale 4D-CT / MRI e scansioni cliniche 4D-CT del sito toraco-addominale in 18 pazienti è stato utilizzato. Il fantoccio 4D CT / MRI Breath Anthropomorphic Thorax (CoMBAT) sviluppato da Paganelli et al. (2017), basato sul fantoccio XCAT, viene utilizzato per dimostrare i cambiamenti dosimetrici su un modello umano realistico e fornire un riferimento rispetto al quale valutare e verificare i risultati nei dati clinici. L'insieme di dati clinici toraco-addominali è costituito da scansioni 4D-CT di 10 pazienti con carcinoma polmonare, 4 pazienti con carcinoma epatico e 4 pazienti con carcinoma del pancreas. I dati di ciascun paziente includono 10 volumi della fase respiratoria e un volume CT medio, che rappresenta la posizione media dell'anatomia durante il ciclo respiratorio da utilizzare per la pianificazione del trattamento. Poiché i siti extracranici sono oggetto specifico di questo studio, l'uso di dati CT 4D ha svolto un ruolo cruciale nella compensazione del movimento attraverso la tecnica di gating (ovvero pianificazione e trattamento in una specifica fase respiratoria). Nella progettazione del piano di trattamento, al fine di simulare un possibile trattamento di gating in una specifica fase di fine espirazione, che è la fase respiratoria in cui la posizione del tumore è più stabile e ripetibile, tre GTV attorno a tale fase vengono combinati per generare il volume target interno (ITV). Dopo la generazione di ITV, il volume target clinico (CTV) viene generato dall'espansione isotropica di ITV al fine di tenere conto delle estensioni patologie subcliniche microscopiche vicine al tumore. Tuttavia, i piani di trattamento progettati sono ottimizzati sui volumi target di pianificazione (PTV). Poiché gli approcci di espansione del margine isotropico nella generazione di PTV non sono in grado di spiegare adeguatamente i cambiamenti nelle densità dei tessuti lungo il percorso del fascio a causa delle incertezze di penetrazione nella terapia a protoni, viene generato un PTV specifico del fascio (bsPTV). Nella progettazione del piano di trattamento, il risparmio degli organi a rischio (OAR) attorno al volume target è assicurato dalla generazione di un anello di salvaguardia basato sull'espansione isotropica del margine bsPTV. Dopo i passaggi della disposizione dei fasci, del volume target e della definizione dell'anello di salvaguardia, vengono definiti il calcolo e l'ottimizzazione della dose. Il piano di trattamento simulato viene scelto se soddisfa i vincoli di dose nel volume target e negli OAR.

In questo studio è stato sviluppato un metodo per determinare e quantificare le incertezze dosimetriche derivanti dalle distorsioni geometriche nella terapia a protoni basate su MRI a prescindere dalla necessità di generazione di CT sintetiche. Al fine di simulare le distorsioni geometriche, un campo vettoriale di deformazione viene applicato sulle immagini CT creando delle immagini CT distorte. Una rappresentazione schematica della procedura utilizzata é mostrata in Figura 3.

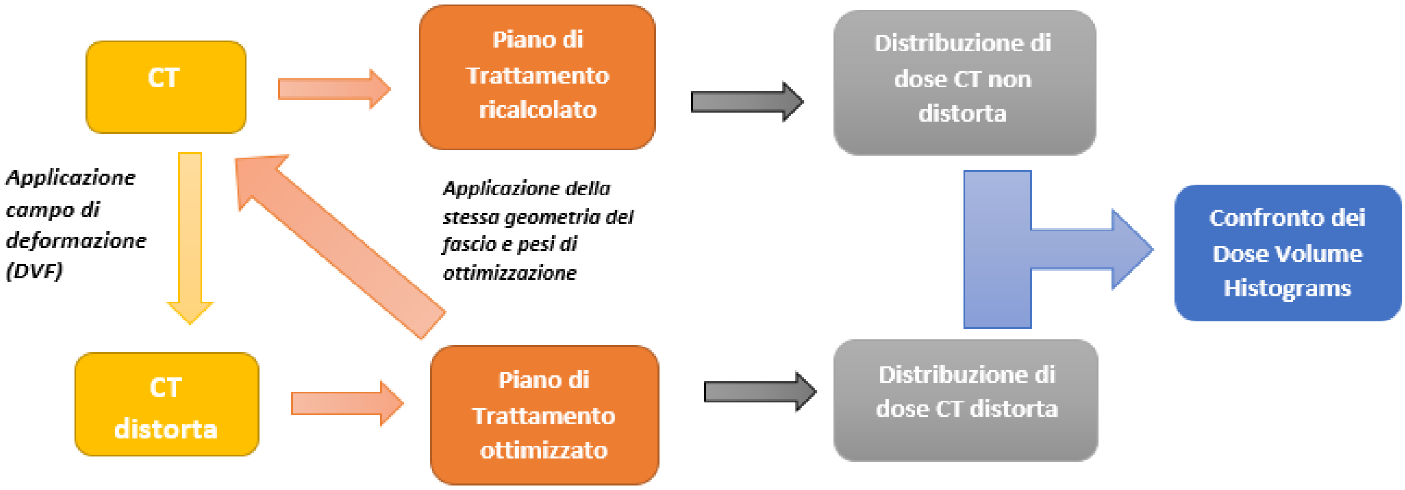

Figura 3 Schema a blocchi del metodo implementato per la quantificazione dell'impatto geometrico dells distorsioni spaziali indotte dallo scanner e dal paziente nella radioterapia MRI-only

Al fine di ottenere distribuzioni di dose comparabili per CT non distorte e distorte, che consente di determinare l'impatto dosimetrico delle distorsioni geometriche nel flusso di lavoro solo con MRI, il trattamento è progettato con gli stessi angoli di fascio, energie del fascio di protoni e prescrizioni di dose per entrambe le scansioni. I piani di trattamento sono progettati e ottimizzati in primo luogo sulle scansioni CT distorte, al fine di simulare un approccio basato esclusivamente sulla risonanza magnetica. I trattamenti sono ottimizzati separatamente per ciascun campo in base al PTV specifico del fascio come target, ottenendo così una singola dose uniforme (SFUD) per ciascun campo e l'isocentro del trattamento è definito come l'isocentro del bsPTV. La distribuzione della dose finale per la CT distorta, indicata come $D_{distorted}$, è ottenuta prendendo la media delle distribuzioni di dose generate da ogni singolo campo ottimizzato. Viene applicato il medesimo piano di trattamento creato e la dose viene ricalcolata sulla CT non distorta utilizzando la stessa geometria e gli stessi pesi del fascio calcolati nell'ottimizzazione sulla CT distorta. Come nel calcolo di $D_{distorted}$, la distribuzione della dose finale per CT non distorta, indicata come $D_{undistorted}$, è la media delle distribuzioni di dose generate da ogni singolo campo ottimizzato. Le distribuzioni della dose finale su CT non distorte e distorte vengono analizzate e confrontate in base al loro istogramma del volume della dose (DVH), che è un istogramma utilizzato come strumento di valutazione del piano nella pianificazione del trattamento di radioterapia che collega la dose di radiazione al volume del tessuto. L'analisi dosimetrica viene eseguita sul volume CTV e OAR nella distribuzione della dose finale. L'analisi sul volume CTV viene eseguita in termini di parametri DVH di dose quasi minima, indicata come D2%, dose quasi massima, indicata come $D_{98\%}$, dose media, D_{mean} e indice di omogeneità della dose (DHI). Nell'analisi di OAR, vengono valutati i parametri dose media, D_{mean} e dose massima, D_{max}. I risultati dosimetrici nel fantoccio e nei dati clinici si trovano in sostanziale accordo per ciascuna regione del corpo studiata nell'ambito di questo lavoro. Pertanto, le conclusioni sull'impatto dosimetrico raggiunto nel set di dati clinici sono confermate dai risultati su fantoccio, che possiamo considerare uno standard di riferimento.

A seguito dell'analisi effettuata sulle distribuzioni della dose finale del set di dati clinici, le differenze dosimetriche tra coppie di dosi deformate e non deformate sono risultate pari a 0,8%, 21,5% e 3,750% della dose prescritta in termini dei parametri dosimetrici $D_{2\%}$, $D_{98\%}$ e D_{mean}, rispettivamente. Per il parametro DHI, la differenza è risultata avere un valore massimo di 0,132. Al fine di determinare se le differenze riscontrate tra la dose non deformata e deformata sono statisticamente significative, è stato eseguito un test di Wilcoxon sui ranghi sul set di dati clinici comprendente tutte le regioni studiate. Secondo questo test, i risultati dosimetrici non deformati e deformati sono risultati statisticamente diversi nei parametri dosimetrici della struttura bersaglio al livello di significatività del 5% (ovvero confidenza al 95%), il che conferma che le distorsioni geometriche indotte dal sistema e dal paziente portino a cambiamenti dosimetrici statisticamente significativi nella struttura target. Al contrario, le differenze dosimetriche sono trascurabili negli organi a rischio e non sono risultate significative. Questo risultato conferma il vantaggio della terapia a protoni nell'erogazione della dose conforme al bersaglio e nel risparmio dei tessuti circostanti rispetto alla radioterapia convenzionale.

Per quanto riguarda i risultati su un determinato sito anatomico, si è riscontrato che l'impatto dosimetrico delle distorsioni geometriche nella struttura del CTV è più limitato piccolo nelle regioni dell'addome piuttosto che nel torace. Infatti, il test di Kruskal-Wallis eseguito sulla differenza tra la dose target non deformata e deformata (normalizzata rispetto alla dose prescritta nei parametri $D_{2\%}$, $D_{98\%}$ e D_{mean}) ha evidenziato come la differenza di dose nei polmoni ha una distribuzione statisticamente diversa rispetto a fegato e pancreas in termini di $D_{98\%}$ e parametro DHI. In particolare, abbiamo notato che le distorsioni geometriche causano minori cambiamenti dosimetrici nella struttura bersaglio per i tumori situati vicino o coperti dal tessuto molle. Questo non è il caso del sito polmonare, in cui il tumore può essere vicino ai tessuti molli o isolato all'interno del parenchima polmonare. In quest'ultimo caso, sono state riscontrate differenze di dose più elevate, dovute al fatto che il fascio viaggia su un percorso con variazioni di densità elevate nella regione polmonare e quindi potenzialmente non raggiunge il target. Pertanto, in questi casi, in cui il tumore è isolato dai tessuti molli, si suggerisce di evitare un approccio esclusivamente basato su MRI per la terapia a protoni. Escludendo questi casi, nello scenario clinico le differenze riscontrate tra la dose target non deformata e deformata sono piccole rispetto alla dose prescritta

Il lavoro descritto in questa tesi mira a quantificare l'impatto dosimetrico delle distorsioni geometriche nell'imaging MRI in un approccio per la terapia con protoni basato esclusivamente su risonanza magnetica nei siti extracranici. I risultati dello studio, pertanto, suggeriscono la potenziale applicabilità della terapia con protoni a sola risonanza magnetica, a condizione che le distorsioni non raggiungano variazioni dosimetriche clinicamente elevate quando il tumore è vicino o coperto dai tessuti molli. Poiché gli studi basati su un approccio MRI-only con protoni nelle regioni toraco-addominali sono limitati in letteratura, abbiamo presentato questo studio come punto di partenza per ulteriori ricerche per portare nella pratica clinica tale approccio per il trattamento di tumori extracranici. Un'analisi su un set di dati più ampio che includa diverse regioni corporee con più campioni contribuirebbe sicuramente a rafforzare i nostri risultati al fine di portare all'effettiva implementazione clinica. Infine, al fine di considerare tutti gli aspetti applicativi della vita reale della terapia a protoni basata sulla sola risonanza magnetica e testare l'applicabilità clinica, questo studio richiede di proseguire con un'ulteriore analisi che includa le incertezze introdotte dai metodi di generazione di CT sintetica nel flusso di lavoro.

1 INTRODUCTION TO PROTON THERAPY

1.1 Cancer

Cancer is a generic term referring to a collection of related diseases that can affect almost any part of the body. These diseases are characterized by the growth of abnormal cells beyond their usual boundaries without stopping and their invasion into adjoining parts of the body (World Health Organization, 2019a). Different from benign tumors, cancerous tumors are malignant and so they can spread into surrounding tissues (National Cancer Institute, n.d., a). Figure 4 visualizes the mentioned characteristics of the tumor cell.

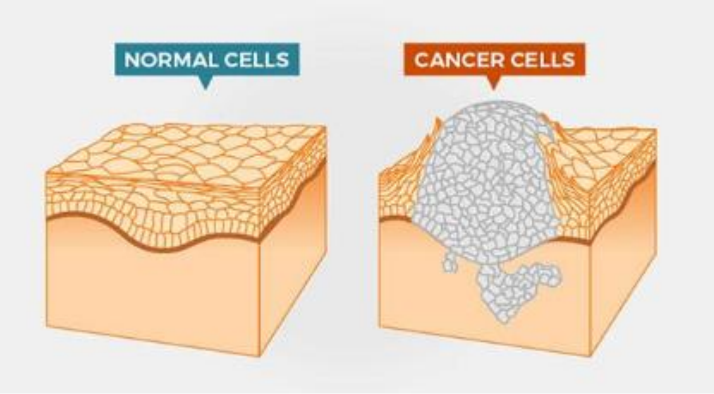

Figure 4 Normal vs. Cancer Cells. (World Health Organization, 2019a).

According to World Health Organization, cancer is the second leading cause of death around the world and accounted for around 9.6 million deaths in 2018 (World Health Organization, 2019a). Therefore, the treatment of cancer holds crucial importance. Each treatment strategy is unique to the patient and aims at local control of the primary tumor site by killing or neutralizing the tumor cell. The modality of the treatment for the patient depends on the type of cancer and its phase and depending on the case, a combination of different treatments can be required. Among different tumor sites, lung, liver, and pancreas will be considered in this work and the treatment modalities used for these body regions are discussed in detail below.

According to World Health Organization statistics for the year 2018, lung cancer is the most common cancer type affecting 2.6 million people and it has the highest record as a cause of cancer death with 1.76 million deaths (World Health Organization, 2019b). There are two main types of lung cancer, which are non-small cell lung cancer (NSCLC) and small cell lung cancer (SCLC). Most commonly, NSCLC is recognized in the lung as squamous cell carcinoma, large cell carcinoma, and adenocarcinoma. On the other hand, SCLC can be found in the hemithorax of origin, the mediastinum, or in the supraclavicular lymph nodes.

These patients have limited-stage disease whereas patients with tumors invading beyond supraclavicular areas are designated as an extensive-stage disease. In the treatment of lung cancer, compared to SCLC, NSCLC is relatively insensitive to radiotherapy and chemotherapy. In resectable cases, surgery is performed alone or together with chemotherapy which is carried out after surgery. In patients with unresectable disease, radiotherapy is a more effective modality for the local control. In patients with SCLC, radiation therapy and chemotherapy are shown to improve the survival of the patients (National Cancer Institute, n.d., b).

With reported 782.000 deaths in the year of 2018, liver cancer is the fourth leading cause of cancer-related deaths worldwide (World Health Organization, 2019b). Malignant tumors in the liver are divided into two major cell types, which are hepatocellular and cholangiocarcinoma. For primary hepatobiliary cancers, the use of conventional radiotherapy has been limited due to the toxicity to the normal surrounding tissues and the low dose tolerance of the liver to radiation. Advanced radiotherapy treatments such as particle beam therapy have been shown promising for the treatment of liver cancer in recent years. A superior dose distribution that spares the surrounding liver can be achieved with proton radiation therapy (Raldow, Lamb & Hong, 2019).

Pancreatic cancer develops from two different kinds of cells in the pancreas, which are neuroendocrine cells and exocrine cells. About 95% of pancreatic cancer develops from exocrine cells and it is usually diagnosed at an advanced stage whereas neuroendocrine tumors have a better prognosis. (National Cancer Institute, n.d., b). Diagnosis and detection of pancreatic cancer are difficult due to some reasons. Firstly, since some organs in the abdomen obscure the pancreas, clear visualization of the pancreas is challenging. Secondly, in the early stages, there is no noticeable symptom or sign for the diagnosis and pancreatic cancer shows many similar signs to some illnesses such as ulcer and pancreatitis, which creates the risk of dismissing the cancer diagnosis. For the treatment of pancreatic cancer, as long as it is feasible, surgical resection is the primarily preferred modality providing long-term survival. Moreover, chemotherapy together with surgery improves survival. Depending on the stage of the tumor, palliative and chemoradiation therapy is considered as a treatment modality as well. Recently, particle therapy has been used as a promising treatment for pancreas cancer. Proton radiotherapy is emerging as an efficacious and safe treatment modality for the treatment of pancreatic tumors (Raldow, Lamb & Hong, 2019).

1.2 Conventional and Particle Radiation Therapy

Radiation therapy uses high doses of radiation to shrink the tumors and kill cancer cells. By the destruction of the genetic material (DNA) of the tumor irreparably, the cancer cell stops dividing and growing or it is killed. It is achieved through consecutive radiation sessions. There are two types of radiation therapy, external beam and internal. The type of radiation therapy suitable for the patient is decided according to type and location of the cancer, size of the tumor, its distance to nearby healthy tissues, age and medical history of the patient and consideration of the other types of cancer treatment planned together with radiation therapy (National Cancer Institute, n.d., a).

Radiation is the energy that is radiated and propagated in the form of electromagnetic waves or particles and the radiation can be ionizing or non-ionizing. Ionizing radiation has enough energy to remove the bound electrons from the orbits of the atoms and radiotherapy uses ionizing radiation to induce damage to the tumor cells destroying their genetic material. Radiotherapy employs ionizing radiation with the energy expressed with the following formula:

$$E = h \times v$$

where $v = c/\lambda$: frequency λ: wavelength

$c = 3 \times 10^{8}$ m/s: speed of the light $h = 6{,}624 \times 10^{-34}$ J/sec: Planck's constant

In radiation therapy, the term ‘hitting the tumor’ physically refers to the energy that the radiation releases to the target. This energy is called absorbed dose and it has the unit of Gray (Gy) where 1Gy is 1J/kg. According to the International Commission on Radiation Units & Measurements (ICRU), it is expressed with the following formula (International Commission on Radiation Units & Measurements [ICRU], 1993):

$$D = \frac{d\mathcal{E}}{dm}$$

where absorbed dose, D, is the imparted energy, $d\mathcal{E}$, by ionizing radiation to the matter per unit of mass dm. While planning the treatment, the dose is planned in daily fractions with the aim of protection of critical healthy organs in the patient from high ionizing radiation. Ionizing radiation is found in the forms of electromagnetic waves and particle beams.

Electromagnetic waves carry energy through oscillating electrical and mechanical waves at the speed of light. The related part of the electromagnetic spectrum used in radiotherapy applications is the X-rays with energy ranging from 6 MV to 20 MV (Zaremba, Jakobsen, Thøgersen, Oddershede & Riahi, 2014). The electromagnetic waves interact with the matter with the following main interactions (Turner, 2007):

i. photoelectric effect: the incident photon is completely absorbed by the atom and one atomic electron from the inner shell is ejected.
ii. Compton scattering: the incident photon causes the ejection of an outer shell electron from the atom and a photon of lower energy is scattered from the atom.
iii. pair production: if the incident photon energy is greater than 1.022 MeV which corresponds to the twice the electron rest mass, an electron-positron pair is generated in the presence of an atom nucleus.
iv. coherent scattering: When the primary energy is lower than the electron binding energy, all photons energy is scattered in an elastic process, no energy conversion into electrons kinetic energy is required.

Particle beams carry energy in the form of kinetic energy with the atomic and subatomic particles in it. In the interaction of particle beams with the matter, electrons and heavy particles are considered. Electrons can refer to the secondary electrons like photo end Compton electrons and heavy particles can be either accelerated protons or ions. During its interaction with the matter, depending on the mass of each moving particle, charged particles deposit energy. The energy of charged particles degrades by the two main types of interactions, which are collisional and radiative.

The radiotherapy with protons or ions is termed as particle therapy or hadron therapy, which distinguishes it from conventional radiotherapy with photons. Hadrons are subatomic particles, typically protons and neutrons forming the atoms and the nuclei itself and they are connected together with strong nuclear force within the atomic nucleus. In the radiotherapy treatment, the hadrons used are protons and some atoms such as Carbon, Helium, and Oxygen, which have nuclei with low atomic number (Orecchia et al., 1998).

Conventional and particle beam therapy differ in geometrical selectivity and radiobiological effectiveness. Hadrons have different dosimetric characteristics than photons used in conventional radiotherapy. The depth dose profiles for different radiation types are shown in Figure 5.

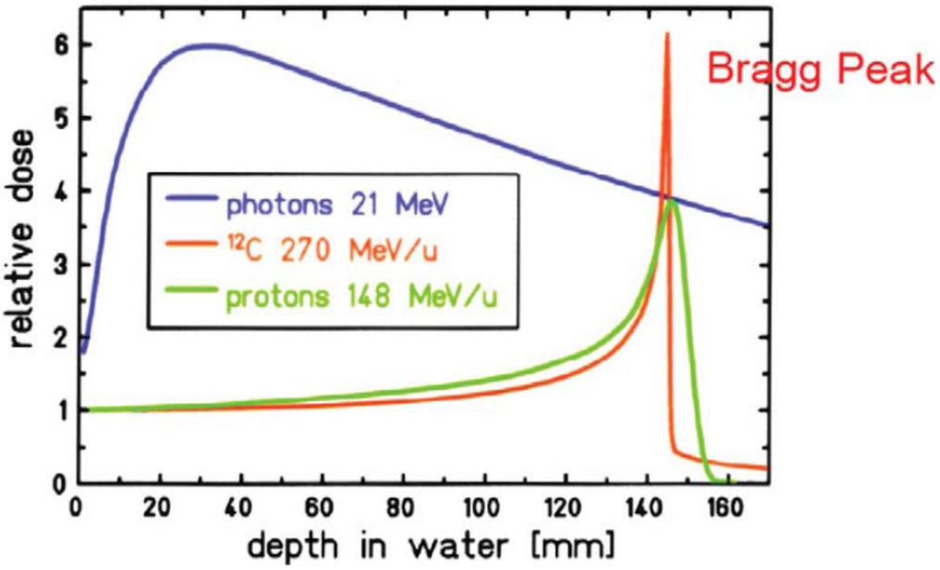

Figure 5 Depth Dose Profiles for Conventional and Particle Beam Radiation Therapy
Reprinted from "Ion beam radiobiology and cancer: Time to update ourselves" by Fokas, E., Kraft, G., An, H., Engenhart-Cabillic, R, 2009, *Biochim. Biophys. Acta, 1796*.

In conventional radiation, energy deposition with increasing depth in tissue takes place with an exponential decrease after a short build-up region. Differently from photons, protons and heavy ions penetrate tissues with a limited absorption and lateral scattering, and they are characterized by a narrow peak, which is called as 'Bragg peak', at the end of their path. Protons and heavy ions release most of their energy at the Bragg peak with a sharp fall-off at the distal edge. Protons present an increasing energy deposition with penetration distance, which leads to a maximum deposition near the end of the range of the beam (Paganetti, Bortfeld & Kooy, 2005). Heavy ions present a characteristic dose tail behind the Bragg peak, which is caused by a complex radiation field due to secondary fragments along the stopping path of ions produced in nuclear reactions (Schardt, Elsässer, & Schulz-Ertner, 2010).

In particle therapy, the position of the Bragg peak can be precisely adjusted to the depth of the targeted area by altering the initial kinetic energy of the ions. Therefore, it leads to a better conformation of the dose distribution on the target volume. Also, as the dose drops to zero sharply beyond the Bragg peak, compared to other radiation therapies, less energy is deposited into the healthy tissues surrounding the target. In the case of larger tumors, in order to cover the whole tumor, the Bragg peak can be shifted at different depths by varying the particle beam energy during irradiation and thus, the Bragg peak can be broadened by overlapping the beams with different energies. Therefore, while the monoenergetic particle beams feature a very narrow Bragg peak, beams with different energies produce an enlarged Spread-Out Bragg Peak (SOBP).

1.3 Proton Therapy

In proton therapy, as the protons moving through the tissue lose energy and slows down and deposit maximum energy at the end of their range, it allows the region of maximum deposition within the targeted area for each beam direction. In contrast to photons, protons energy ranges from 70 to 250 MeV (Mohan & Grosshans, 2017). Proton therapy has the following advantages over conventional radiotherapy (Paganetti et al., 2005):

i. Maximum energy release within the targeted volume
ii. Covering tumor volume with high accuracy
iii. Sparing of healthy tissues nearby by delivering lower doses to organs at risk
iv. Increased tumor control probability (TCP) with the feasibility of delivering higher doses to the tumor

Proton therapy is generally acknowledged to be effective, safe and recommended for many types of cancers and promising results have been and continue to be found (Mohan & Grosshans, 2017). Regarding also the regions under study in this study, lung, liver, and pancreas, proton therapy emerges as a promising modality. The use of radiotherapy for upper abdominal tumors is limited due to its toxicity to normal surrounding tissues, so proton therapy has clear dosimetric advantages over radiotherapy for upper abdominal regions by minimizing the radiation toxicity while maintaining high local tumor control rates (Raldow, Lamb & Hong, 2019). Moreover, the use of proton therapy for lung cancers is emerging in several centers due to its potential for improving the local control and overall disease-free survival (Kang et al., 2006). Therefore, due to its advantages, therapeutic potential and the clinical interest for the body regions of interest in this study, in the next sections, the discussion will be focused on proton therapy.

Today proton therapy is performed in several countries around the world. According to the latest statistics of Particle Therapy Co-operative Group (PTCOG), as of September 2019, there are over 80 proton therapy centers in operation worldwide with at least 39 centers under construction in records (Particle Therapy Co-operative Group [PTCOG], 2019).

1.4 Physical Characteristics of Proton Therapy

In this section, physical aspects of proton therapy are going to be mentioned including the concepts of stopping power ratio, linear energy transfer (LET), relative biological effectiveness (RBE).

1.4.1 Stopping Power and LET

In order to fully exploit the Bragg peak concept and greater biological effectiveness of particle therapy, Stopping Power and Linear energy transfer concepts should be addressed.

The energy of protons passing through the medium is lost with the successive collisions. Stopping power is the term defining the energy loss per unit path length ($-\frac{dE}{dx}$). Stopping power of protons depends on the electron density, velocity of the protons and mean excitation energy of the medium, and within the therapeutic range, the energy loss is mainly determined by the electronic collisions and inversely correlated to the particle energy. It is measured in units of [$\frac{MeV}{cm}$]. In order to be able to perform the dose calculation in proton therapy, Hounsfield Unit (HU) to stopping power ratio relative to water conversion is required. This conversion is based on calibration curves.

Linear energy transfer is the restricted form of stopping power and different from stopping power, it does not include the radiative losses of energy. According to ICRU, it is defined as:

$$L = \frac{dE_l}{dl}$$

where E_l is the local mean energy absorbed by the media by means of collisions resulting in energy transfer of charged particles of specified energy and dl is the traversed distance by the projectile (L'Annunziata, 2012). It has the unit of ${}^{keV}/_{\mu m}$. If the energy loss of a charged particle due to energy transfers is up to a specified energy cut-off value, energy-restricted LET (L_Δ) is defined for that specific part of energy loss and it is given with the following formula:

$$L_\Delta = (\frac{dE}{dl})_\Delta$$

where the cut-off energy (Δ) expressed in eV should be stated. If no cut-off energy is stated, it is shown with L_∞ and it includes all energy losses and equals to the total mass stopping power for the collision. The LET approximately describes the local energy transfer of charged particles and the shorter the range of radiation, the higher the LET value becomes since the energy dissipated per unit path length of travel increases (L'Annunziata, 2012).

1.4.2 Relative Biological Effectiveness

The relative biological effectiveness (RBE) is the term describing the radiobiological properties of the charged particles. It is defined as the ratio of the absorbed dose of the reference radiation (typically x-rays) to the dose of radiation under study to produce an identical biological effect and it is formulated as follows for the protons:

$$RBE = \frac{D_{reference}}{D_{protons}}$$

RBE is expressed by means of ionization of the DNA molecules of the irradiated cells. Protons have similar biological effectiveness as photons featuring an RBE value of 1.1 as a function of penetration depth.

In particle therapy, beams with different energies produce SOBP to cover large tumors. The broadened Bragg peak aims to deposit constant biologically effective dose, which is homogeneous to the target, and to cover the tumor with the maximal dosage (Wisenbaugh et al., 2014). The physical dose profile is corrected according to the RBE values of protons and carbon ions in order to feature a flat SOBP in the target region.

1.5 Beam Delivery in Proton Therapy

In order to meet the prescribed dose distribution, the beam has to be correctly arranged in both shape (linked to the dose-target volume) and amplitude (dose prescription). In order to make a treatment plan featuring conformal dose distribution and robustness to the range uncertainties, choice in how the protons are delivered holds crucial importance and it can have a large impact. There are two main treatment delivery techniques used in the clinic in order to conform the dose to the target (Bert & Durante, 2011):

i. passive beam shaping (passive scattering), and
ii. active beam scanning.

These techniques use different modelings of dose distribution. For the conformal dose distribution in large tumors, a mono-energetic beam of protons and ions is not suitable mainly due to the high dose gradient in the Bragg peak region. For the uniform dose coverage of the target at a different depth, SOBP, which features longitudinal beam spread, is needed. In passive scattering, the beam is spread orthogonal to its direction using scatterers and patient- and field-specific collimators and compensators are used for three-dimensional dose conformation. However, in active scanning, at each Bragg position, applied fluence dose can be varied which brings the advantage of conformal dose distribution to the target, sparing the organs at risk (McGowan, 2015). In the modern treatment facilities, active beam scanning is implemented.

Active Beam Scanning

In active beam scanning, the energy of particle beams is modulated during the irradiation using the accelerators and there is no need for passive attenuators. Therefore, it does not require any patient-specific hardware.

In active beam scanning, the target volume is divided into iso-energy slices where each slice is covered by a grid of voxels. The dose is delivered sequentially to each voxel. As the target volume is divided into layers, individual Bragg peaks within the target volume cumulatively form a SOBP. The trajectory of the charged particle is bent by the magnetic field generated with dedicated scanning magnets and the proton beam is deflected towards the planned position in the target. This results in improved target conformity. Moreover, the possibility of delivering the dose voxel by voxel helps to irradiate even the irregular shaped tumors effectively with optimal precision.

With the properties of providing greater flexibility for the target volume and reducing the dose in the nearby healthy tissues, active scanning allows the delivery of Intensity Modulated Proton Therapy (IMPT). Therefore, the radiation fields of active beamlines are intensity modulated fields (Schardt, Elsässer, & Ertner, 2010). IMPT is based on the principle that each beam delivers an optimized and inhomogeneous pattern in such a way that the combination of the individual fields produces final homogeneous dose distribution. Energy and intensity can be changed to control the dose at a point and adjust the depth of the dose (McGowan, 2015).

1.6 Treatment Planning

The radiation treatment includes two main steps, which are treatment planning and treatment delivery. Treatment planning is patient-specific and includes the steps of acquisition of patient imaging data, contouring of tumor and organs, selection of some parameters for the treatment, i.e. margins, radiation dose, and beam geometry, dose calculation, optimization and verification of the planned treatment. Treatment planning holds crucial importance for the resulting dose conformity in the target volume, sparing of the healthy tissue and robustness of the plan to the uncertainties. A tool called Treatment Planning System (TPS) is indispensable for the definition and simulation of different beamline settings and the analysis of 3D dose distribution.

1.6.1 Imaging and Planning

Medical imaging plays an important role in the state-of-the-art radiotherapy techniques in planning the desired treatment and verifying that it has been delivered as planned (Evans, 2008, Jaffray, 2012), thus guiding the radiotherapy workflow with the so-called Image-Guided Radiotherapy (IGRT). While planning the desired treatment, in order to have sufficient information for the tumor volume and the organs at risk, an imaging dataset is required.

The main imaging modalities used in the treatment planning include high-resolution anatomical imaging techniques, which are Computed Tomography (CT), and Magnetic Resonance Imaging (MRI), and functional imaging which is Positron Emission Tomography (PET). CT imaging provides information on the physical properties of the tissue with high spatial resolution and superior bone structure description. The gray level of CT image, which is represented in Hounsfield Units (HU), maps the radiation attenuation coefficients of the tissues. Conversion of HU values, obtained from CT images, to relative electron density (in the case of photon therapy) or to stopping power ratio relative to water (in the case of proton therapy) is used in the dose calculation. MRI provides images of tissue properties using static and gradient magnetic fields with radiofrequency excitation. Unlike CT, MRI uses low-amplitude non-ionizing radio waves and it provides superior soft tissue contrast with good temporal resolution. However, it has limitations as it causes increased image distortions (Schmidt & Payne, 2015). Lastly, PET as functional imaging provides information on different aspects of tumor biology.

Radiation therapy treatment planning is based on a hybrid workflow. Different imaging modalities play a complementary role, i.e. CT and MRI or CT and PET together, such that they are often combined to improve the interpretation of the clinical data and improve the tumor and organs delineation (Veninga, Huisman, Van Der Maazen, & Huizenga, 2004). The complementary use of CT and MRI plays an important role in treatment planning since MRI is better suited for contouring of the tumor volume and CT is required for the accurate radiation dose computation (Maintz & Viergever, 1998).

Image Registration

As the different imaging modalities used in the clinical workflow is of complementary nature, proper integration of the data is required. The integration of different imaging modalities includes registration and fusion steps. Registration is required to bring together different involved modalities into spatial alignment and fusion for the combined display of the data. Registration is defined as the optimization process aiming to provide maximum similarity between a reference and a target image by determining the spatial transformation that relates position in a reference image to corresponding positions in the target image.

Registration algorithms include mainly three components: similarity metric, transformation model and an optimization method as it is modeled in Figure 6.

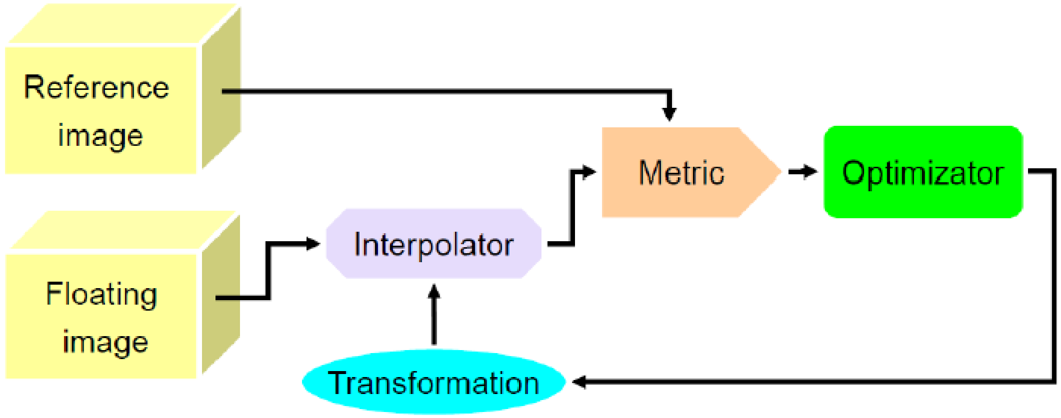

Figure 6 Image Registration Workflow representation with the components of the registration algorithm. Retrieved from 'Motion modelling techiques in radiotherapy: Deformable image registration', by C. Paganelli, 2018, Lecture Notes, Politecnico di Milano.

The similarity metric measures the similarities between images: it is a feature-based approach and aims to represent the cost function to be optimized. The registration can rely on anatomical landmarks, alignment of segmented binary structures or voxel-based measures computed from image gray values (Maintz & Viergever, 1998). Depending on the imaging modalities involved in the acquisition of images, the registration can be mono-modal or multi-modal. In mono-modal registration, images are acquired with the same imaging modality and thus the information from the images is of the same nature. This allows the gray levels to be comparable. For this registration, the most frequently used similarity metrics are mean squared error, and correlation coefficient, which are calculated with the assumption of equal and linear intensity relationships respectively. In multi-modal registration, since the information acquired from images are of different nature, gray levels are not comparable, thus the metric is not based on the absolute value of the voxel but on its information content. For this registration, normalized mutual information similarity metric is used which is based on the computation of the entropies of the intensity distributions (Maintz & Viergever, 1998).

The transformation model is based on the mapping of the coordinates of the target image to the coordinates of the reference image in order to increase the similarity between the images. Transformation can be either rigid or non-rigid. In rigid image registration (RIR), only translations and rotations are allowed and every pixel-to-pixel remains the same since the pixels move or rotate uniformly (Maintz & Viergever, 1998). RIR has been used commonly in radiation therapy, i.e. CT to MRI information fusion. It is effective in cases when anatomical changes are not expected (Oh & Kim, 2017). Non-rigid registration, also called as Deformable Image Registration (DIR), is able to effectively perform transformation when there is local distortion between the images. DIR has a significantly greater number of degrees of freedom (DOF) compared to RIR (Oh & Kim, 2017). Therefore, it can manage anatomical structure changes which can be due to several reasons such as weight loss, tumor reduction, and respiration. There are many different algorithms for DIR proposed in the literature. They are landmark-based, i.e. thin-plate spline or biophysical, intensity-based, i.e. demons and B-spline and finally finite element modeling-based registration algorithms. DIR plays an important role to analyze target motion and monitor tumor changes (Paganelli, Meschini, Molinelli, Riboldi, & Baroni, 2018).

Lastly, the optimization method aims to find the parameters of the transformation model, which gives the best similarity metric value. The objective function is either minimized or maximized and its shape can vary according to different models. Various optimization schemes exist with different performances in terms of speed and robustness.

1.6.2 Margins

Treatment plans are based on a static view of a patient. Therefore, there might be a variation between the planned and delivered dose, which is introduced with the term uncertainty. Despite the efforts on patient immobilization and usage of IGRT in order to deliver treatments with greater conformity, residual uncertainties are unavoidable. In order to manage these uncertainties, the treatment plans are based on the principle of irradiating a target larger than the tumor volume itself. According to International Commission on Radiation Units Reports 50 & 62, the following margins are defined (ICRU, 1993; ICRU, 1999):

i. GTV (Gross Tumor Volume): it includes gross touchable or visible extent and position of the malignant volume
ii. CTV (Clinical Target Volume): it is the tissue volume containing GTV and neighboring microscopic subclinical malignant pathologies. It is obtained by fixed or variable extension of the GTV.
iii. PTV (Planning Target Volume): it encompasses both GTV and CTV and accounts for all possible geometrical variations and uncertainties. It is defined for selecting the beam geometry and appropriate irradiation techniques to ensure that the prescribed dose is actually absorbed by the CTV.

Figure 7 demonstrates the target volumes with the discussed margins.

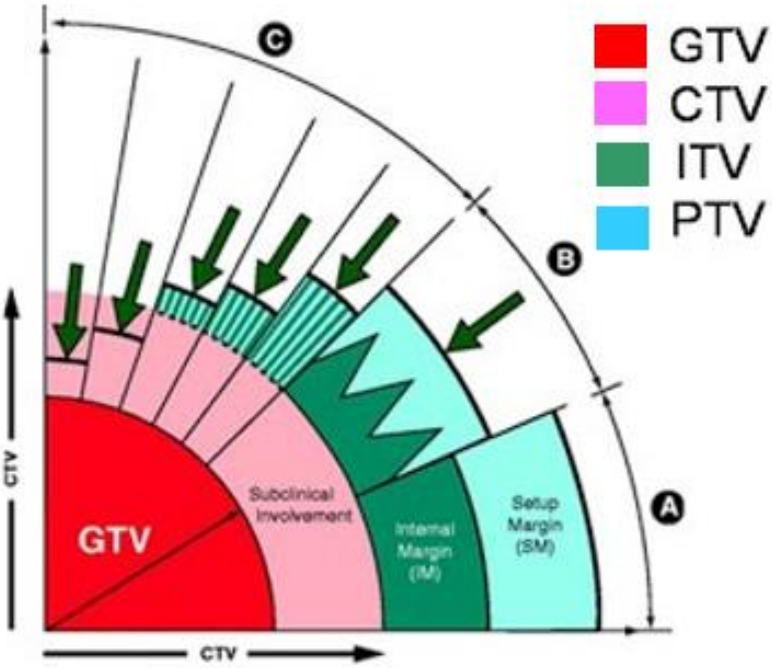

Figure 7 Demonstration of target volumes with their margins

Analogous to PTV, to ensure sparing of healthy tissues nearby the target, Planning Organ at Risk (PRV) is defined for the organs at risk in Report 83 by ICRU (ICRU, 2010). Moreover, in order to account for internal movement, internal target volume (ITV), which includes CTV plus an internal margin (IM), is defined. While the determination of GTV, CTV, and ITV are clinical, PTV creation is considered more with the physical process of beam delivery and its uncertainties. Therefore, the method of PTV creation differs depending on the choice of radiation therapy type and beam delivery.

The selection of the margins varies between the cases and the body districts. The optimal value decision for the margins holds crucial importance since reducing the margin would reduce the dose to the healthy tissue while it can also result in the geographical miss of the target.

1.6.3 Dose Calculation

In the clinics, mainly four different dose calculation techniques are used: Broad Beam Algorithms, Convolution Algorithms, Monte Carlo methods (MC) and Pencil Beam Algorithms (PBA). Currently, MC and PBA are the dose calculation algorithms available in commercial treatment planning systems in proton therapy (Saini et al., 2018).

Monte Carlo Simulations

The transport features of particles and their consequences in any type of medium (homogeneous or heterogeneous) is modeled with Monte Carlo methods. As Monte Carlo methods model with high accuracy the particle interaction properties with any medium they are going through, especially for heterogeneous tissues, it is considered as the gold standard for dose calculations, dosimetric validation, and dose distribution analysis (Agostinelli et al., 2003). After its generation, the interaction of the particle with the medium throughout its pathway happens at two different levels (Berger, 1963):

i. With the interactions with the medium or an external field, the intrinsic parameters, i.e. position, direction, and energy, are updated.
ii. The action of the primary particle and also the secondary particle, which is created during the interactions of the primary particle with the medium are monitored.

The interactions of particles are simulated randomly according to empirical look-up tables. The real randomness of interaction properties is represented with these lookup tables. As each particle is monitored along its pathway one by one, Monte Carlo simulations are time-consuming, taking some minutes to hours depending on the initial conditions and the required accuracy. The duration of the simulations is determined by several parameters, i.e. field size, particle energy, the grid resolution of the measurement matrix and the number of simulated particles.

Considering the accuracy and the speed, Monte Carlo algorithms can be discussed under three methods:

i. Detailed History Method: Particles are simulated and followed one by one according to their physical properties. Each secondary particle is followed one after each other. It provides high accuracy, but it is very slow.
ii. Condensed History Method: It is an algorithm implemented in MCNPx and GEANT4 (Fluka). The computational time is much lower compared to the Detailed History Method. In this method, the trajectory of the particles is segmented in a number determined by the atomic number of the media, and randomly oriented walk of particles, which is statistically very close to the real pathway, is created (Berger, 1963). The description of events occurring in each segment is approximated for each segment. Therefore, since each single event is considered by groups or clusters, it is much faster than the Detailed History Method.
iii. Track-repeating Methods: In this approach, pre-calculated particle pathways in water, which are modulated according to the stopping power ratio of the medium, are considered. Therefore, the computation and storage of the pathways save computation time compared to the previous methods. However, it also introduces inaccuracies due to approximations involved (Yepes, Mirkovic & Taddei, 2010).

Pencil Beam Algorithms (PBA)

In Pencil Beam Algorithms, the beam is decomposed into small beamlets. Each beamlet is associated with a 3D dose distribution and each has a contribution to the overall dose. The elementary dose contribution of each beamlet to reference medium, which is usually water, is called as a pencil beam dose kernel. The overall dose is calculated as the sum of the dose contributions coming from each active beamlet. The fact that the dose distribution from each beamlet is well defined mathematically in 3D space without any requirement of simulations makes Pencil Beam Algorithms different from Monte Carlo simulations.

The delivered dose, d, to an arbitrary point P(x,y,z) from each elementary beamlet directed towards z^* axis in Cartesian plane is expressed as follows (Hogstrom, Mills & Almond, 1981):

$$d(x,y,z) = C(z) \times O(x - x_0, y - y_0, z)$$

where C(z) is the central axis term in terms of depth, z, and O(x,y,z) is the off-axis term which depends on the depth in the medium as well as transverse distance from the beamlet axis, z^*. Accordingly, x_0 and y_0 represent the coordinates of the beamlet axis in regards to the central x-y beam frame. The relative geometric configuration is shown in Figure 8.

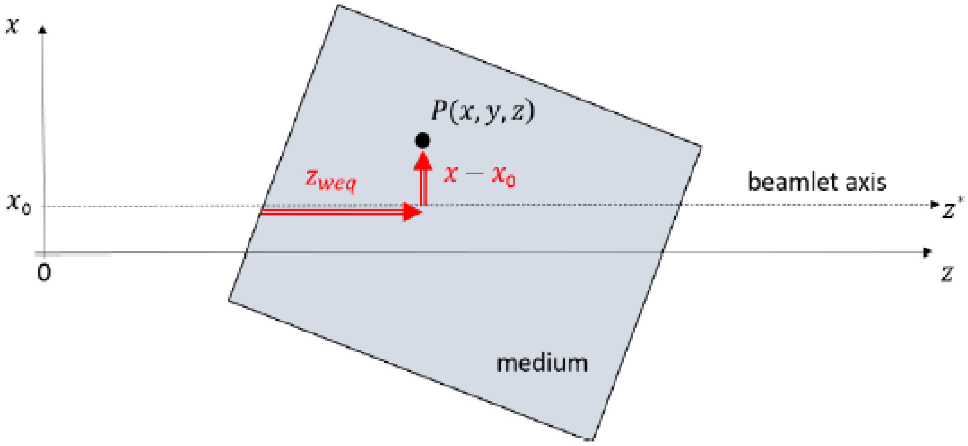

Figure 8 Description of the geometric configuration considered in the dose calculation of an elementary beamlet where beam axis is represented as a straight line and the ray axis z^* as a dotted line.(Deplanques, 2015)

Considering that the overall dose is the sum of the dose distributions from beamlets, the global dose to the point P(x,y,z) is expressed with the following formula:

$$D(x,y,z) = \iint_{beam\ aperture} d(x',y',z) \times dx' \times dy'$$

Therefore, taking into account the definition of dose from each beamlet, the global dose, D, can be finally written as:

$$D(x,y,z) = \iint_{beam\ aperture} C(z) \times O(x' - x_0, y' - y_0, z) \times dx' \times dy'$$

The central axis term, C(z), is constant for all beamlets at depth z and can be arbitrary chosen to correspond to the measured depth dose in the medium. Accordingly, in the infinite orthogonal plane at depth z, integration of off-axis term is normalized to 1 (Desplanques, 2015). Therefore, the expression of global dose in water equivalent medium at water equivalent depth of z_{weq} can be expressed as:

$$D(x,y,z) = C(z) \times \iint_{beam\ aperture} O(x' - x_0, y' - y_0, z) \times dx' \times dy'$$

which is then equal to:

$$D(x,y,z) = DD_{weq}(z_{weq}) \times \iint_{beam\ aperture} O(x' - x_0, y' - y_0, z) \times dx' \times dy'$$

where $\forall z, \int_{-\infty}^{\infty} \int_{-\infty}^{\infty} O(x' - x, y' - y, z) dx' dy' = 1$

The off-axis term distribution for the charged particles has a 2D single Gaussian shape (Eyges, 1948). Taking into account small angle approximation of Multiple Coulomb Scattering, off-axis term distribution would be expressed as follows:

$$O(x, y, z) = \frac{1}{2\pi\sigma^2(z)} e^{-\frac{x^2+y^2}{2\sigma^2(z)}}$$

where σ is called Standard Deviation of Pencil Beam Profile (SDPBP) and determines the beam spread due to particle interaction in the medium. This formula stands as an approximation to mainly account for Multiple Coulomb Scattering (MCS) and does not consider nuclear interactions.

Considering the definition of the dose distribution of a pencil beam and off-axis term distribution, the 3D dose distribution of a beamlet directed along z^* can be finalized as:

$$d(x, y, z) = DD_{weq}(z_{weq}) \times \frac{1}{2\pi\sigma^2(z)} e^{-\frac{(x-x_0)^2+(y-y_0)^2}{2\sigma^2(z)}}$$

1.7 Uncertainties in Proton Therapy

The sources of uncertainty in radiotherapy, i.e. inaccuracies in delineation, imaging, anatomical changes due to a change in tumor shape and weight loss and geometric miss of the target due to internal motion and patient set-up errors, are present also in proton therapy. However, the impact of these uncertainties on the delivered dose is greater in proton therapy than in conventional radiotherapy due to two main reasons. Firstly, protons have a finite range with a steep dose gradient at the distal edge of the Bragg peak. This brings the advantage of conformal treatment, but at the same time, if not properly predicted, even a small uncertainty can lead to under-dosage in the target volume or over-dosage in the nearby healthy tissues. Secondly, the range in proton therapy depends on the density of the medium that the beam travels through and it is a function of the stopping power ratio of the medium. Thus, any variation in the tissue density of the patient due to uncertainties would result in significant deterioration of the delivered dose (Engelsman & Kooy, 2005). Therefore, understanding and reducing these uncertainties holds crucial importance for an optimized treatment plan conformal to the target sparing the OAR.

The sources of uncertainties leading to uncertainties in the range can be discussed under two main groups: the variables causing uncertainties in range calculation in the treatment planning system (TPS) and those causing discrepancies between the planned and the delivered dose. The schematic of the sources of range uncertainties in proton therapy is shown in Figure 9.

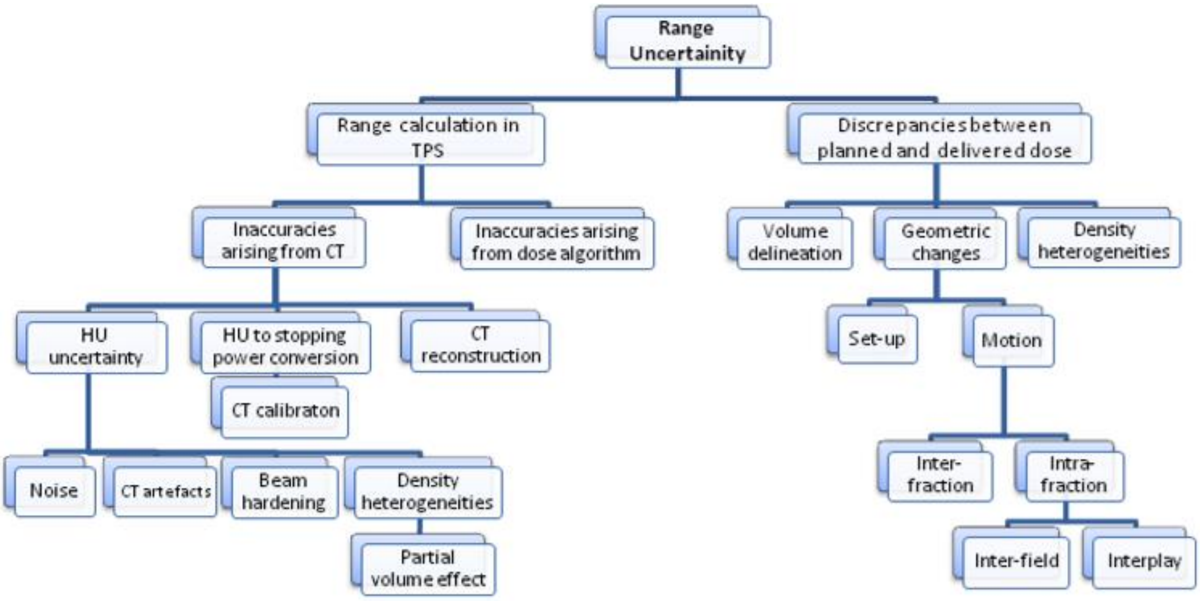

Figure 9 Sources of Range Uncertainties in Proton Therapy (McGowan, 2015)

In proton therapy, for a conformal and accurate treatment planning, range uncertainties should be properly accounted for. Different studies on the treatment margins in proton therapy have concluded that a PTV simply generated by the isotropic expansion of CTV is inadequate in proton therapy treatment planning (Moyers, Miller, Bush, & Slater, 2001, Engelsman & Kooy, 2005). Specific margins can be derived for proton therapies due to uncertainties that are covered in sections 1.8 and 1.9. Therefore, in proton therapy, unlike CTV, PTV should be beam delivery dependent which introduces the concept of 'beam specific PTV (bsPTV)'.

Proton beam on its beam path encounters tissues with different densities and chemical compositions. The variability and the uncertainty arising from the tissue heterogeneities along the proton beam path would lead to a target miss if not properly accounted for. Patient's anatomy change on the beam path would substantially vary proton dose distribution and in the presence of tissue heterogeneities, like air pockets, or dense bone, misalignment in proton beam would lead to significant hot spots or cold spots within the target volume (Park et al., 2012). Therefore, in order to account for the overall effect of these tissues on the beam range, a parameter named Water Equivalent Thickness (WET), which enables us to derive bsPTV volumes, is introduced. Beam specific PTV margins are calculated using the WET of the distal and proximal ends of the CTV volume with respect to the beam's eye view. WET implies to consider all the tissues on the beam path to have the same densities. Therefore, considering proton beams with the same initial energy, while they have different ranges in materials with different densities, their WET values is the same. Considering a single beam, WET corresponding to a line segment that extends from the source to a specific point in the target with depth, d, can be calculated using the relative stopping power ratio of proton (rsp) as follows:

$$WET\ (x,y) = \int_{source}^{d} rsp\ (x,y,z)dz$$

where relative stopping power at (x, y, z) is defined as:

$$rsp(x,y,z) = \frac{\rho_m \bar{S}_m}{\rho_w \bar{S}_w} \mathrm{I}_{x,y,z}$$

in which ρ_m and ρ_w are the mass density and $\bar{S}_m$ and $\bar{S}_w$ are the mean proton mass stopping power of medium and water respectively at (x, y, z).

1.8 Range Calculation Uncertainties in the Treatment Planning System

Inaccuracies in range calculation in the TPS can be caused by two main reasons, which are inaccuracies from CT and inaccuracies from the dose calculation algorithm.

1.8.1 Inaccuracies arising from CT

As previously mentioned in Section 1.6.1, Imaging and Planning, the gray-level of the acquired CT images is represented in Hounsfield Units (HU) and in order to be able to perform dose calculation, conversion from HU to proton-stopping power is required. At this point, inaccuracies in HU values and their conversion to proton-stopping power result in inaccuracies in range calculation (Chetsov & Paige, 2010).

Inaccuracies in HU values arise from noise, CT artifacts, beam hardening, and density heterogeneities. Noise is a stochastic uncertainty and it adds uncertainty in the order of ±1% (Schaffner & Pedroni, 1998). Beam hardening depends on the tissue density and the position of the tissue and it has a contribution to the range calculation uncertainties by ±1.1% and ±1.8% for soft tissue and, bone respectively (Schaffner & Pedroni, 1998). Treatment plans are sensitive to the tissue heterogeneities and its sensitivity is affected by the proton final range, sharp fall-off at the distal edge of the Bragg peak and multiple Coulomb scattering. In order to determine the effect of inaccuracies in HU values on the delivered dose onto the target volume, a test study has been carried out in which ±3% HU uncertainty is introduced in the prostate case and skull base case. As a result of the study, systematic over- and under-dosage of the CTV of 5% has been determined with the distal edge tracking (DET) approach and even less difference is determined with 3D IMPT (Lomax, 2008a).

In order to determine the effect of HU to conversion in range calculation uncertainty, a test study has been carried out in which the calculated proton range is compared with the proton range determined from PET imaging in a phantom. As a result, it has been concluded that the uncertainty caused by the conversion from HU to proton-stopping power is ±1% (España & Paganetti, 2010). In the conversion from HU to proton-stopping power, CT-scanner specific calibration is essential due to the fact that HU values depend on X-ray spectrum and target position and thus, different X-ray spectrums are generated from each scanner requiring individual calibration. Considering all these facts, usage of proton CT would eliminate the uncertainties due to the conversion of HU to proton-stopping powers (Schulte et al., 2004).

1.8.2 Inaccuracies arising from Dose Calculation Algorithm

The uncertainties in density calculation from CT data causes deterioration in the dose. Analytical dose calculation algorithm projects the proton beam range according to the water-equivalent depth in the patient, which neglects the heterogeneities relative to Bragg peak depth and thus this method has limitations in the prediction of the precise proton beam range (Paganetti, 2012). In contrast to analytical dose calculation algorithms, Monte Carlo model uses probability distribution in order to simulate interactions and secondary particle productions in the medium in which the beam travels through, but still, there are uncertainties when using the Monte Carlo algorithms as well. In order to evaluate the uncertainties coming from analytical dose calculation algorithms, a comparison is made with the same plans calculated using Monte Carlo algorithms in the skull base case. It has been concluded that, for an acceptance level of ±10%, the two calculation methods were in close agreement, but the agreement decreases for lower acceptance levels (Lomax, 2008b). Moreover, it has been concluded by Paganetti that the two dose calculation techniques show clinically insignificant differences due to the fact that the effect of dose calculation uncertainties is minimized thanks to the conservative treatment margins (Paganetti, 2012).

1.9 Discrepancies between Planned and Delivered Dose

Another cause of range uncertainty is the set-up uncertainties and organ motion which result in the geometric change of the position of tissue heterogeneities with respect to the proton beam path.

1.9.1 Set-up Uncertainties

Set-up errors can take place in the registration of external surface markers on the patient or in the registration of soft-tissue or bone landmarks during image-guidance and they would cause a geometric miss of the target. It is essential to be able to successfully handle the set-up errors since in the treatment plan the iso-center of the beam is defined relative to the position of the target volume. Set-up uncertainties can be discussed under two main groups: systematic and random set-up errors. The systematic set-up error is caused by several changes, i.e. change in the treatment room, or landmark position. It is committed during the entire treatment simulation. Unlike systematic set-up errors, random set-up errors occur occasionally in the treatment simulation with a varying value from fraction to fraction. Therefore, with a set-up consistent between the fractions, random set-up errors can be minimized.

1.9.2 Organ Motion

Organ motion is an important issue needed to be successfully accounted for in radiation therapy since the accuracy of imaging, treatment planning, and delivery is highly affected by the geometric uncertainties introduced by organ motion (Keall et al., 2006). Organ motion can be categorized and discussed in three categories:

i. Inter-fractional organ motion: inter-fractional motion is a slowly happening change indicating the motion between each fraction. It can be due to tumor shrinkage due to weight loss or response to the treatment.
ii. Intra-fractional organ motion: it indicates the motion during the treatment delivery which can be caused by respiration, cardiac, gastrointestinal and skeletal muscular systems. The most relevant source of intra-fractional organ motion is the respiration and the lungs, esophagus, liver, pancreas, breast, prostate and kidneys move with breathing (Keall et al., 2006). Therefore, respiration affects the tumors in the thorax and abdominal regions. These motions are fast and periodic with relatively high frequency. Intra-fractional organ motion is either inter-field (between each field) or intra-field (during the field). For active scanning, the major effect of intra-field

> motion is interplay indicating the interference between tumor motion and scanned beam due to similar frequency between the respiratory motion and the scanned beam. The interplay effect causes deteriorated and non-homogeneous dose distribution in the irradiated volume.

Inter-fractional motions occur in a time scale of minutes to hours whereas intra-fractional motion takes place in a shorter time frame, which is in a scale of seconds to minutes. Therefore, for inter-fractional motions, action is required only before the treatment delivery and they can be handled by the adjustment of the geometric set-up before the treatment delivery by positioning the patient relative to the beam as planned in the treatment plan. However, for taking into account intra-fractional motion successfully, treatment should be adapted in the planning phase accordingly (Meschini, 2015, Keall et al., 2006). Considering all of these facts, special attention should be paid to the patient positioning before the treatment delivery and the continuous real-time monitoring of organ motion during the treatment delivery for the conservation of the beam-target relative geometry at each fraction.

Geometric changes cause density variations leading to a change in the radiological path length along the beam path. In X-ray therapy, the effect of density changes on the dose distribution is only a few percent. However, in proton therapy, it is more severe blurring the dose gradients from target volume and changing the distribution of resulting dose with the under-dosage of the CTV and over-dosage of the distal healthy tissues and OAR. In IMPT, PTV is the only method to record the dose to the moving CTV and to ensure that moving CTV is covered (McGowan, 2015).

Intra-fraction motion can be classified as inter-field, which takes place between each field, and intra-field motion, which happens during the field. According to a study by Lomax carried out in the prostate region in order to investigate the effects of inter-fraction, intra-fraction and inter-field motion, a 5mm shift in the dose distribution would cause under-dosage of the CTV by up to 20% when the plan is optimized for maximum OAR sparing. Therefore, it has been concluded that a simple PTV margin would not be sufficient to apply in certain IMPT plans in order to compensate for inter-fraction motion (Lomax, 2008b). Therefore, it necessitates the design of a treatment plan with a beam specific planning target volume in proton therapy.

In many body districts, organ motion has to be taken into account and incorporated into treatment planning and delivery workflow.

Treatment Planning in Moving Districts

In order to take into account, the organ motion in treatment planning, the CT image should be able to visualize the full extent of the tumor motion. This is possible thanks to slow CT, inhalation and exhalation breath-hold CT, respiratory gating and four-dimensional CT (4D CT) (Keall et al., 2006). In slow CT acquisition, the scanner operates very slowly and it is based on the principle of image reconstruction with the average of the multiple CT scans. In this approach, the reconstructed image is able to describe the entire tumor motion. Since the tumor in the lung has high contrast against its medium, this method is successful for lung tumors and not recommended for the other sites. In inhalation and exhalation breath-hold CT, two 3D CT images are acquired at the extreme lung volume moments, one at the end of the inhalation when the lung volume is maximum and one at the end of the exhalation when the lung volume is minimum. This approach is effective in determining the range of the tumor motion, but does not contain the full extent of the motion and requires the patient to be able to keep his/her breath hold, not an easy task especially for lung cancer patients. In the respiratory gating method, snapshot CT acquisition takes place while the patient is holding the breath at a specific phase of the respiratory cycle, which is referred as the gate. The variables characterizing the respiration are amplitude and phase and they are determined with the help of the external surrogates' signal or internal fiducial markers, which are synchronized with the breathing cycle. The specific phase of the respiratory cycle is determined in terms of its position and length using amplitude and phase variables. The gating window is defined in terms of the amplitude such that the part of the respiration in which its amplitude is within a pre-determined range is chosen, or in terms of the phase such that the time interval in which the respiration signal is within a pre-set phase window is chosen (Keall et al., 2006). Lastly, the 4D CT approach is based on the time-resolved retrospective sorting of the breathing phases (Vedam et al.,2003) and represents the current clinical standard. The respiratory cycle is recorded with several 2D slices synchronized with an external surrogate signal, and accordingly, volumes representing different respiratory phases are reconstructed and retro respective sorting is performed based on the respiratory amplitude/phase. The treatment plans in the thorax and abdomen regions, which are highly affected by the respiratory motion, are usually based on 4D CT. Figure 10 shows the workflow of 4D CT generation.

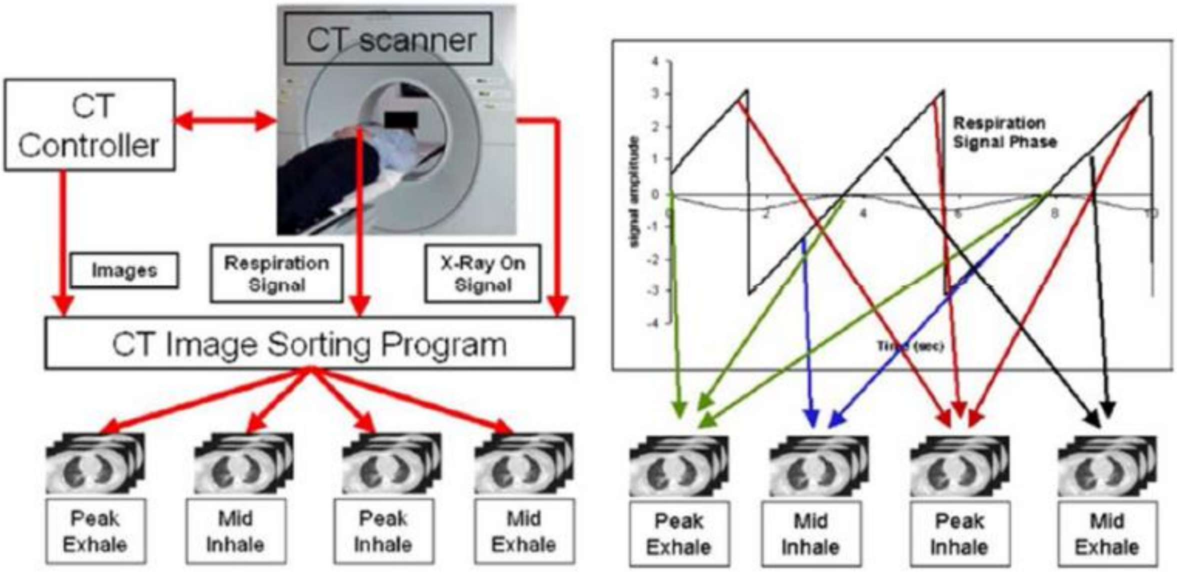

Figure 10 Schematic representing the 4D CT Retro respective phase sorting workflow with the inputs of images from CT scan, respiration signal when the X-ray imaging signal is on (Vedam et al., 2003)

The motion should be an essential concern not just in the treatment planning, but also in the treatment delivery in order to successfully compensate its effect on the treatment effectiveness. In the treatment delivery, there are different approaches taking into account the motion compensation and treatment delivery should replicate the motion management strategy, which is adopted during planning.

2 INTRODUCTION TO MRI IN RADIATION THERAPY

2.1 MRI in Radiation Therapy

Computed tomography is the primary imaging modality used to ensure accurate treatment planning in radiation therapy (Pereira, Traughber & Muzic, 2014). It has high geometric accuracy and is able to provide good visualization of the high-density tissues such as bone. Most importantly, for the dose calculations in the treatment planning, CT images provide information on the relative electron density (in the case of photon therapy) and stopping power ratio relative to water (in the case of proton therapy) from the Hounsfield Units. However, CT imaging has a primary disadvantage of low tissue contrast and this problem leads to significant differences in tumor definition varying from physician to physician (Pereira et al., 2014). At this point, MRI contributes significantly to the tumor and OAR delineation in the treatment planning with its superior soft tissue contrast with respect to CT (Chandarana, Wang, Tijssen, & Das, 2018). MRI provides multiple contrast information and its contrast from different weighted imaging renders possible highlighting a specific organ or tumor (Chandarana et al., 2018). Figure 11 helps to visualize the soft tissue contrast in MRI and CT images and provides the superiority of MRI in discriminating the regions which should be irradiated and which should be not.

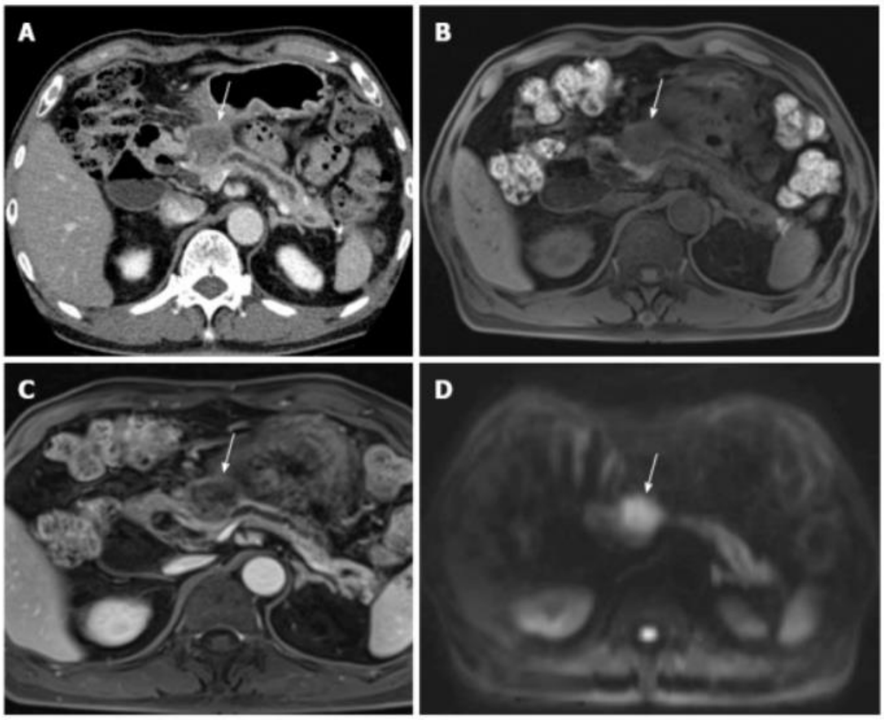

Figure 11 Differences in the soft-tissue contrast from MRI and CT scans in pancreas region in which arrow points the pancreatic head (A) CT scan, (B) T1-weighted gradient echo sequence of MR, (C) contrast administered MRI, (D) Diffusion-weighted MRI (Lee, E. S. & Lee, J. M., 2014)

Due to the superiority of MRI in soft tissue contrast visualization, MRI has been the complementary imaging modality in treatment planning for target and OAR delineation since the beginning of the 1990s (Dirix, Haustermans & Vandecaveye, 2014). The combination of CT and MRI images would allow having both a good soft tissue contrast for accurate contouring and electron density or proton stopping power ratio relative to water, which enables the dose calculation for treatment planning. Therefore, in current clinical practice, treatment planning is based on a hybrid workflow in which the patient undergoes CT and MRI imaging before the treatment (Chandarana et al., 2018). This workflow is possible by the image registration of these two modalities into a common geometric reference frame which is explained in detail with its theoretical aspects in the previous subsection, Image Registration.

When image registration of two modalities is involved in radiation therapy, the workflow of treatment planning and delivery is as follows as shown in Figure 12:

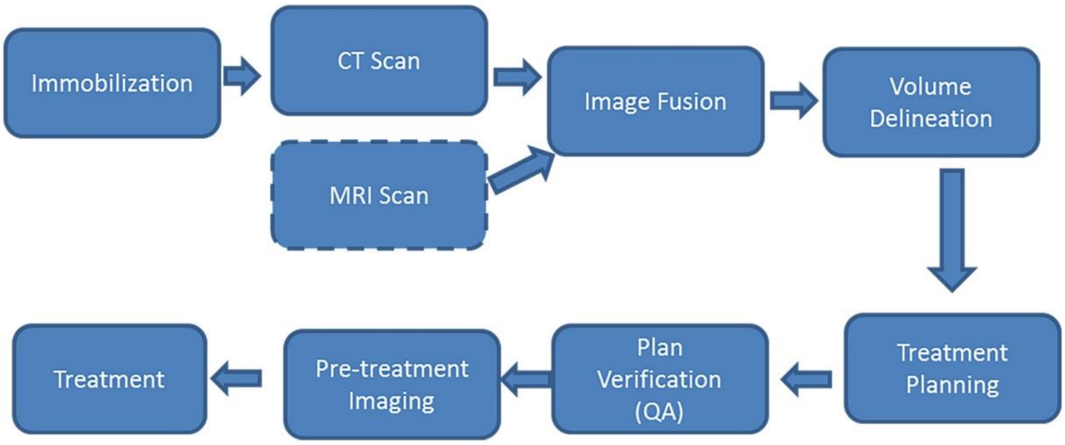

Figure 12 Workflow of radiation therapy treatment planning and delivery when image registration of CT and MRI is involved (Chandarana, 2018)

As it is represented in Figure 12 above, after the immobilization of the patient with the immobilization devices, which have low electron density to avoid the attenuation of the beam, the patient undergoes MRI and CT imaging subsequently. Fusion is the step for displaying the registered images coming from different modalities in a composite image (Pereira et al.,2014). The fusion of images from MRI and CT enables accurate volume delineation by high soft-tissue contrast, and dose calculation.

While CT imaging exposes the patient to high ionizing radiation, MRI provides a multitude of different image contrasts by the usage of different MR sequences without patient radiation burden (Guerreiro et al., 2019). However, in terms of the geometric accuracy of the images used in treatment planning, CT is considered as the gold standard and MRI images can bring geometric distortions, which would result in systematic errors in radiation therapy treatment planning and delivery (Weygand et al., 2016). In this section, the usage of MRI in radiation therapy is going to be discussed in more detail in the contexts of MRI-only radiation therapy with its application methods, advantages and challenges due to image distortions raised by MRI.

2.2 MRI-Only Radiation Therapy

In the clinically used current practice, CT/MRI image registration for treatment planning would introduce systematic spatial uncertainties and would be time-consuming and pricy for the patient requiring several imaging sessions. In order to avoid the spatial uncertainty and patient exposure to ionizing radiation arising from the CT/MRI hybrid workflow, and provide a workflow reducing the time, effort and resources spent by the patient and hospital, techniques excluding the CT from the workflow has been introduced which are referred to as ‘MRI-only’ or ‘MRI-based’ or ‘MRI-alone’ radiation therapy (Maspero et al., 2017, Edmund & Nyholm, 2017, Johnstone et al., 2018). In this thesis, the term MRI-only is going to be used to refer to these workflows. MRI-only radiotherapy has been first studied in conventional radiotherapy with a focus on brain and prostate tumors (Ramsey & Oliver, 1998, Beavis et al., 1998, Khoo et al., 1997, Lee et al., 2003) and the research on MRI-only treatment planning has increased with the strong interest of many groups to move toward MRI-only workflows (Owrang, Greer & Glide-Hurst, 2018). The studies on MRI-only workflow is recently extending to particle beam therapy as well. In the recent few years, MRI-only workflow has been introduced into the clinic. In 2014, MRI-only radiotherapy workflow has been clinically used for the first time in treating the prostate patients in Helsinki University Hospital (Tenhunen et al., 2018).

MRI-only treatment planning would bring several advantages. The main advantages put forward in the literature in favor of MRI-only radiation therapy compared to conventional hybrid workflow can be highlighted as follows:

i. Eliminating CT from the treatment workflow would eliminate the spatial uncertainties arising from the CT/MRI image registration, which affect each fraction and are systematic (Guerreiro et al., 2019). According to different studies conducted in order to investigate the magnitude of the registration errors, it has been reported that the CT/MRI registration would cause a spatial uncertainty of 1.7-2 mm

(Roberson et al., 2005, Nyholm, Nyberg, Karlsson M. G., & Karlsson M., 2009, Korsager, Carl, & Riis, 2016, Wegener et al., 2019). A systematic registration error would lead to a persistent systematic treatment error that would present in all of the treatment fractions. This would create a dose distribution, which is far away from the target due to displacement and would significantly decrease the effectiveness of the treatment regarding tumor control (van Herk, 2004).

ii. CT causes ionizing radiation exposure to the patient. Therefore, MRI-only based workflows would decrease patient exposure to ionizing radiation (Guerreiro et al., 2019). However, compared to the dose administered during radiation therapy, the contribution of ionizing radiation from CT imaging is significantly low which would be probably negligible (Tenhunen et al., 2018). The radiation exposure reduction by using MRI-only therapy would be considered of interest when repeated imaging is necessary for example in the scenario of adaptive radiotherapy involving weekly scans based on MRI data (Jamtheim Gustafsson, 2019). Moreover, bringing together the advantages of reduction of spatial uncertainty due to image registration and reduction of ionizing radiation is particularly important for pediatric patients for whom a lot of effort is put to reduce radiation-induced complications (Guerreiro et al., 2019).

iii. In the hybrid workflow of CT and MRI, inter-scanner differences can appear between the two imaging sessions. Therefore, MRI-only treatment is proposed to remove any potential inter-scan differences (Maspero, 2018).

iv. Considering that no CT is required, MRI-only workflow is cost-effective as it requires fewer imaging sessions and it is more efficient (Chandarana et al., 2018).

v. Avoiding a hybrid CT/MRI workflow would help to save time. According to a study comparing clinical MRI-only treatment with CT/MRI workflow, time-saving of approximately 15 minutes is reported (Tyagi et al., 2017).

vi. MRI-only treatment workflow is being a promising advance for the MRI guided photon and proton radiotherapy (Maspero et al., 2017).

While MRI-only workflow brings several advantages to the current clinical practice of treatment plan, it requires to generate suitable images enabling treatment planning, defined as synthetic CT images.

Synthetic CT Generation

In a conventional workflow, CT image provides electron density and relative stopping power ratio information from the HU in order to calculate the absorbed dose in radiotherapy treatment planning.

However, in MRI, magnetic relaxation times and proton density of the tissue determines the signal. Therefore, image intensity and contrast in MRI is not directly related to HU or electron density and relative stopping power ratio required for treatment planning. Obtaining the HU information from the MRI images requires the conversion process and the new images providing this information are referred as ‘synthetic CT’, ‘pseudo-CT’ or ‘substitute CT’ (Gustafsson, 2019). In this thesis, the term synthetic CT, also donated as sCT, is going to be used. Figure 13 is presented to visualize the difference between a conventional CT and sCT. It shows a conventional CT image on the left and an sCT image generated from a T2 weighted image on the right.

Figure 13 Conventional CT image on the left and sCT image generated from T2 weighted MRI on the right (Gustafsson, 2019)

Synthetic CT images provide maps with HU tissue information like CT and they are generated from the MRI images in order to serve as a surrogate for dose calculations. Different techniques for sCT generation have been introduced with different categorizations. According to the categorization used by Guerreiro et al. (2019), there are mainly four different approaches:

i. Bulk-density override: Bulk-density override is based on assigning specific densities to segments of the patient volume which are determined according to manual or automatic intensity-based contour segmentation (Guerreiro et al.,2019). It can be either by assigning a homogeneous density to the whole body which is the simplest approach or by assigning heterogeneous density distribution in which soft tissue, bone, and air are assigned different densities.

ii. Atlas-based methods: This approach consists of a reference material with CT and MR images. In this method, MR to CT image atlas is created such that CT representation of the MR image is created (Jamtheim Gustafsson, 2019). It enables the conversion of MRI intensity to HU units. Non-linear image registration is involved between the MR scan from the reference material, one or more atlases of MR scan representing the correspondences with the CT scan and an organ label map.
iii. Voxel-based methods: Voxel-based methods rely on MRI contrast, which is considered independent of the voxel locations. It involves the conversion of individual MR voxels to their corresponding CT HU units. This conversion is based on a combination of classification and bulk density assignment or a regression model that share the common feature of being a learned criterion. In the learning-based approaches, using supervised training a map function is generated in order to associate MR voxel intensities or image patches with HU numbers.
iv. Deep learning methods: The introduction of deep learning algorithms for sCT generation is a recent approach being explored (Guerreiro et al., 2019). Convolutional Neural Networks (CNN) learn multiple levels of information from MR-CT image datasets and by training, they are able to learn the mapping from 3D multi-parametric MR patches to the same size 3D sCT (Chandarana et al., 2018).

Bulk assigned is a user friendly sCT generation method (Guerreiro et al., 2019) and as a result of several studies, comparing dose distribution from sCT and conventional CT-based calculations, it has been reported to result in equivalent dose for brain tumors (Prabhakar et al., 2007) and dose deviation within 2% for the prostate case when heterogeneous density is assigned (Lambert et al, 2011). However, it does not offer high accuracy results for more challenging regions such as head and neck and lung tumors and thus needs improvement (Jonsson, Johansson, Söderström, Asklund & Nyholm, 2013). Moreover, the need for manual bone segmentation limits its clinical usage (Lambert et al.,2011). Atlas-based methods present limitations due to its lack of adaptation to atypical patients. It would result in poor accuracy in this group of patients since deformable image registrations can be used when matching CT and MRI images (Guerreiro et al., 2019). Compared to atlas-based methods, voxel-based methods are more suitable to be used in patients with atypical anatomy. Lastly, deep learning methods would require a long time and a large dataset for training, but after the training is completed, this approach would offer faster sCT generation compared to the previous methods (Chandarana et al., 2018). Considering all the approaches for the generation of sCT to eliminate CT in the treatment workflow, it should be highlighted that several studies have concluded that atlas-based and voxel-based methods are the most clinically useful approaches with a report of dose discrepancies of less than 1% in the prostate target (Jamtheim Gustaffson, 2019).

2.3 Challenges in MRI-Only Radiation Therapy

In MR imaging, a magnetic field radio-frequency pulse is applied in order to measure the temporal evaluation of the magnetic dipole moments of nuclear spins within the magnetic field. MR images are formed from tiny signals, which are induced by the precessing of these atomic dipoles in a strong magnetic field (Schmidt & Payne, 2015). Therefore, spatial encodings in MRI relies on the well-defined magnetic field. Alterations in the magnetic field can occur due to system-dependent and patient-dependent uncertainty sources (Weygand et al., 2016) and these alterations would lead to geometric distortions in MR imaging. Geometric distortions introduce systematic errors in radiotherapy planning and treatment (Jamtheim Gustafsson, 2019). In the image field of view (FOV), image distortions exceeding 2 mm has been suggested as the level requiring consideration (Weygand et al., 2016). Therefore, it is important to understand the sources of these distortions in order to be able to reduce them and therefore their effect on the treatment successfully. In this section, the main causes of geometric distortions, which are categorized under the system- or patient-dependent distortions are going to be discussed in detail.

There is no standard procedure developed for the characterization of the geometric distortions in MRI. Several methods have been presented in the literature for the measurement and mapping of the MRI system-dependent distortions. 2D and 3D geometric phantoms play an essential role for this purpose and the phantom based techniques are the commonly used approaches for the characterization of MRI distortions (Huang, Cao, Baharom & Balter, 2016, Kroll et al., 2018). Signal markers located at known positions in these phantoms are used to calculate the displacement map. Basically, the discrepancies between the physical locations of the markers and their positions measured in MRI images are used to assess the geometric distortion.

For the reduction of the system-induced distortions, different strategies are used depending on the origin of the distortion. Geometric distortions stemming from gradient nonlinearities are not limited to any spatial direction and not constant between the scans. Therefore, for their correction, in-plane (2D) or in-plane and through-plane (3D) vendor-specific correction software are used. For the correction of the geometric distortions arising from the static magnetic field inhomogeneities, magnetic field shimming can be used. If the residual B_0 inhomogeneities persist after shimming, higher acquisition bandwidth can be enabled for reducing the effect of B_0 inhomogeneities. The reduction of the patient-dependent distortions is similar to those strategies used for the reduction of magnetic field inhomogeneities. These approaches include magnetic field shimming, decreasing echo time and using higher acquisition bandwidth.

2.3.1 System-Dependent Distortions

System-dependent distortions arise from the imperfections in MRI hardware. In ideal conditions, MR images are generated from the superimposition of a constant magnetic field gradient to a uniform static magnetic field. If these magnetic fields are not accurately tuned, spatial signal encoding loses its accuracy leading to image distortions. MRI system-induced geometric distortions can mainly stem from nonlinearities in spatial encoding gradients and inhomogeneities in the main static magnetic field (B_0) (Schmidt & Payne, 2015). These distortions vary linearly with the increasing distance from the MRI system isocenter (Walker, Liney, Metcalfe & Holloway, 2014). Gradient strengths vary in time in the order of mT whereas static magnetic field range between 1T to 3T (Bernstein, King & Zhou, 2004). Therefore, even a small gradient nonlinearity would have a larger impact compared to those due to static magnetic field inhomogeneities.

When fast gradient switching is involved in the MRI acquisition sequence, these sequences are affected by eddy-currents which is another source of system-dependent distortions. Eddy currents lead to additional time-varying magnetic field gradients. Thus, the induced field gradients would lead to distortion in gradient waveforms (Schmidt & Payne, 2015) and undesirable image artifacts which are mostly present in diffusion-weighted MR imaging and in localized magnetic resonance imaging spectroscopy (Baldwin, Wachowicz, Thomas, Rives & Fallone, 2007, Spees et al., 2011). Therefore, eddy currents are not going to be discussed more in this section.

Gradient Nonlinearities

Gradient magnetic fields are used for encoding spatial information in MR images, thus, the inability of generating perfect gradients would result in inaccuracies in precise imaging. The gradient coils generating the gradient fields are designed such that gradient varies linearly with the position in the ideal conditions. However, in real practice, across the entire FOV, it is not always successful to keep this linearity since gradient fields are generated with short rise time, therefore the disengagement of this ideal relation would induce an in-plane distortion. The in-plane distortions due to non-linear MRI gradients can be roughly quantified as (Weygand et al., 2016):

$$\Delta x_{grad} = \frac{x \times \Delta G_{read}}{G_{read}}$$

where G_{read} represents the readout gradient strength, x the in-plane apparent position of the object, ΔG_{read} is the nonlinearity in gradients, and Δx_{grad} is the discrepancies in signal location between where it originates within the scanner to where the system perceives it to be representing the distortion due to nonlinearity in gradients.

Gradient nonlinearities are typically observed at large distances from the MRI system isocenter (Weygand et al., 2016). The greater loss of gradient linearity with the increase of radial distance causes blurring in the outer parts of the image. It is not limited to any spatial direction (Baldwin et al., 2007). Figure 14 shows the variation pattern of the nonlinearities in gradient with respect to the system isocenter.

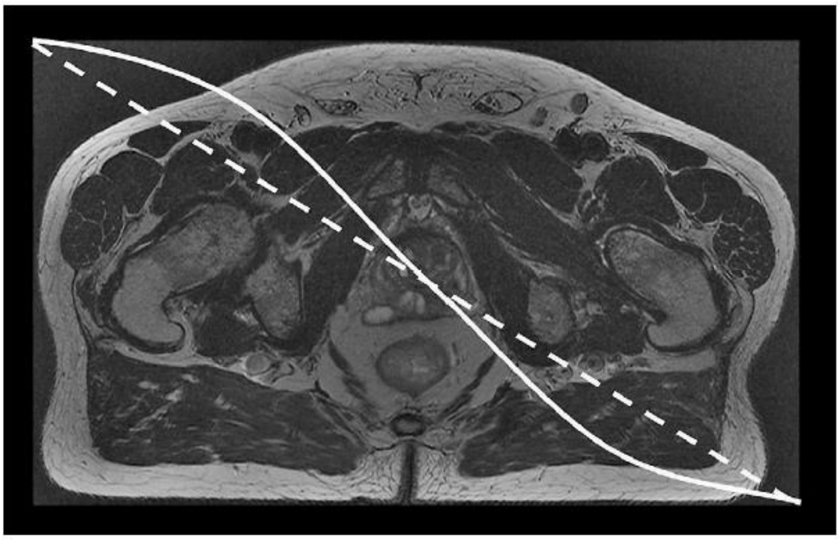

Figure 14 Representation of the spatial encoding gradient relationship with radial distance, dashed line shows the ideal linear gradient whereas solid line represents the non-linear gradient (Jamtheim Gustafsson, 2019)

It should be highlighted that the nonlinearity of gradients is the dominant source of geometric distortion (Weygand et al., 2016) with the reported values greater than 1 cm (Walker et al., 2015). It is definitely a concern especially for a large FOV in MRsI images.

Magnetic Field Inhomogeneities

Static magnetic field homogeneity is measured in parts per million (ppm) over a diameter of spherical volume which increases by extending out from the MRI system isocenter. MRI scanners operate with the assumption that B_0 is homogeneous. However, the generation of homogeneous B_0 within the entire FOV is not a realistic expectation. Therefore, the deviation of B_0 by a few ppm is possible depending on the measurement location (Weygand et al., 2016). Thus, the greatest homogeneity occurs in the isocenter and it decreases with increasing the distance from the isocenter. Inhomogeneities in B_0 can arise due to the improper adjustments of the shim coils, which are used for the regulation of the magnetic field homogeneity. Moreover, patient-induced distortions can also lead to magnetic field inhomogeneities.

Static magnetic field inhomogeneity cause dephasing of the individual spins. It is sequence-dependent and thus, can be reduced by using a shorter echo time. Different from the geometric distortions stemming from gradient non-linearities, deviations in the static magnetic field due to inhomogeneities give rise to geometric distortions in the direction of the applied spatial frequency-encoding gradient. The geometric distortion due to inhomogeneities in the magnetic field is dependent on the gradient strength used. Therefore, the in-plane shift arising from magnetic field inhomogeneities can be roughly quantified as (Weygand et al., 2016):

$$\Delta x_{field} = \frac{\Delta B_0(x,y,z)}{G_{read}}$$

where Δx_{field} is the magnitude of the in-plane shift, G_{read} is the readout gradient strength, and $\Delta B_0(x,y,z)$ represents the magnetic field inhomogeneity at a given point (x,y,z) in space.

2.3.2 Patient-Dependent Distortions

MRI patient-dependent distortions depend on the magnetic properties of the patient under scan. They can mainly stem from magnetic susceptibility and chemical shift effects. The patient-induced distortions are smaller in magnitude than system-induced distortions and they are more difficult to correct (Weygand et al., 2016). The patient-induced distortions also introduce imperfections in the homogeneity of B_0.

The magnitude of the patient-dependent distortions changes with the MRI acquisition sequence used and depends also on the field strength of the scanner. The difference between resonance frequencies of fat and water and also the distortions arising from susceptibility change increase with the field strength. Thus, patient-dependent distortions are greater in magnitude at higher field strength.

Magnetic Susceptibility

Magnetic susceptibility, denoted as χ, describes the capacity of a medium to become magnetized when placed in a magnetic field. Magnetic susceptibility of a medium is determined by the extent to which orbital angular momentum of electrons and spins of electrons and nuclei are influenced by the magnetic field.

There are mainly 3 groups describing the object's response to a magnetic field: diamagnetic, paramagnetic and ferromagnetic which differ in terms of their magnetic susceptibility value ranges. The human body is mainly diamagnetic due to its high water content. It also contains air spaces, which are paramagnetic in origin, and other various paramagnetic ions in position dependent concentrations. Due to the presence of different components with different magnetization properties within the human body, variations in magnetic susceptibility values lead to the disturbance of the static magnetic field locally. Therefore, different tissues create local magnetic changes, which lead to image distortion. When a material with magnetic susceptibility χ is placed in a magnetic field, B_0, the perturbed magnetic field, $B_{0,\text{ perturbed}}$, can be quantified in magnitude as (Weygand et al., 2016):

$$B_{0,perturbed} = (1 + \chi)B_0$$

The effect of magnetic susceptibility on the homogeneity of the B_0 scales with the static magnetic field strength.

The magnitude of the image distortion due to inhomogeneity of the magnetic field arising from variation in magnetic susceptibility is proportional to the difference in susceptibility. Accordingly, the geometric distortion due to magnetic susceptibility can be expressed as:

$$\Delta x = \Delta\chi \frac{B_0}{G_{read}}$$

where Δx is the displacement due to geometric distortion, and $\Delta\chi$ is the susceptibility difference. In order to be able to fully quantify the geometric distortions due to magnetic susceptibility effect, 3D patient's distribution of susceptibility values should be known in advance. It should be highlighted that the image distortion due to magnetic susceptibility effect can be very severe at the locations of implants or highly curved structures (Schmidt & Payne, 2015) and also at the interfaces between tissue and air or compact bone and soft tissue (Weygand et al., 2016). Since susceptibility-related geometric distortions are not scanner-related and may change depending on the imaged object. Therefore, modeling of susceptibility-induced distortions and their separation from B_0 inhomogeneities hold a crucial. The susceptibility simulations are commonly based on simplified tissue composition models, which include air, water, and some other tissues such as fat and blood importance (Kroll et al., 2019).

Chemical Shift

Chemical structures of water and fat are different in the sense that the electron density distribution of hydrogen atoms is different in these two materials. While water has an oxygen-hydrogen molecule structure, fat has a carbon-hydrogen structure. Therefore, these mediums with different chemical structures induce different degrees of shielding from the magnetic field. This causes hydrogen atom in fat and water to produce signals with slightly different frequencies. As the protons resonate at different frequencies depending on its medium, the apparent spatial location of a radiofrequency echo is shifted. Hydrogen atoms in fat have a slower precessing than those in water. This phenomenon is described with the term chemical shift (Schmidt & Payne, 2015, Weygand et al., 2016). It causes tissues containing fat to be shifted in the frequency encoding direction.

There are mainly 2 different categories of chemical shift-artifacts: first one due to different spinning frequencies of hydrogen atoms in different chemical environments and the second one due to rephrasing and dephasing of the radiofrequency echo in the B_0 direction. Chemical shift artifacts in the second kind occur due to the differences in precession frequencies causing the constructive and destructive interference of the transverse magnetization.

3 AIM OF THE WORK

The use of Magnetic Resonance Imaging (MRI) scanners in the radiotherapy treatment planning (RTP) is rapidly increasing due to its superior soft tissue contrast compared to computed tomography (CT), which enables accurate delineation of target and Organs at Risk (OAR) with less inter-observer variability (Adjeiwaah et al., 2019). Therefore, MRI has been the complementary imaging modality in treatment planning since the beginning of the 1990s (Dirix et al., 2014). The hybrid workflow of CT and MRI would allow one to have both a good soft tissue contrast for accurate contouring and information on electron density (for photon therapy) or proton stopping power ratio relative to water (for proton therapy), which enables dose calculations for treatment planning (Chandarana et al., 2018). However, due to the limitations of hybrid workflow arising from systematic spatial uncertainties due to image registration, patient exposure to ionizing radiation in the CT acquisition, inter-scanner differences between the two imaging sessions and overall cost considerations, MRI-only workflows have been introduced eliminating the use of CT in RTP. However, MRI introduces system-dependent and patient-dependent geometric distortions and geometric inaccuracies in the radiotherapy treatment planning images, which can have a severe effect in the case of proton therapy. MRI image distortions would cause radiation dose calculations on incorrect assumptions or treatment delivery in the wrong breathing phase (Paganelli et al., 2018, Schmidt & Payne, 2015). These would lead to insufficient irradiation of the tumor and over-dosage in normal tissues. Therefore, it necessitates quantifying the dosimetric uncertainties, which stem from the geometric inaccuracies in MR imaging in order to be able to safely benefit from the advantages that MRI-only workflow brings compared to the current clinical practice.

This work aims to quantify the dosimetric effect of geometric distortions arising from MRI in MRI-only workflow in the Intensity Modulated Proton Therapy (IMPT) on a thoracoabdominal phantom and clinical cases from the thorax and upper abdominal regions including the lung, liver, and pancreas. For this purpose, a study in collaboration with Ludwig-Maximilians University (LMU) Munich has been conducted. The clinical data has been provided by LMU university clinic and a digital breathing CT/MRI phantom of the thoracoabdominal site developed by Paganelli et al. (2017) is used for the phantom tests. In order to simulate the spatial distortion artifacts in MR images, deformation vector fields (DVFs) quantified on a self-designed distortion phantom developed by Kroll (2018) have been used. To simulate solely the dosimetric changes due to geometric distortions eliminating the inaccuracies arising from synthetic CT generation in MRI-only workflow, DVFs have been directly applied to the 4D CT patient scans and phantoms and dosimetric analysis is carried out on the distorted and undistorted scans.

MRI-only radiation therapy has been first introduced in the conventional radiotherapy treatment plans with a focus in the brain and prostate regions, and it is being studied in proton beam therapy in the last few years. The studies based on MRI-only workflow in the thoracoabdominal regions are limited. This study aims to assess the dosimetric impact of the geometric distortions arising from MRI to demonstrate if these distortions significantly affect the dose distributions in MRI-only proton therapy in the thoracoabdominal regions.

4 MATERIALS and METHODS

4.1 Image Datasets

In order to quantify the effect of spatial distortion artifacts in MR images on the radiation dose in MRI-only workflow, a digital breathing CT/MRI thoracoabdominal phantom and 4D CT clinical scans are used for the thorax (for lung) and upper abdominal (for pancreas and liver) regions. These datasets are described in detail in this section.

4.1.1 4D CT/ MRI Digital Phantom

Paganelli et al. (2017) developed a 4D CT/MRI Breathing Anthropomorphic Thorax (CoMBAT) phantom based on the extended cardiac-torso (XCAT) phantom (Paganelli et al., 2017). Their work aimed to develop a 4D CT/MRI digital phantom taking into account the organ motion due to respiration for the simulation of abdominal MR images covering the aspects of estimation of MR tissue parameters, simulation of MR pulse sequences and modeling of radiofrequency coil response and noise. In this thesis, the COMBAT phantom is used for the validation of the dosimetric effect analysis made in the thorax and upper abdominal clinical cases. In this section, generation of the COMBAT phantom is going to be discussed in more detail and afterwards the preparation steps applied on the phantoms in order to enable treatment planning (TP) are going to be described.

Generation of COMBAT Phantom

In the phantom, specific MR tissue parameters like relaxation parameters (T1 and T2) and proton density (ρ) values are estimated through MRI sequences acquired with a 1.5T scanner. In order to simulate MR sequences, three pulse sequences are performed. These sequences are categorized mainly based on their repetition time, T_R, and echo time, T_E, and can be listed as:

i. T_1-weighted spoiled gradient echo sequence (Volumetric Interpolated Breath-hold Examination: VIBE)
ii. T_2-weighted balanced steady-state free precession sequence (Fast imaging with steady state precession: TrueFISP)
iii. T_1-weighted fast low-angle shot sequence (FLASH).

The distortions at identical image resolution are highly influenced by the selected sequence. According to the experimental study conducted by Kroll (2018) with the two MR sequences, TrueFISP and FLASH, it has been reported that the mean in-slice landmark deformations stay below 1 mm in the FLASH sequence whereas TrueFISP mean deformations reach almost 2 mm at the outer boundaries (Kroll, 2018). Kroll et al showed that deformation levels are highly dependent on the applied distortion correction method and that 3D distortion correction (as applied in the FLASH sequence in the quoted study) is better performing. For this reason, the FLASH sequence has been selected for this work, as a representative MRI sequence to capture motion where 3D distortion correction is applied.

The COMBAT phantom is derived based on the XCAT phantom developed by Segars, Sturgeon, Mendonca, Grimes, & Tsui (2010), relying on 10 respiratory volumes of the entire thorax with a maximum motion of 15 mm in the superior-inferior (SI) direction. When acquiring an MR image, the time-space domain is sampled in the k-space domain and the phantom P(k, t) is described in k space as:

$$P(k,t) = R.F.[S(N_{coil}).T(T_1,T_2,\rho).C(T_E,T_R,\alpha).O(x,t) + n(x,t)]$$

where O(x, t) represents the 4D XCAT phantom in the time-space domain. According to this equation, T is the tissue contribution as a function of weighting parameters, C is the applied MR sequence as a function of $T_E, T_R, and\ \alpha$, n is the noise model in time-space domain and S is the term describing the sensitivity of the N readout coils. The implementation of these operations is carried out as follows:

i. Organs O(x,t): 4D XCAT phantom developed by Segars et al. (2010) incorporates 16 distinct tissues some of which are water, fat, heart and kidney and two parameters for background and air.

ii. Tissue parameters, $T(T_1,T_2,\rho)$ and MR sequences (T_E,T_R,α) : tissue appearance in MR image is dominated by the terms T_1, T_2, and ρ. All tissue types are assigned specific T_1, T_2 relaxation time and ρ parameters with reference to the acquired MRI scans. For the VIBE sequence, the signal equation C is expressed with the acquisition parameters $T_E, T_R, and\ \alpha$ and tissue-specific T1, T2 and ρ values as:

$$C = \frac{\rho\, sin\alpha\, (1 - e^{-\frac{T_R}{T_1}})}{1 - cos\alpha e^{-\frac{T_R}{T_1}}} e^{-\frac{T_E}{T_2}}$$

For the FLASH sequence, which is used in the context of this thesis, the signal intensity equation can be derived similarly to the VIBE sequence (Kroll, 2018).

iii. Coil operator S and noise n: sensitivity maps, denoted by the operator S, has the shape of a linear fall-off for the coils. Eight coils ($N_{coils} = 8$) are placed uniformly on a circle around the abdomen and the MR image is computed by summing up over all the sensitivity maps of the eight coils applied to the MR signal. The noise, n, has a Gaussian shape.

iv. 3D Fourier Transform, F, and sampling, R: The time-space domain is transformed into the k-space domain by Fourier Transform. After the transformation into k-space, it is sampled differently depending on the sampling approach used for the selected sequence.

The phantom dataset is composed of phantoms of the thorax and upper abdomen including the lung, liver and pancreas regions. Figure 15 and Figure 16 show respectively the simulations of CT images and corresponding MRI images of lung region in the exhale phase of the respiration.

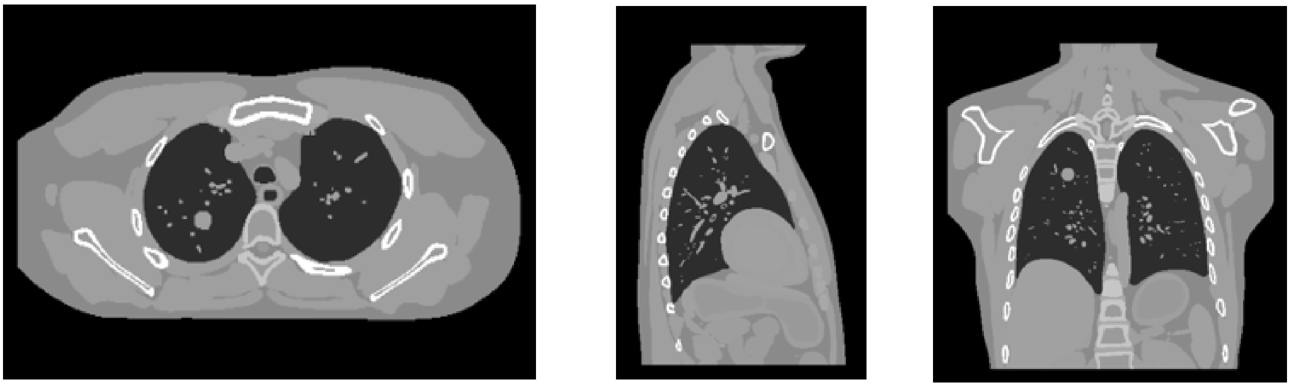

(a) (b) (c)

Figure 15 CT images of lung phantom (a) axial plane (b) sagittal plane (c) coronal plane views

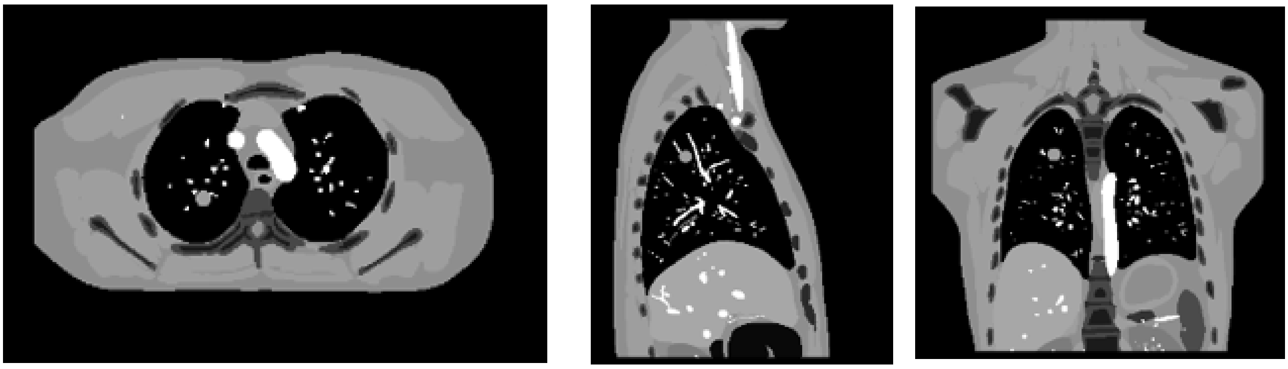

(a) (b) (c)

Figure 16 Corresponding MR images of lung phantom (a) axial plane (b) sagittal plane (c) coronal plane views

Simulations of upper abdomen CT images for the liver and pancreas regions are shown in Figure 17.

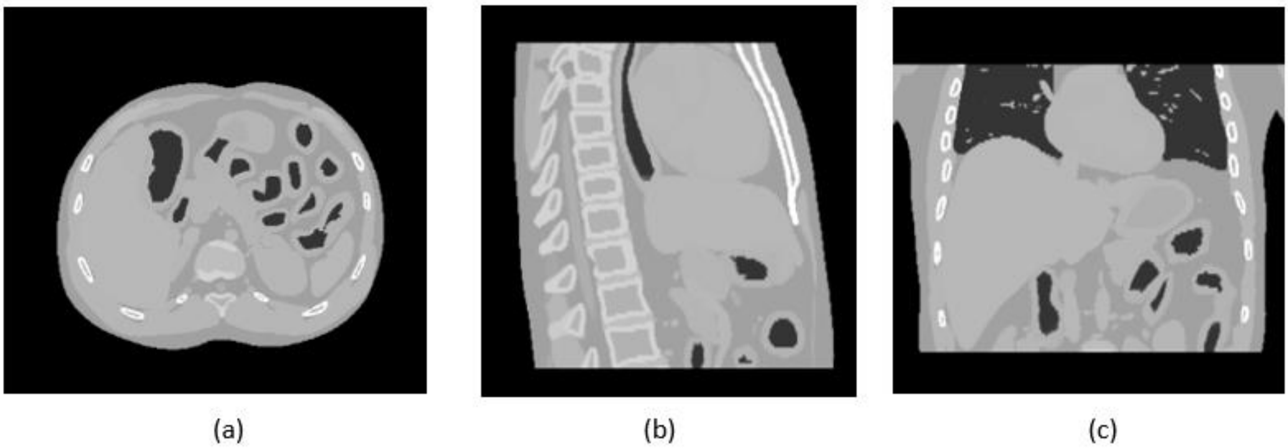

Figure 17 Upper abdomen phantom (a) axial plane (b) sagittal plane (c) coronal plane views

COMBAT Phantom in TP

In order to be able to perform the dose calculation in proton therapy, Hounsfield Unit (HU) to relative stopping power ratio conversion is required. HU are dimensionless numbers used to express CT numbers in a standardized way according to a linear density scale and the HU densities of the tissues reflect their attenuation of x-ray. Hounsfield units of the tissues are obtained from the linear transformation of the attenuation coefficients based on the densities of pure water and air. Therefore, it necessitates converting the intensity values of the XCAT phantom into the HU scale first. For this conversion the following formula is used (Lev & Gonzalez, 2002):

$$HU = 1000 \times \frac{\mu_{tissue} - \mu_{water}}{\mu_{water}}$$

where μ represents the attenuation coefficient and attenuation coefficient of water is arbitrarily assigned as 0 HU.

In order to make treatment planning and perform dose analysis on the phantoms, the phantoms are manually contoured in MATLAB (The MathWorks, Inc.) based tool, Computational Environment for Radiological Research (CERR) which is developed for radiation therapy treatment planning and imaging informatics. Contouring is made using the structure delineation tool of CERR.

In this study, two lung phantoms, which have tumors at different locations inside the lung, are used. While in the first lung phantom, the tumor is close to soft tissue, in the second lung phantom, a tumor, which is isolated in the lung parenchyma and far from the soft tissue, is created. These two lung phantoms differ in the sense that the distal end of their final dose distribution where we have the prescribed dose ends either close to soft tissue or inside the lung parenchyma away from the soft tissue. By simulating two different tumor location scenarios in the lung, it has been aimed to demonstrate properly the dosimetric impact of geometric distortions in the lung region independent of the tumor location. Figure 18 shows both of the lung phantoms in HU with manually delineated contours and tumors at different locations.

(a) (b)

Figure 18 Manually contoured two lung phantoms which have tumors at different locations. The contours in the images are skin: in yellow, tumors: in blue, lungs: in green and spinal cord: in purple

Figure 19 shows the phantoms in HU with manually delineated contours in the liver and pancreas cases.

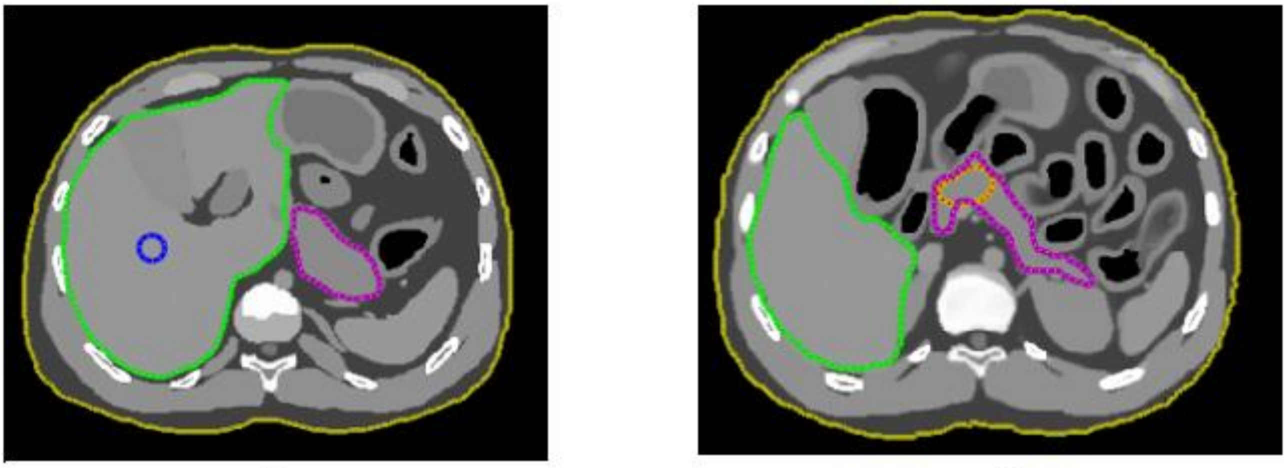

(a) (b)

Figure 19 Manually contoured (a) liver phantom (skin: in yellow, tumor: in blue, pancreas: in purple, liver: in green) and (b) Pancreas phantom (skin: in yellow, tumor: in orange, pancreas: in purple, liver: in green)

4.1.2 4D CT Clinical Dataset

The clinical dataset is provided by the Ludwig-Maximilians University (LMU) university clinic, and it consists of CT scans of the thorax and upper abdominal regions. Organs in the thorax and abdominal regions are subject to intra-fractional organ motion due to respiration, so motion should be compensated in the RTP in these body regions for a conformal treatment. Therefore, 4D CT scans are used in order to be able to visualize the full extent of the tumor motion and plan the treatments accordingly. Thorax region dataset consists of 4D CT scans of 10 patients with lung cancer and the abdominal region dataset consists of 4D CT scans of 4 patients with liver cancer and 4 patients with pancreas cancer. Abdominal compression is applied during the acquisition on the patients with liver cancer in order to reduce the diaphragm motion. Each patient data includes 10 respiratory phase volumes, and an average CT volume, which represents the mean position of the anatomy during the breathing cycle and is used for treatment planning. The respiratory phase volumes are tagged with a percentage indicating the amplitude percentage with respect to the maximum amplitude of the respiratory signal. The patient data from the clinic also includes the tumor and the organs at risk contours contoured by an expert on the average CT. Figure 20 shows an example of the clinical dataset with the axial plane views of the lung, liver and pancreas cases respectively from left to right:

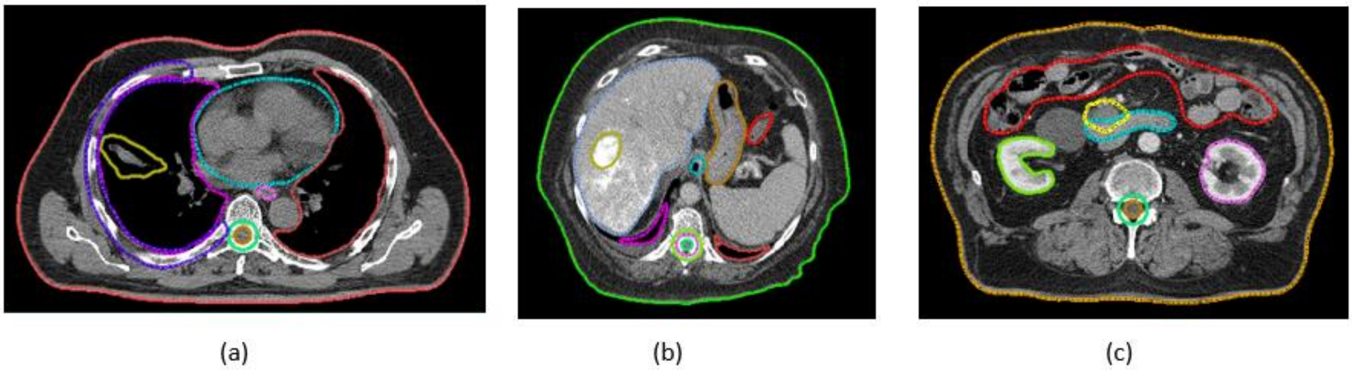

Figure 20 An example from the clinical dataset with the axial plane views of (a) lung case (b) liver case and (c) pancreas case where Internal Target Volumes (ITVs) are contoured in yellow in the images

4.1.3 Processing of the Image Dataset before TP

Before proton therapy treatment planning is carried out, both phantom and clinical data images and their contours are processed in order to fit them into a standardized format. These steps include the resampling, cropping the image frames only including the boundaries of the body volume and making the image dimension the same in the whole dataset by locating the cropped and resampled images with their isocenters at the origin in a big mask with a determined dimension. Resampling is performed to make the spacing uniform throughout the whole dataset. Image cropping has been necessary to eliminate the redundant information in the images and to keep only the parts of the image, which are necessary for treatment planning. It is based on including only the boundaries of the body volume and eliminating the arms of the patient if they lay along the body's side and the abdominal plate, if present in the image. In the final step of standardization, the resampled and cropped images are located in a big mask, with its background assumed to be air. It has the dimensions of 550 x 450 x 251 voxels, which is chosen taking into account the whole dataset and considering that the resampled and cropped images comprising the useful information can fit inside. The image is located such that its isocenter is at the origin in order to make sure that the deformation vector field application, as will be covered in the following sections, is uniform over all the images.

All these processing steps are applied on the contours as well as on the average planning CTs and at the end all the images have 550 x 450 x 251 voxels and spacing of [1.074 1.074 3] mm, which is the spacing in the majority of clinical images in the dataset, with their isocenter located at the origin. These steps are all performed in MATLAB. Resampling is computed using Plastimatch version 1.8 which is an open-source software developed for radiotherapy image processing with a plug-in property for MATLAB (Plastimatch, n.d.).

4.2 Utilized Software

In this section, the software used in proton therapy treatment planning and image processing is going to be introduced. These softwares are CERR, Raystation, and Plastimatch.

4.2.1 CERR

Computational Environment for Radiological Research, CERR, is a software environment, developed as a plug-in for MATLAB that provides a platform for treatment planning research (Deasy, Blanco, & Clark, 2003). The open-source software is developed for photon therapy and it is partly extended at the Technical University of Munich (TUM) and LMU enabling treatment planning and simulation in particle therapy. It provides an environment for treatment planning and its analysis with several integrated tools such as importing patient geometry, 3D visualization of the images, dose calculation, optimization of beam delivery, exporting treatment plans with calculated doses, structure delineation and analysis, and dose comparison. In this project, TP and dose evaluation with Dose Volume Histograms (DVH) are carried out in CERR. Figure 21 shows the user-interface of CERR with the main panel.

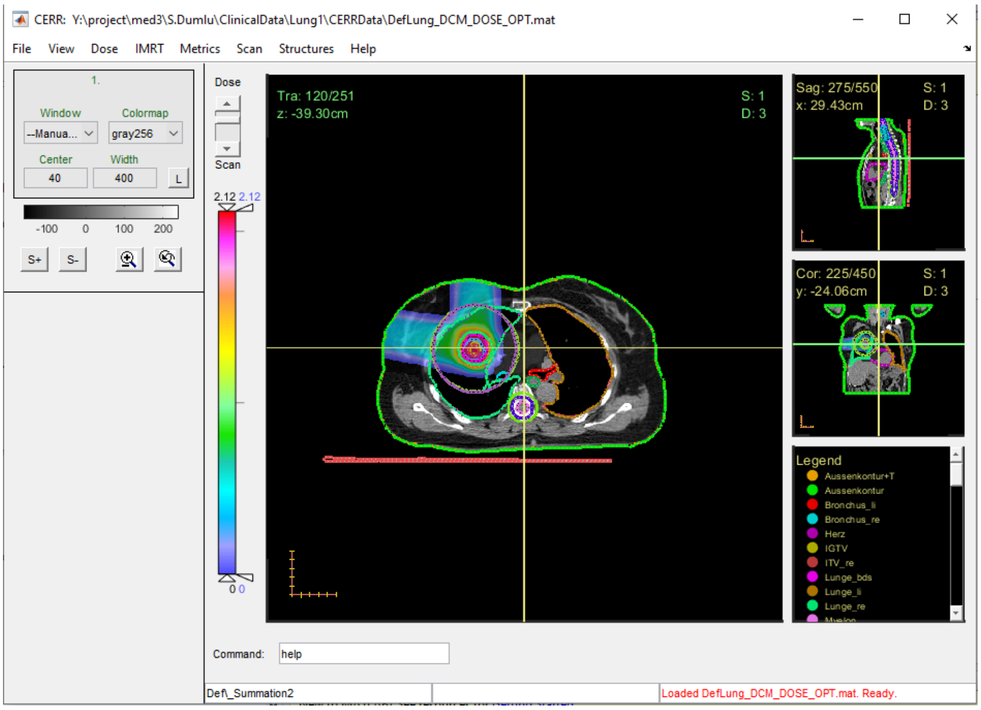
CERR: Y:\project\med3\S.Dumlu\ClinicalData\Lung1\CERRData\DefLung_DCM_DOSE_OPT.mat

Window: --Manua...
Colormap: gray256
Center: 40
Width: 400

Command: help

Defl_Summation2

Loaded DefLung_DCM_DOSE_OPT.mat. Ready.

Figure 21 User Interface of CERR Software Platform

The next figure, Figure 22, shows the Intensity Modulated Proton Therapy (IMPT) window in CERR, which enables us to choose the beam modality and to set the determined beam angles, various TP parameters, the targets, and external contour.

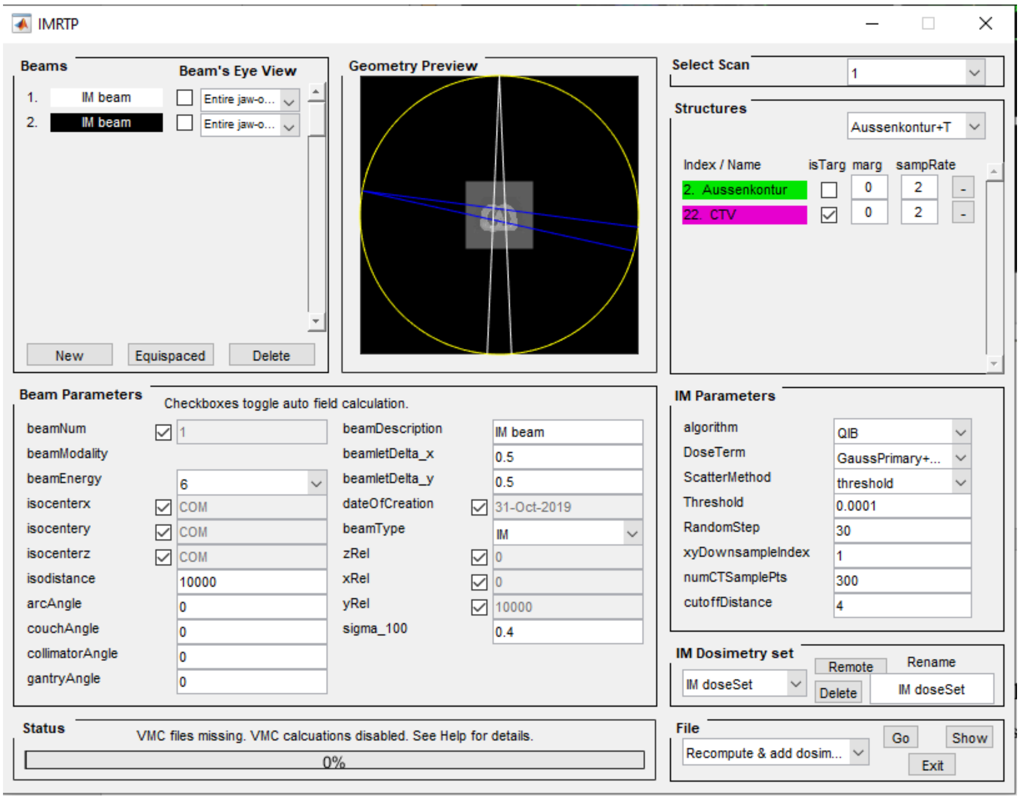
IMRTP

Beams
1. IM beam ☐ Entire jaw-o...
2. IM beam ☐ Entire jaw-o...

Select Scan: 1

Structures: Aussenkontur+T

Index / Name | isTarg | marg | sampRate
2. Aussenkontur ☐ 0 2
22. CTV ☑ 0 2

Beam Parameters
Checkboxes toggle auto field calculation.

beamNum ☑ 1
beamModality
beamEnergy 6
isocenterx ☑ COM
isocentery ☑ COM
isocenterz ☑ COM
isodistance 10000
arcAngle 0
couchAngle 0
collimatorAngle 0
gantryAngle 0

beamDescription IM beam
beamletDelta_x 0.5
beamletDelta_y 0.5
dateOfCreation ☑ 31-Oct-2019
beamType IM
zRel ☑ 0
xRel ☑ 0
yRel ☑ 10000
sigma_100 0.4

IM Parameters
algorithm QIB
DoseTerm GaussPrimary+...
ScatterMethod threshold
Threshold 0.0001
RandomStep 30
xyDownsampleIndex 1
numCTSamplePts 300
cutoffDistance 4

IM Dosimetry set: IM doseSet
Rename: IM doseSet

Status
VMC files missing. VMC calcuations disabled. See Help for details.
0%

File: Recompute & add dosim...

Figure 22 CERR user interface for IMPT

4.2.2 Raystation

Raystation is a commercial Treatment Planning System developed by Raysearch Laboratories (Stockholm, Sweeden). It provides a software platform to develop advanced TP with different beam modalities, photons and protons, and various functionalities such as dose calculation, image registration, robust optimization, treatment adaptation, dose analysis and structure delineation with the extended features like generation of beam-specific margin ROI, and contouring with structure templates present in the software. In this project, Raystation is used in the beam specific PTV generation. Figure 23 shows the user interface of the Raystation TP software.

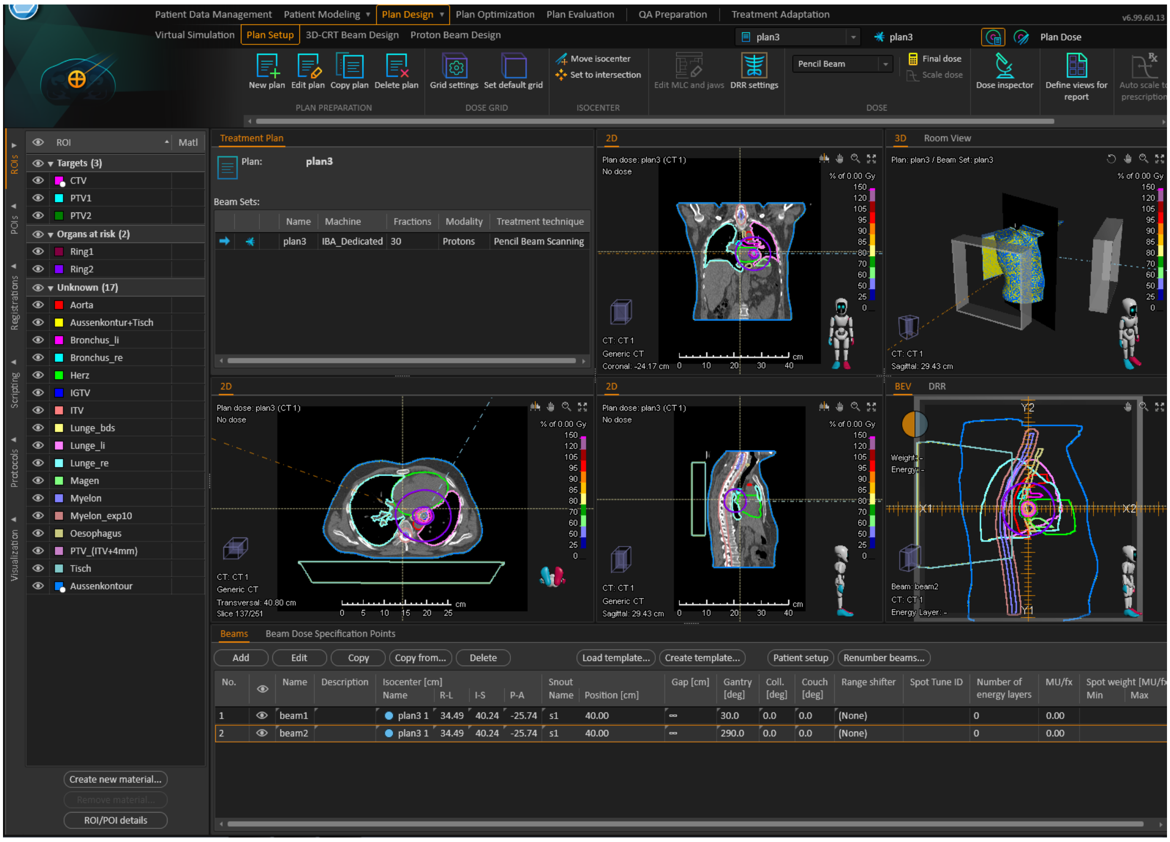

Treatment Plan

Plan: plan3

Beam Sets:

			Name	Machine	Fractions	Modality	Treatment technique
			plan3	IBA_Dedicated	30	Protons	Pencil Beam Scanning

No.		Name	Description	Isocenter [cm] Name	R-L	I-S	P-A	Snout Name	Position [cm]	Gap [cm]	Gantry [deg]	Coll. [deg]	Couch [deg]	Range shifter	Spot Tune ID	Number of energy layers	MU/fx	Spot weight [MU/fx] Min	Max
1		beam1		plan3 1	34.49	40.24	-25.74	s1	40.00	∞	30.0	0.0	0.0	(None)		0	0.00		
2		beam2		plan3 1	34.49	40.24	-25.74	s1	40.00	∞	290.0	0.0	0.0	(None)		0	0.00		

Figure 23 User interface of Raystation TPS

4.2.3 Plastimatch

Plastimatch is an open-source software for image computation (http://plastimatch.org/). A variety of useful tools for radiotherapy research and clinical practice are in Plastimatch. In this work, Plastimatch is used for resampling, conversion of files from one format to another, and apply deformation field on the CT, which simulates the geometric distortion of MRI.

4.3 Treatment Plan Design

In this section, the designed treatment plan is going to be discussed with a focus on motion compensation methods, target volume definition and OAR sparing approaches, dose-prescription, field set-up details and optimization method. The treatment plan design used in this study is summarized with a schematic in Figure 24. It shows the general workflow of the treatment plan. The treatment planning workflow developed for the determination of the dosimetric effect of geometric distortions and the evaluation methods for the assessment of the dosimetric effects are going to be discussed in more detail in the next sections.

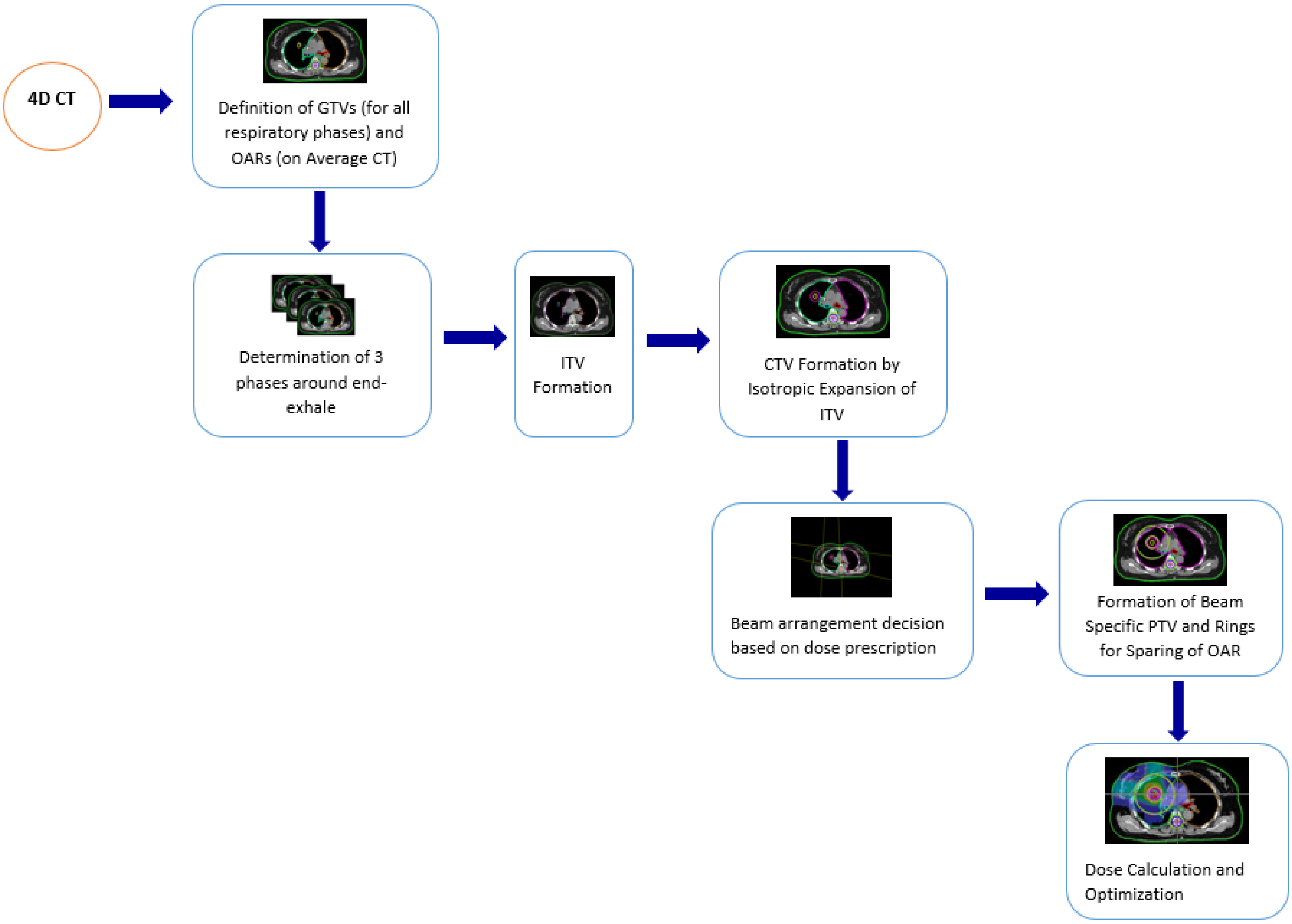

Figure 24 Treatment planning workflow used in this study

Treatment planning is performed for IMPT using the pencil beam scanning technique. It has been discussed in detail in the Introduction section that there are many sources of uncertainties in proton therapy, which require special and distinct approaches to be successfully managed in treatment planning and delivery. In this work, margin-based approaches are considered in order to compensate for the uncertainties due to motion, set-up uncertainties and range calculation in the TPS.

4.3.1 Motion Compensation

The body regions of interest in this study, lung, liver, and pancreas, are highly subject to intra-fractional motion due to respiration. Therefore, for a conformal treatment to prevent under- or over-dosage in the target and over-dosage in the nearby healthy tissues, motion compensation is applied in the treatment planning with 4D simulation. The clinically contoured tumor regions are the GTV contours defined on the 10-phases 4D CT and on the average CT. In order to be able to compensate for the motion effect, 3 GTVs around the end-exhale phase are combined to generate Internal Target Volume (ITV). This is to simulate a possible gating treatment at the exhale phase, which is the respiratory phase where the tumor position is more stable and repeatable. In order to correctly determine the GTVs around end-exhale, the isocenters of the GTVs belonging to 10 respiratory phase bins are found. Accordingly, 3 GTVs around the end-exhale are determined and these GTVs are combined to form the ITV for respiratory gating. The same approach is applied to phantoms. Figure 25 demonstrates the ITV approach with the 3 GTVs and the generated ITV.

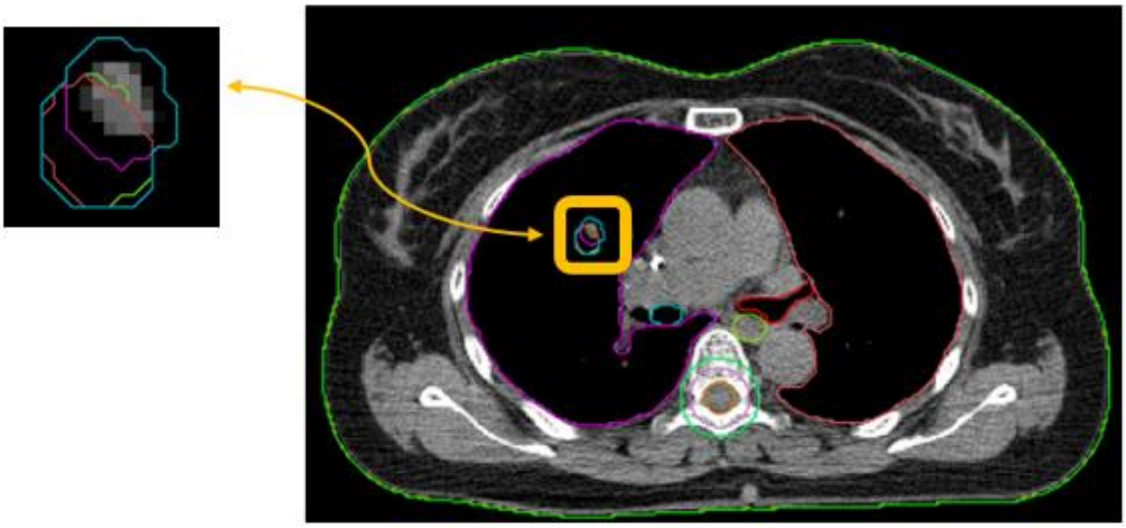

Figure 25 Generation of the ITV (in blue) by the combination of 3 GTVs around end-exhale phase (in red, pink and green)

4.3.2 Target Volume Definition

After the ITV generation, CTV is generated by the isotropic expansion of ITV. For ITV to CTV expansion, based on studies of Yixiu et al. (2017) (lung case), Hong et al. (2014) (liver case) and Jethwa et al. (2018) (pancreas case), 8 mm margin is used in all of the body regions.

Proton therapy is subject to range calculation uncertainties in the TPS due to the finite range of proton beams. Commonly used PTV generation approaches based on the isotropic margin expansion cannot adequately account for the changes in tissue densities due to range uncertainties. Therefore, it necessitates generating beam-specific PTV (bsPTV) for a robust proton treatment plan that can account for the change in tissue density along the beam path due to range uncertainties (Park et al., 2012).

Beam-specific PTV Generation

Different studies on the treatment margins have concluded that simple isotropic expansion of CTV volumes to create PTV is inadequate in proton therapy treatment planning (Moyers, Miller, Bush, & Slater, 2001, Engelsman & Kooy, 2005). Beam specific PTV is generated following the approaches of Moyers et al. (2001) and Paganetti (2012).

For the generation of the beam specific PTV, firstly the optimal beam angles which satisfy the dose prescriptions are determined for each case based on the treatment planning made with CTV as target. In the design of bsPTV, two uncertainties are taken into consideration: set-up error and systematic range uncertainties. These uncertainties are accounted for with margins applied to the CTV volume in different directions. Firstly, CTV is expanded in the lateral direction with respect to the beam's eye view in order to incorporate the set-up error margin into the bsPTV. In this study, a standard set-up error margin of 3 mm is considered for all the cases. Next, in order to encompass systematic range calculation uncertainties, which arise from the calibration curve to convert HU values to proton stopping power and HU values themselves, CTV is expanded in distal and proximal directions with respect to the beam's eye views. To determine the distal and proximal margins, firstly Water Equivalent Thickness (WET) of the distal and proximal ends of the CTV target with respect to the beam's eye view are calculated using radiological depth calculation function in CERR software. Afterward, assuming a proton range uncertainty of 3.5 % of the range plus an additional 3 mm (Paganetti, 2012, Moyers et al., 2001), the distal margin (DM) and proximal margin (PM) are calculated as

$$DM = 0.035 \times (distal\ CTV\ depth) + 3\ mm$$

$$PM = 0.035 \times (proximal\ CTV\ depth) + 3\ mm$$

Distal and Proximal CTV depths are taken as the highest and smallest values of the water-equivalent range (radiological depths) of the CTV contour on the beam path respectively.

After the determination of radiological WET of the CTV in CERR, bsPTV is generated in Raystation with the structure definition with beam specific margin functionality using the calculated margins in lateral, distal and proximal directions. After the beam specific PTV generation, sparing of OAR is ensured by a ring generated based on the bsPTV.

Sparing of OAR

Healthy tissues nearby the tumor volume and OAR are aimed to be spared from the proton dose by defining a ring concentric to the bsPTV with the patient specific dimensions. The ring has been created by the isotropic expansion of bsPTV, excluding the bsPTV inside, with the dimensions ranging from 3 cm to 4 cm for the lung and the pancreas cases, and 3 cm for the liver cases. These dimensions are determined patient-specific depending on the location of the tumor and the presence and distance of the OAR nearby. Figure 26 below shows a case with all the margins including ITV, CTV, beam specific PTVs and OAR rings for a treatment plan with two beams.

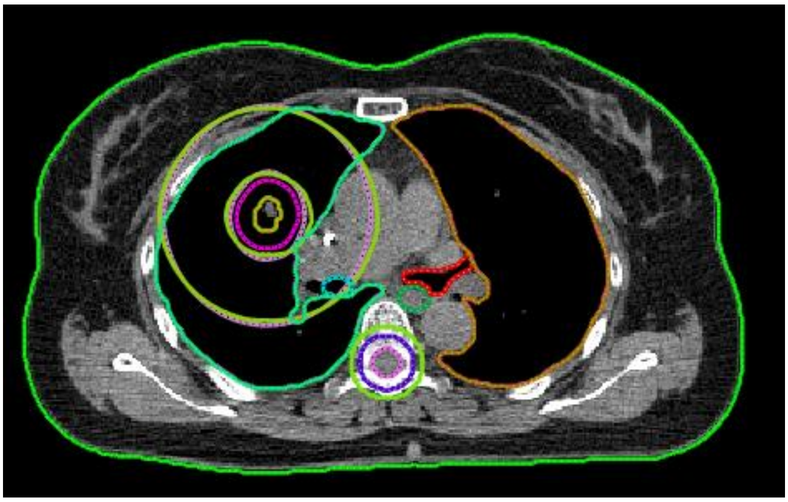

Figure 26 An example from the patient lung cases on which all the margins are shown. ITV: in yellow, CTV: in purple, bsPTV and OAR for beam 1: in light purple, bsPTV and OAR for beam 2: in green. Since OAR rings are generated from the bsPTVs, in the figure inner ring of OAR sparing rings represent bsPTVs

4.3.3 Field Set-Up and Dose Prescriptions

Before the bsPTV generation, field set-up designs meeting the desired dose prescriptions in the target are determined for each case in the dataset. These treatment plans are designed on average CT based on the CTV volume as the target and the OAR ring expanded from CTV as non-target volume and the distal and proximal margins necessary for bsPTV generation are determined based on these treatment designs. The real treatment plans designed to determine the dosimetric impact of geometric distortions are planned based on bsPTVs as target and OAR ring expanded from bsPTVs as non-target volume and evaluated on the

CTV. The details of this workflow are going to be discussed in more detail in the 'Determination of Dosimetric Impact of Geometric Distortions' section.

Proton treatment plans are designed and dose simulations are made in CERR. Characteristics of the treatment plan design used in this study are summarized in Table 1.

Table 1 Treatment Plan Design Characteristics

Parameter		**Value**
Beam Energy Range		70 - 250 MeV
Prescribed Dose (per fraction)	***Lung Cases***	2 Gy
	Liver Cases	2 Gy
	Pancreas Cases	3 Gy
Dose Grid Resolution		2 x 2 x 2 mm^3

The field set-up characteristics and dose prescriptions are different in each body region. The gantry angles are determined case by case. The final dose distributions with the determined optimal gantry angles for each case are shown in Appendix B, Appendix C and Appendix D. The beam angles are set relative to the isocenters of the target volumes. Optimization functions have been set for the mean dose in the target and non-target structures and the suitable field set-up for each case has been decided by conforming that the resulting distribution fulfill the dose criterions, which include min and max dose on the target CTVs, $D_{min, target}$, and $D_{max, target}$, and mean and/ or maximum dose on the nearby OAR.

Lung Cases

The tumor location in lung cancers shows high variability. Therefore, while determining the optimal field set-up for this patient group, it has been paid attention to shooting from the possible shortest distance to the tumor, avoiding shooting through the bones, the contralateral lung, and the heart. However, it was hardly possible to avoid a shoot through the bones due to the rib covering the lungs. In all of the cases, two beam fields are used which are shown in Appendix B. Dose prescription criteria on maximum dose to heart and esophagus were not feasible for some of the lung cases in which OARs are adjacent to the tumor. Dosimetric constraints followed RTOG 1308 for OARs. Constraints defined in lung cases are summarized in Table 2.

Table 2 Target and OAR Dose Constraints for Lung Cases

Constraint	Value (Gy)
Min Dose to Target ($D_{min,\ target}$)	1.475
Max Dose to Target ($D_{max,\ target}$)	2.125
Mean Dose to Heart	0.800
Max Dose to Spinal Cord	1.540
Mean Dose to Esophagus	1.045

Liver Cases

For the liver cases, the beam arrangement is designed with two beams, one in the lateral direction and the other in the anterior direction (Raldow, Lamb & Hong, 2019). The beam angles set in the four liver cases are $0° - 275°$, $10° - 275°$, $0° - 280°$ and $0° - 280°$, respectively and $10° - 275°$ for the liver phantom. The target and OAR constraints defined in liver cases are summarized in Table 3.

Table 3 Target and OAR Dose Constraints for Liver Cases

Constraint	Value (Gy)
Min Dose to Target ($D_{min,target}$)	1.575
Max Dose to Target ($D_{max,target}$)	2.125
Mean Dose to Right Kidney	0.800
Max Dose to Spinal Cord	1.540
Mean Dose to Stomach	0.800
Mean Dose to Large Intestine	0.800

Pancreas Cases

For the beam arrangement and dose constraints in the pancreas cases, the approach proposed by Dreher et al. (2015) for IMPT has been followed making it specific to each patient case confirming that the plan meets the constraints. Two oblique fields have been used for TP. The beam angles set in the four clinical pancreas cases are $150° - 240°$, $150° - 240°$, $120° - 220°$, and $120° - 240°$ respectively and $150° - 240°$ for the pancreas phantom. The target and OAR constraints defined in pancreas cases are summarized in Table 4 (Dreher et al., 2015).

Table 4 Target and OAR Dose Constraints for Pancreas Cases

Constraint	Value (Gy)
Min Dose to Target (D$_{min, target}$)	2.666
Max Dose to Target (D$_{max, target}$)	3.210
Mean Dose to Right & Left Kidney	0.800
Max Dose to Stomach	1.333
Max Dose to Large Intestine	1.333
Max Dose to Spinal Cord	1.600
Mean Dose to Liver	0.666

4.3.4 Optimization

After the steps of contour delineation, beam arrangement and target volume and OAR sparing ring definition, dose calculation and optimization are computed in CERR. The dose calculation algorithm aims to calculate the distribution of absorbed radiation dose in the patient based on the interactions of the beam with the tissues on which it passes through. Optimization methods are intended to optimize the incident directions of external radiation fields and intensities to meet the dose prescriptions in the tumor and surrounding healthy tissues. The main purpose of the optimization is to determine the appropriate intensities or weights of scanning spots within the target volume that give a dose distribution closest to the planned dose in the target minimizing the dose in the healthy tissues.

Each beam is divided into finite-sized beamlets in IMPT. The dose is calculated as

$$D_i = \sum_j d_{ij} w_j$$

where D_i is the dose at the voxel i, d_{ij} is the dose delivered at beamlet j to voxel i and w_j is the beamlet weight. Optimization algorithms aim to optimize the weights of the beamlets to produce a fluence map for every beam. Fluence maps are a set of beam weight distributions and are optimized to produce the desired dose distribution. Fluence is optimized by minimizing an objective function, F. Therefore, the aim is to find the set of weights that minimizes the objective function. F is defined as

$$F = \sum_i f_i$$

in which i is the anatomical structure with the objective function f_i.

In this treatment plan design, optimization is based on the prescription of the mean dose for the target volume, values of which are given above for different regions and 0 Gy dose for the OAR ring. The number of iterations that the TPS software should refine the optimization is set with the optimization parameter “maximum number of iterations”. In this plan, the maximum number of iterations is set to 200. At the end of the optimization step, when the optimization reaches the optimal solution with the defined number of maximum iterations, and the treatment is feasible for delivery meeting the dose prescriptions, the final dose distribution is determined.

4.4 Simulation of Distortion Aspects of MRI-Only Workflow

In order to simulate the distortion aspects in an MRI-only workflow and evaluate its impact on the planned dose distribution, an approach is developed in which CT images are distorted using the MRI displacement map and treatment planning is made on these CT images. This approach allows quantifying the dosimetric effect of MRI system-induced and patient-induced distortions separating it from dosimetric discrepancies arising from inaccuracies in synthetic CT generation. The uncertainties arising from the synthetic CT generation is out of the scope of this work. The details of the approach developed for the determination of the impact of these distortions on the planned dose distribution is going to be discussed in the next section. In this section, the details of the quantification of the MRI deformation field and development of displacement map by Kroll (2018) and its application on the CT images allowing to simulate the distortion aspects in MRI-only workflow are going to be discussed.

4.4.1 Quantification of Deformation Field

The displacement map representing the spatial distortion artifacts in MR-images is developed by Kroll (2018) in which these artifacts are experimentally quantified using a self-designed distortion phantom (Kroll, 2018). In this section, her approach is going to be explained in detail.

Analysis of MR images is done for the two MRI acquisition sequences, TrueFISP and FLASH and it has been highlighted that MRI sequences greatly affect the distortions at identical image resolution. Images acquired with the TrueFISP sequence suffer from relatively higher artifact level and contrast problems. The quantified displacement map, represented as Deformation Vector Field (DVF), comprises deformations due to gradient nonlinearities, static magnetic field inhomogeneities and patient susceptibility variations. The work by Kroll (2018) enables the user to investigate four different distortion combinations, each for a 2D FLASH and a 2D TrueFISP sequences: the total deformations as registered using a conventional 2D imaging sequence, the B0 and susceptibility related distortions in x-direction, the gradient induced distortions in x-direction and the susceptibility effects in z-direction. In this work, DVF arising from all the uncertainty sources is considered in order to evaluate the dosimetric effects due to both system-dependent and patient-dependent distortions in MRI.

Magnetic field (B-field) alterations within an MRI scanner are modeled by the measurement of the B-field in a self-designed distorted phantom. The phantom has four physically aligned modules, which have distortion grids inside with an aquarium outer structure. MR signal is created by filling in the aquarium with water. Figure 27 shows the design of the four modular phantom.

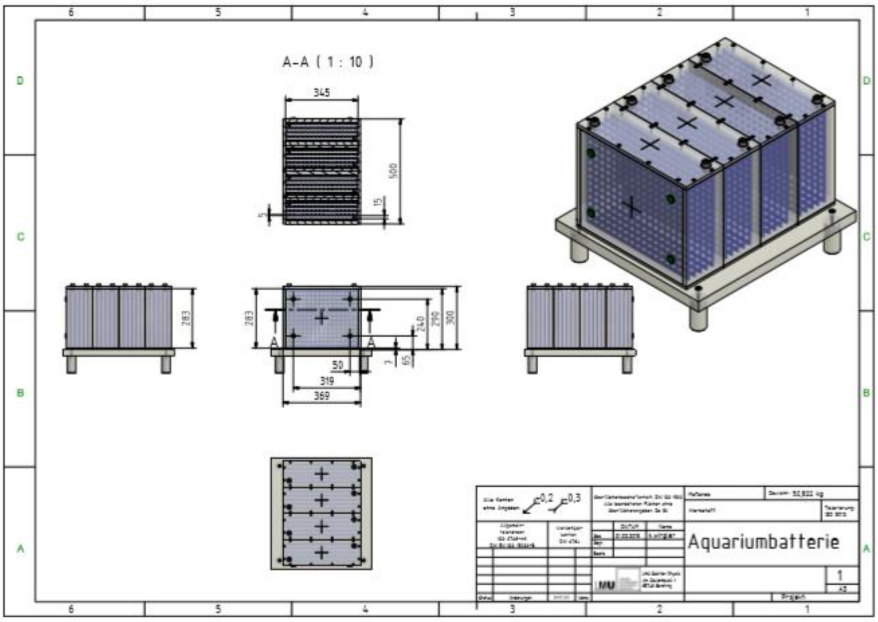

Figure 27 Construction sketch of the four modular phantom with total dimensions of (369×300×500) mm3. Each phantom subunit houses 5 distortion grids and can be filled with water. (Kroll, 2018)

In the final step, in order to evaluate and quantify the distortions, firstly, the CT of the phantom is acquired and afterwards the water-filled phantom is imaged with MR using two sequences. CT acquisition is done to verify that the digital model of distortion phantom accurately represents the real distortion grid since geometric inaccuracies will only lead to very small deviations in CT compared to the deviations in MRI. The acquired MRI images suffer from distortions increasing with the distance from the static magnetic field’s isocenter.

In order to extract the deformation field from CT and MRI images two-step image registration is performed: rigid registration to remove all the misalignment between model and image caused by experimental conditions and non-rigid registration in order to determine the discrepancies between the phantom model and real model in CT-image and the image distortions and inaccuracies of the phantom model in case of the MR-image.

In the end, the mean deformation is determined in mm within each slice in the z-direction. A maximal mean landmark deformation per image slice of up to 3 mm in slice selection direction is introduced in the FLASH sequence at a slice shifted 105 mm away from the isocenter. While for the TrueFISP sequence, mean in-slice landmark deformation reaches almost to 2 mm at the outer boundaries, it stays below 1 mm for the FLASH sequence.

4.4.2 Application of Deformation Field

In order to be able to simulate the distortion aspects of MRI-only workflow due to system-dependent and patient-dependent geometric uncertainties, the FLASH sequence deformation vector field quantified by the experimental study by Kroll (2018) is used. The deformation vector field is applied to the clinical CT images and to the phantom data creating distorted CT images. Therefore, this approach enables simulating the distortion aspects of MRI-only workflow enabling treatment planning and dose simulation such that the relative stopping power ratio necessary for TP is obtained from the CT images and the demonstration and evaluation of the dosimetric effects of geometric distortion in MRI is provided by the application of the quantified displacement map coming from MRI to CT scans.

DVF is applied to all of the images in the dataset. The isocenter of the DVF is located at the origin as in the images in the dataset and the spacing in DVF is set to [1.074 1.074 3] mm, the same as in the dataset. DVF is linearly interpolated to match the pixel dimensions of the CT images. The DVF is then applied to the images relying on Plastimatch. It is of importance that the identical MRI sequence and DVF are applied to the phantoms and the clinical data. Figure 28 shows the visualization of clinical lung CT data with the deformation field added.

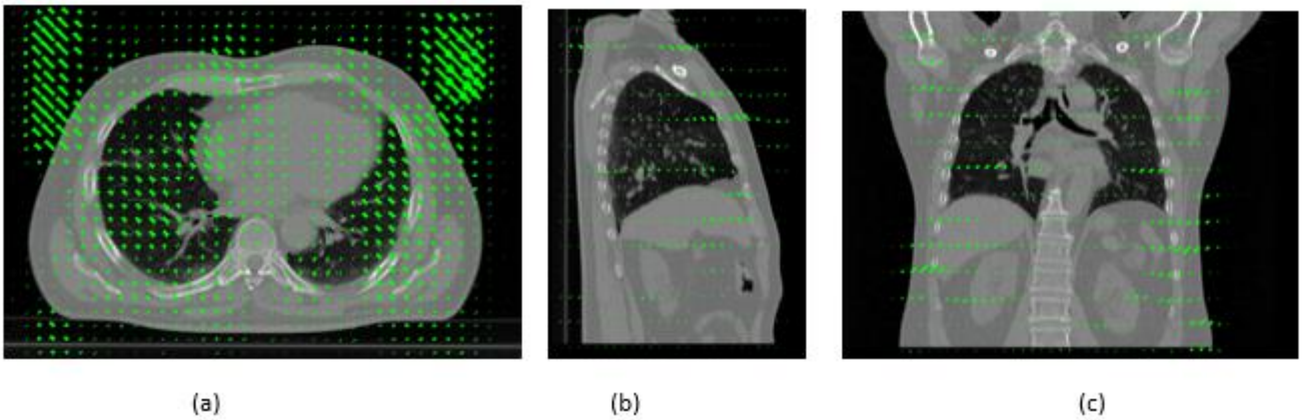

Figure 28 CT images of a lung case on which deformation field representing the system-dependent and patient-dependent geometric distortions in MRI is applied (a) axial plane view (b) sagittal plane view (c) coronal plane view

4.5 Determination of Dosimetric Impact of Geometric Distortions

In this study, the method developed for the quantification of the dosimetric effect of geometric distortions is based on the treatment plan with two CT scans, undistorted and distorted CTs and their dose distribution analysis and comparison. Margins are generated in the as introduced in detail in the Treatment Planning section; firstly, the contours for target and OARs are delineated, ITV contour is generated by the combination of GTVs belonging to 3 phases around end-exhale, and CTV is generated by 8 mm isotropic expansion of ITV. Afterwards, according to the dose prescriptions defined for CTV and OAR rings expanded from CTV, beam angles are decided for each case, and beam-specific PTVs are created for each beam according to the lateral, distal, and proximal margins calculated with the defined field-set-up. Lastly, a ring around the bsPTV is created for the sparing of the OARs. In order to create distorted CT and contours, the Deformation Vector Field quantifying the displacement map of the MRI due to geometric distortions is applied to the CT data and all of the contours.

In order to simulate the treatment, which gives the comparable dose distributions for undistorted and distorted CTs to determine the dosimetric impact of geometric distortions in MRI-only workflow, treatment is designed with the same beam angles, proton beam energies and dose prescriptions for both of the scans. The beam angles that are determined in the treatment plans designed based on CTV structure are used. After the generation of bsPTVs, the treatments are designed and optimized separately for each field based on the bsPTV as target obtaining Single Field Uniform Dose (SFUD) and the treatment isocenter is defined as the isocenter of the bsPTV. Therefore, treatment isocenter is shifted in the distorted CT treatment simulations.

Firstly, the treatment plan is optimized for each single field on the distorted CTs with distorted bsPTV defined as the target. The final dose distribution for the distorted CT, denoted as $D_{distorted}$, is the average of the dose distributions generated from each single field optimization. The created treatment plan design is applied and the dose is recalculated in undistorted CT using the same beam geometry and beam weights calculated in the optimization of distorted CT. The dose recalculation is based on single field optimization with the calculated beam weights for each single field on the distorted CT. Like in $D_{distorted}$ calculation, the final dose distribution for the undistorted CT, denoted as $D_{undistorted}$, is the average of the dose distributions generated from each single field optimization. Figure 29 shows the dose calculation workflow for undistorted and distorted scans.

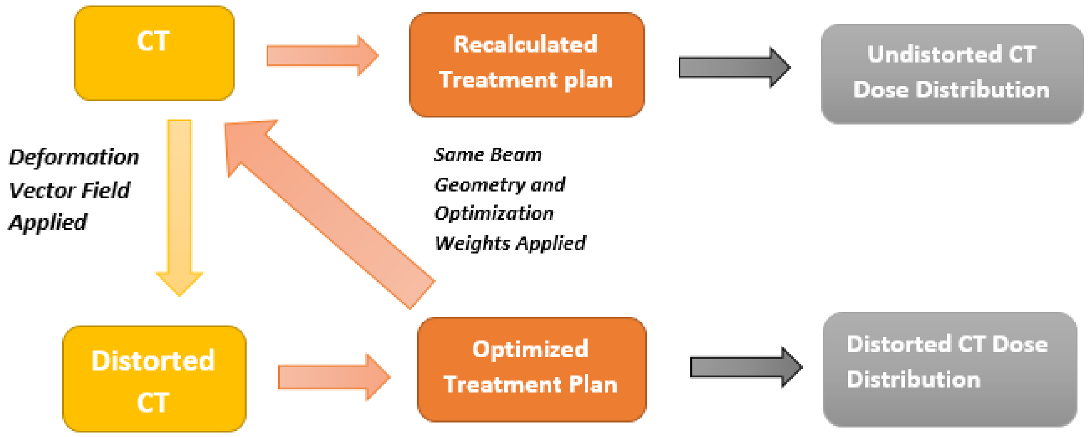

Figure 29 Flow chart showing the treatment simulation steps for the undistorted and distorted CT scans

In order to compare the final dose distributions of undistorted and distorted CTs, two workflows have been developed. These workflows have basically the same operations on the CTs in the treatment plan and dose distribution simulation, but they differ in the final steps where the dose distribution analysis is performed. Both of the workflows are tested and their results analyzed on the lung and pancreas phantom and one clinical lung case. In the end, one of them is chosen as the main workflow and all of the cases in the dataset are analyzed following that workflow.

4.5.1 Workflow 1

In the first workflow, the undistorted and distorted CT dose distributions are analyzed and compared based on their dose volume histogram (DVH), which is a histogram used as a plan evaluation tool in the radiation therapy treatment planning relating the radiation dose to tissue volume. The analysis of each scan is made on the final dose distribution on the CTV volume and OARs. For each dose distribution, the analysis is made using several different parameters extracted from DVHs, which are going to be introduced in detail in the Assessment of Dosimetric Impact of Geometric Distortions section. Figure 30 shows the flow chart of workflow 1.

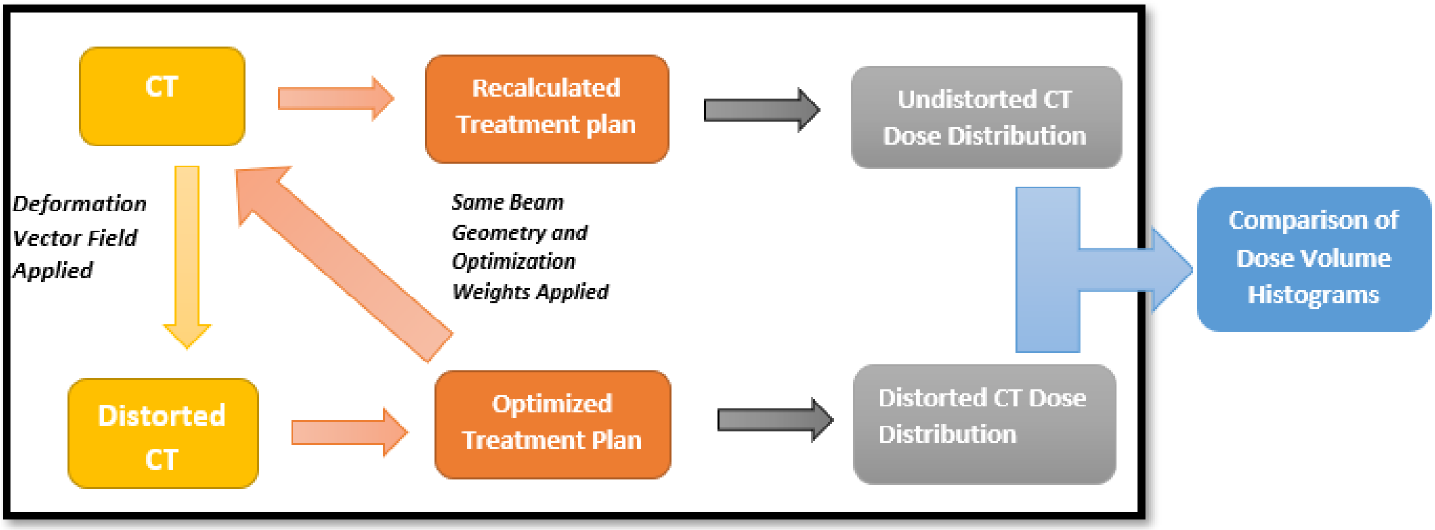

Figure 30 Flow chart of Workflow 1 in which the blocks in black frame show the operations common in both workflows and the other block shows analysis made in workflow 1

4.5.2 Workflow 2

The second workflow is based on the idea to compare the dose distributions from undistorted and distorted CTs in the same reference frame as the distorted CT is considered geometrically incorrect. In order to bring these two dose distributions into the same frame of reference, the inverse of DVF is applied to the distorted CT dose distribution. This dose distribution is denoted as $D_{distorted\_inv}$. The inverse of DVF is calculated through Plastimatch. The comparison analysis is performed between the parameters extracted from the DVH of $D_{undistorted}$ and $D_{distorted\_inv}$ on the CTV volume and OARs. In this workflow, as the dose distributions are in the same reference frame, it gives the possibility to perform analysis also on the DVH of difference dose distribution between $D_{undistorted}$ and $D_{distorted\_inv}$. Moreover, for the comparison of these two dose distributions in the same reference frame, it is also possible to perform gamma analysis, which is based on the calculation of gamma (γ) index for each point of interest using a preselected dose difference and distance to agreement criteria and determination of the pass-fail outcome for the agreement of two dose distributions based on the calculated γ index (Li et al., 2011). If workflow 2 is chosen as the main modality, these analyses are going to be performed on all of the cases in the dataset.

Figure 31 shows the flow chart of workflow 2 with the initial steps.

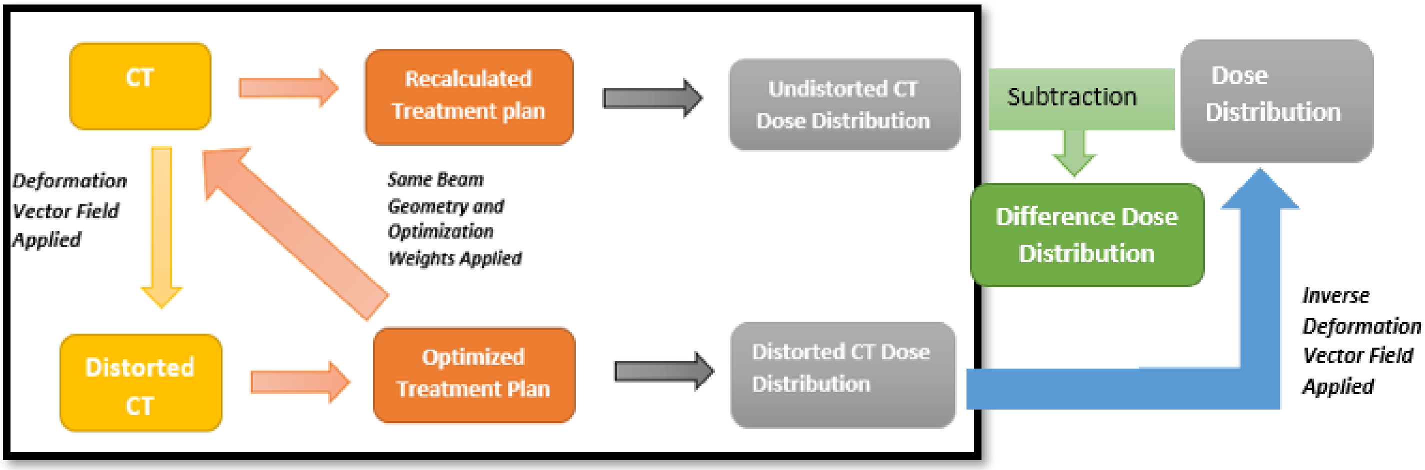

Figure 31 Flow chart of Workflow 2 in which the blocks in black frame show the operations common in both workflows and the blocks outside the frame show the operations applied for final analysis in workflow 2

4.6 Assessment of Dosimetric Impact of Geometric Distortions

The dosimetric effect of geometric distortions is evaluated based on the dose distributions of undistorted and distorted CTs. The plans are optimized on the bsPTV minimizing the dose in OAR ring separately for each field, and the dosimetric analysis is carried out on the CTV volume, and OARs in the final dose distribution, which is found by averaging of the dose distributions simulated in single field optimizations.

The evaluations of final dose distributions are made based on Dose Volume Histogram (DVH) for each case. DVH is a cumulative dose-volume frequency distribution summarizing the simulated radiation dose within the volume of interest. In DVH plots, the x-axis represents the received dose and the y-axis represents the fractional volume of the total volume of the examined structure receiving that dose (Drzymala et al., 1991). This representation reduces 3D dose distributions within a volume of interest to a 1D curve.

The comparison is made by evaluating the difference of these parameters in the two scans (i.e. distorted and undistorted CTs). The parameters used in the comparison of dose in CTV and OARs are discussed in detail in the next section.

4.6.1 Analysis on Target Structure

Regarding the dosimetric impact of geometric distortions in the target volume, the dosimetric analysis is made in the CTV volume in the unit of Gy. The comparison is performed based on 4 parameters extracted and/or derived from the DVHs of dose distributions:

i. $D_{2\%}$: It is also called near-maximum dose and it represents the dose received by the 2% of the CTV volume.

ii. $D_{98\%}$: It is also called near-minimum dose and it represents the dose received by 98 % of the CTV volume.

iii. D_{mean}: It represents the mean of the dose received by the whole CTV volume.

iv. Dose Homogeneity Index (DHI): It is a parameter indicating the dose homogeneity, which is used to analyze the uniformity of the dose distribution in the target volume. It is used to evaluate the effect of geometric distortions on the uniformity of the dose in the target volume. There are several different definitions of DHI. In this study, the following definition of DHI is used:

$$DHI = \frac{D_{5\%}}{D_{95\%}}$$

where $D_{5\%}$ is the minimum dose in the 5% of the CTV and $D_{95\%}$ is the minimum dose in 95% of the CTV. The lower the DHI index, so closer to one, the better is the dose homogeneity (Gong, Wang, Bai, Jiang & Xu, 2008).

It has been reported in ICRU Report 83 that, since maximum and minimum dose, D_{max} and D_{min}, are the dose values specified at a single calculation point, they have great delineation uncertainty (ICRU, 2010). Therefore, in the analysis of the target volume, $D_{2\%}$ and $D_{98\%}$ are used instead of D_{max} and D_{min} respectively.

4.6.2 Analysis on OAR

In the treatment plan, sparing of OAR has been designed by the formation of the OAR ring as an expansion of the bsPTV. The analysis is made for each OAR in each region. Analysis of the dose in OARs and the comparison of the dose values in OARs are made based on the two dose parameters extracted from DVH:

i. D_{mean}: It indicates the mean dose in the whole volume of the OAR structure. According to ICRU Report 83, the mean absorbed dose in parallel-like structures can be a useful measure of absorbed dose in an OAR (ICRU, 2010). According to tissue architecture, the normal tissue cells are described as parallel-like, such as liver and lung, or serial-like structures, such as spinal cord and esophagus.

ii. D_{max}: It indicates the maximum dose value delivered to the structure. Since geometric distortion can lead to deviations in the dose to the OAR and would lead to exposure of the OAR structure to a high dose, D_{max} is chosen as one of the OAR analysis parameters.

4.6.3 Statistical Analysis

In this study, after the designed TPs are simulated in each case and the mentioned dosimetric parameters belonging to each dose distribution are found, statistical analysis is performed in order to test the statistical significance of the dosimetric change in undeformed and deformed CTs arising from geometric distortions. For this purpose, Wilcoxon signed-rank test, which is a non-parametric test applied on paired observations, is performed between paired parameters belonging to the undistorted CTs and distorted CTs. The test is performed separately for each dosimetric parameter, i.e. $D_{2\%}$, $D_{98\%}$, D_{mean} and DHI for the CTV volume and D_{mean} and D_{max} for the OARs, on the undeformed-deformed pairs for clinical data, returning a ρ parameter for each dosimetric parameter. This test is mainly principled on the absolute difference of the pairs, which are dosimetric parameters from the undeformed dose distribution, D_{undef}, and that from the deformed dose distribution, $D_{def.}$ It is based on the assumption that their absolute difference has a distribution with zero median. Excluding the data, which have $\left|D_{def} - D_{undef}\right| = 0$, the test orders the pairs from smallest to largest absolute difference and ranks them in the same order, which is denoted as R_i with i indicating the pair number. The pair with the smallest absolute difference is ranked as 1. As a result, the test statistic, W, is calculated as:

$$W = \sum_{i=1}^{N_r} \left[sgn(D_{def,i} - D_{undef,i}) \times R_i \right]$$

where N_r denotes the number of pairs which have non-zero absolute difference and sgn is the sign function. As a result of the test, a ρ value is found. It is a non-negative scalar from 0 to 1 indicating the probability of observing a test statistic.

In order to determine to perform the Wilcoxon signed-rank test either on all of the clinical data grouped together or on the data separated in terms of thorax and abdominal regions and to see if the distribution of dosimetric results show variation between different regions, Kruskal-Wallis test is performed separately on different dosimetric parameters in CTV volume with 3 groups, lung, liver and pancreas. Moreover, it is also used in a second analysis conducted in order to see if the distribution of dosimetric differences between undeformed and deformed doses is statistically different in different regions. Kruskal-Wallis test is a non-parametric test used to compare the medians of the data groups to determine if they come from the same distribution. It assumes that the populations have the same continuous distributions of their samples apart from possible different locations due to group effects. Moreover, it also assumes that all the observations are mutually independent. This test is based on the ranks of the data rather than their numeric values. Data are ordered from the smallest to the largest across all groups, and their numeric ordering is taken in order to find the rank of the data. The smallest value gets a rank of 1, and the second smallest gets 2 and it increases as the value increases. As a result of the test, a ρ value is returned with the null hypothesis that the data in different populations come from the same distribution. If the ρ is greater than the set significance level, the hypothesis is rejected and the groups which have a different distribution are determined with the comparison of the ranks.

5 RESULTS & DISCUSSION

5.1 Comparison of Workflow 1 & Workflow 2

The dosimetric impact of geometric distortions has been assessed using two different workflows applied on the lung and pancreas phantoms and one clinical lung case. The difference between these two workflows is mainly the dose reference frame correction, which is additionally applied in workflow 2. As described in the previous chapter, workflow 1 is mainly based on a direct comparison of dose distributions of undeformed and deformed CTs. Different from workflow 1, in workflow 2, it has been aimed to transfer the dose distribution of deformed CT into a geometrically correct reference frame. Therefore, dose comparison is made on the DVHs of undeformed CT dose distribution and of the dose distribution obtained by the application of inverse of DVF on the deformed dose. While the second workflow aims to transfer the dose distribution of deformed CT into a geometrically correct reference frame, it also introduces uncertainties arising from the inversion of DVF. The dose distributions in both workflows are assessed based on the absolute difference of the parameters, which are mentioned in the 'Assessment of Dosimetric Impact of Geometric Distortions' section, belonging to the two dose distributions coming from undeformed and deformed CTs. Accordingly, one of the workflows is chosen as the main modality of this study to be applied to all of the data in the dataset.

Figure 32 visualizes the TP simulation and the final dose distribution as a result of the application of Workflow 2 for the lung and pancreas phantoms and one clinical lung case, respectively.

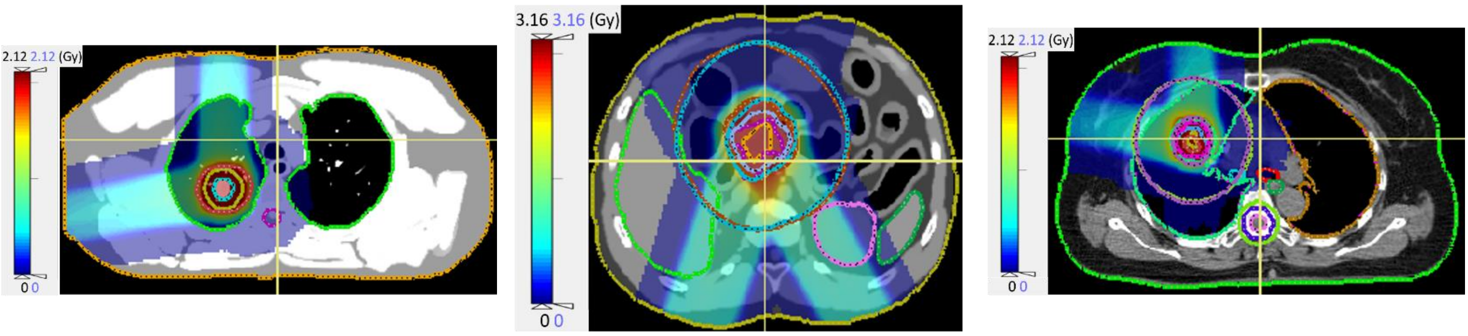

(a) (b) (c)

Figure 32 Treatment Plan simulations with Workflow 2 on (a) lung phantom, (b) pancreas phantom and (c) clinical lung case

Treatment plan analysis in the CTV volume based on the DVH parameters is presented in Table 5 below for Workflow 1 and 2. The result for each parameter is the absolute difference of that parameter value in undeformed and deformed CT distributions. The absolute difference results for $D_{2\%}$, $D_{98\%}$, and D_{mean} are normalized to the prescribed dose in order to be able to make a comparison among the results in different regions.

Table 5 Assessment of dosimetric change measured on DVH parameters in CTV volume following Workflow 1 and Workflow 2 in the lung and pancreas phantoms and in the clinical lung case ($D_{2\%}$, $D_{98\%}$, D_{mean} parameters are normalized to the prescribed dose and given in percentage whereas DHI is given as absolute difference)

		WORKFLOW 1	**WORKFLOW 2**
Lung Phantom	**$D_{2\%}$ (%)**	0.400	0.900
	$D_{98\%}$ (%)	0.400	0.700
	D_{MEAN} (%)	0.250	0.050
	Dose Homogeneity Index (DHI)	0.007	0.013
Pancreas Phantom	**$D_{2\%}$ (%)**	0.133	0.467
	$D_{98\%}$ (%)	0.067	0.200
	D_{MEAN} (%)	0.067	0.033
	Dose Homogeneity Index (DHI)	0.001	0.007
Clinical Lung Case	**$D_{2\%}$ (%)**	0.80	1.30
	$D_{98\%}$ (%)	15.90	16.0
	D_{MEAN} (%)	3.40	3.250
	Dose Homogeneity Index (DHI)	0.102	0.106

Table 6 represents the results for dosimetric changes between the undeformed and deformed scans as a result of the geometric distortions in the Organs at Risk in each region following Workflow 1 and 2 and the results are expressed as absolute difference dose normalized to the prescribed dose in percentage. The values different than 0 are represented in bold.

Table 6 Normalized differences in mean and maximum dose in the percentage of target prescribed dose in OARs in the lung and pancreas phantoms and in the clinical lung case following Workflow 1 and Workflow 2

			WORKFLOW 1	**WORKFLOW 2**
Lung Phantom *(In % of 2 Gy)*	**Spinal Cord**	**DMEAN**	0.0	0.0
		DMAX	0.0	0.0
	Heart	**DMEAN**	0.0	0.0
		DMAX	0.0	0.0
	Total Lung	**DMEAN**	**0.100**	**2.0**
		DMAX	0.0	**2.50**
Pancreas Phantom *(In % of 3 Gy)*	**Liver**	**DMEAN**	**0.033**	**0.100**
		DMAX	**1.667**	**6.667**
	Left Kidney	**DMEAN**	**0.067**	**0.033**
		DMAX	0	0
	Right Kidney	**DMEAN**	**0.033**	**0.033**
		DMAX	0.0	0.0
Clinical Lung Case *(In % of 2 Gy)*	**Spinal Cord**	**DMEAN**	0.0	0.0
		DMAX	0.0	0.0
	Heart	**DMEAN**	0.0	0.0
		DMAX	0.0	0.0
	Eusophagus	**DMEAN**	0.0	0.0
		DMAX	0.0	0.0
	Left Kidney	**DMEAN**	0.0	0.0
		DMAX	0.0	0.0
	Right Kidney	**DMEAN**	**0.40**	**0.250**
		DMAX	**2.50**	**2.50**

Looking at the dosimetric parameter differences in the CTV volume and the OAR volumes in workflow 1 and 2, it has been observed that the results are not the same for the two workflows. Regarding the CTV volume, the differences in the parameters $D_{2\%}$, $D_{98\%}$, and Dose Homogeneity Index are higher and D_{mean} is slightly lower in workflow 2 compared to workflow 1. The dose distribution is aimed to be transferred into a geometrically correct reference frame in workflow 2. The geometrical dose reference frame correction compensates for the dosimetric impact of geometric distortions in the mean dose. However, considering more differences in the other CTV dose parameters, these results confirm that the operation of inversion of DVF in workflow 2 could potentially introduce extra uncertainties, leading to more deviation of near-maximum and near-minimum doses and altering the dose distribution homogeneity in the deformed scans more. Also, the results in OARs are slightly higher in Workflow 2 for both D_{mean} and D_{max}. As such, workflow 1 is chosen as the main modality and used for the analysis of the rest of the data in the dataset. In the following sections, the results obtained by following workflow 1 are presented.

5.2 Results of Dosimetric Analysis on Phantoms

Results in Target Structure

The treatment plan simulations for the assessment of the dosimetric impact of geometric distortions are first performed on the thoracoabdominal phantoms since phantoms provide a dynamic 3D model of the human body and stand as an accurate measurement and validation tools (Paganelli et al., 2017). The phantoms are used to interpret and also validate the analysis made on the clinical dataset. Therefore, the treatment simulations and the analysis of dosimetric changes due to geometric distortions are performed in the phantoms in the same regions which are tested with clinical data.

The treatment plan simulations are performed on the manually contoured two lung phantoms, with the tumors at different locations, liver phantom and pancreas phantom. All the treatment planning design parameters, dose distribution and the resulting DVH plots for each phantom are reported in Appendix A. The simulated treatment plans with the resulting dose distributions in these phantoms are shown in Figure 33. As mentioned before and visualized with the dose distributions in this figure, the two lung phantoms differ in terms of the location of the tumors and the location of the final dose distribution where it has the prescribed dose, i.e. close to the soft tissue or isolated inside the lung parenchyma.

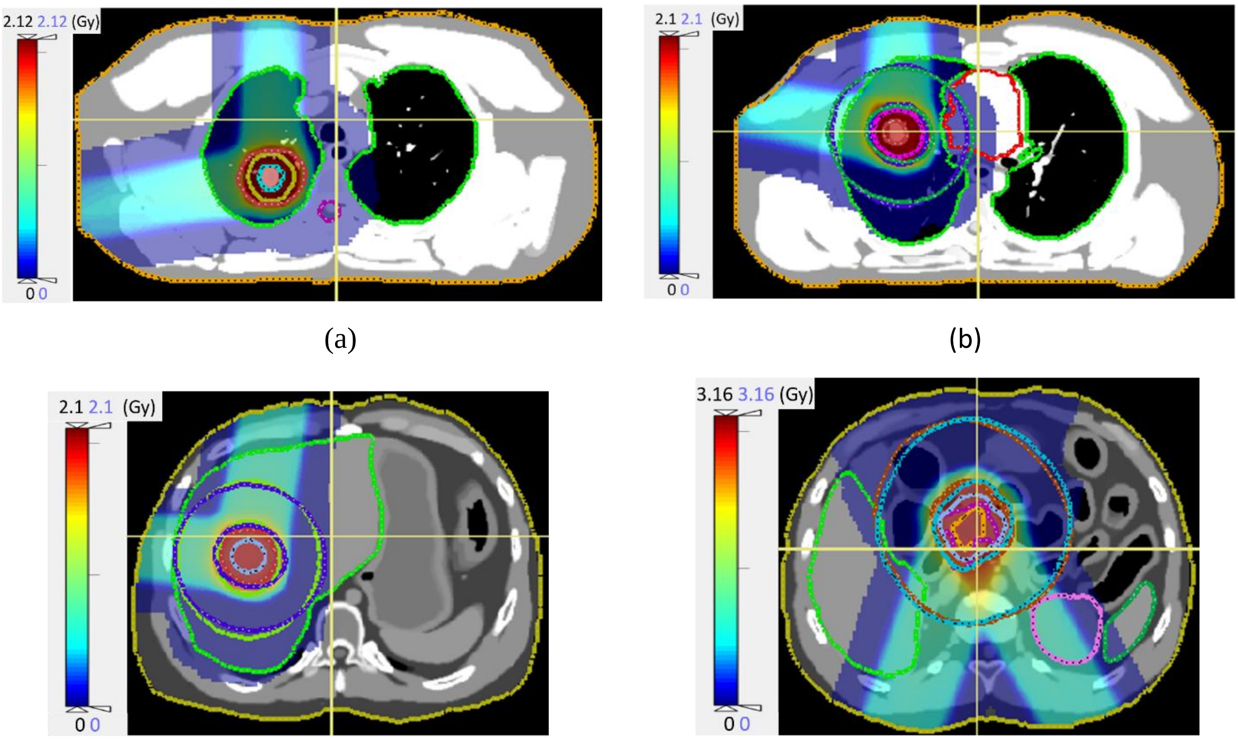

(a) (b)

(c) (d)

Figure 33 Dose distributions and field set-up representations for (a) Lung phantom with a tumor close to the soft tissue (b) Lung phantom with a tumor isolated in lung parenchyma (c) liver phantom and (d)pancreas phantom

Table 7 shows the absolute differences of the dosimetric parameters in the CTV volume between the undeformed and deformed dose distributions. The absolute difference results for $D_{2\%}$, $D_{98\%}$ and D_{mean} are normalized to the prescribed dose.

Table 7 Differences of Dosimetric Parameters in CTV region between undeformed and deformed dose distributions belonging to the phantom data ($D_{2\%}$, $D_{98\%}$, D_{mean} parameters are normalized with respect to the prescribed dose)

	$D_{2\%}$ (%)	$D_{98\%}$ (%)	D_{mean} (%)	Dose Homogeneity Index (DHI)
Lung Phantom (Tumor close to soft tissue)	**0.400**	**0.400**	**0.250**	**0.007**
Lung Phantom (Tumor isolated in lung parenchyma)	**0.70**	**8.70**	**1.30**	**0.048**
Liver Phantom	**0.100**	**0.100**	**0.050**	**0.001**
Pancreas Phantom	**0.133**	**0.067**	**0.100**	**0.001**
Mean Difference	**0.333%**	**2.312%**	**0.425%**	**0.014**

Considering both the thorax and abdominal region results, for all of the parameters, the differences between the undeformed and deformed dose distributions are the smallest in the abdomen regions. The absolute difference results are very close to each other and small with respect to the prescribed dose in the abdomen region for the liver and pancreas phantoms reaching at most 0.133%. The dosimetric differences are higher in the lung region. Indeed, while for the lung phantom with a tumor close to the soft tissue, the results reach up to 0.40%, for the lung phantom with an isolated tumor inside the lung parenchyma, the results show a relatively higher difference ranging between 0.70% and 8.70% of the prescribed dose. This difference is visualized better in Dose Volume Histograms (DVHs) of lung, liver and pancreas regions, in Figure 34, with the DVH of the undeformed phantom, in red line overlaid on the DVH of the deformed phantom, in blue line.

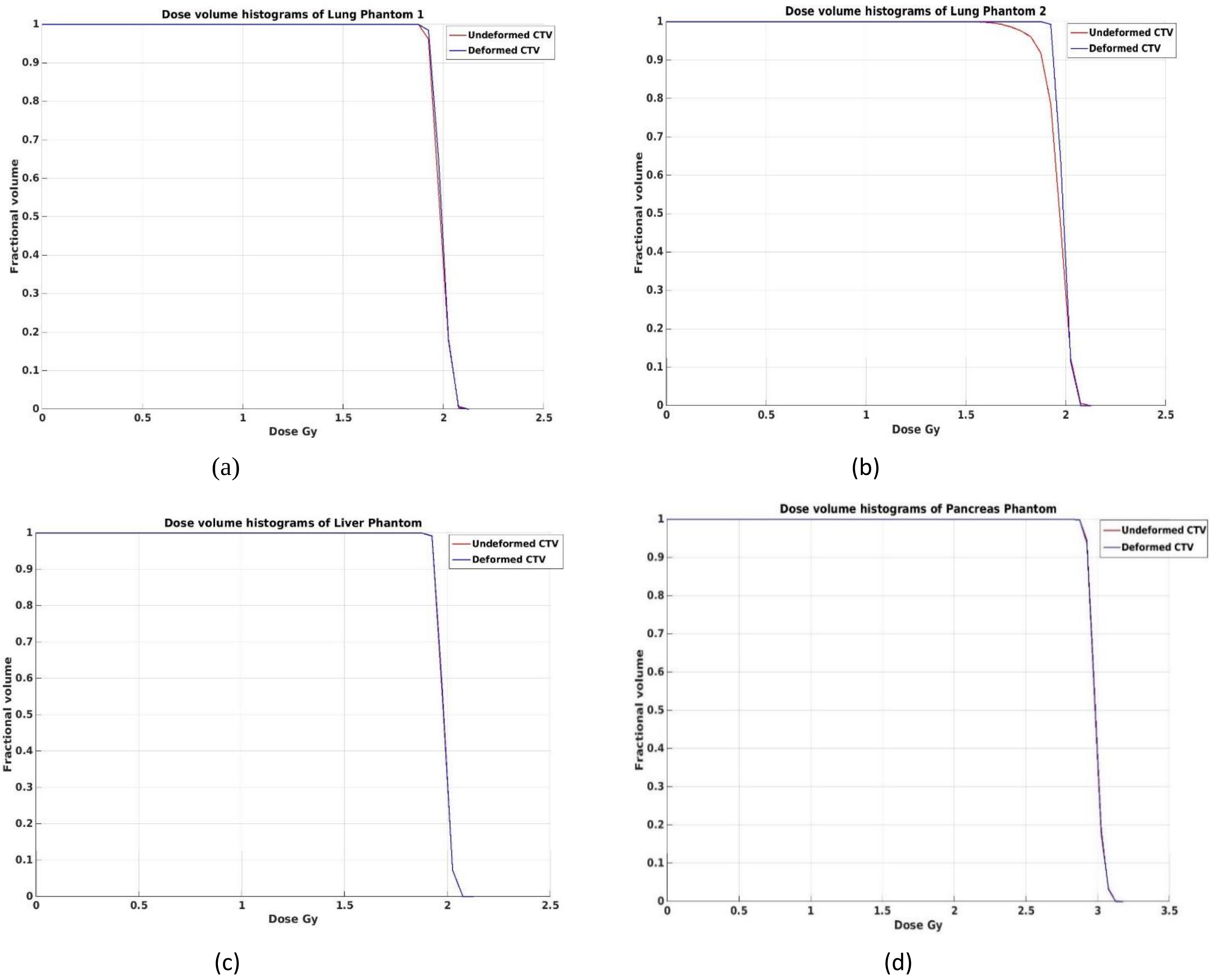

(a)

(b)

(c)

(d)

Figure 34 Dose Volume Histograms with Dose on the x-axis and fractional volume on the y-axis of (a) Lung phantom with a tumor close to soft tissue (b)Lung phantom with an isolated tumor in lung parenchyma, (c)liver phantom and (d)pancreas phantom. Red line represents the DVH of undeformed phantom whereas blue line represents the DVH of deformed phantom

In the liver and pancreas regions, DVHs of undeformed and deformed phantoms show a very similar trend that they are almost overlaid with very small differences. However, unlike abdominal regions, in the DVH plots of lung phantoms, differences are more observable especially in the region where the curve bends, which corresponds to the near-minimum dose, $D_{98\%}$. This difference is observably much higher in the lung phantom that has an isolated tumor in the lung parenchyma. In this lung phantom, also the mean dose is apparently different in DVHs of undeformed and deformed distributions verifying the results in Table 7. The higher results in this phantom rely on the fact that there is a higher tissue density gradient around the tumor due to the presence of ribs and air around it. This causes higher dosimetric changes in this region due to the shift of the Bragg peak (Paganelli et al., 2017).

Considering both dose difference results in Table 7 and the DVH plots, geometric distortions appear with the highest influence on $D_{98\%}$ and D_{mean} parameters. This is visualized better with the box plot in Figure 35, which reports the results of all of the phantoms for each dosimetric parameter separately. Since the prescribed doses are different in lung, liver and pancreas cases, which are 2 Gy, 2 Gy and 3 Gy respectively, the box plot is plotted based on the normalized absolute dose differences in percentage for $D_{2\%}$, $D_{98\%}$ and D_{mean} parameters and DHI is plotted with absolute difference values with its y-axis on the right.

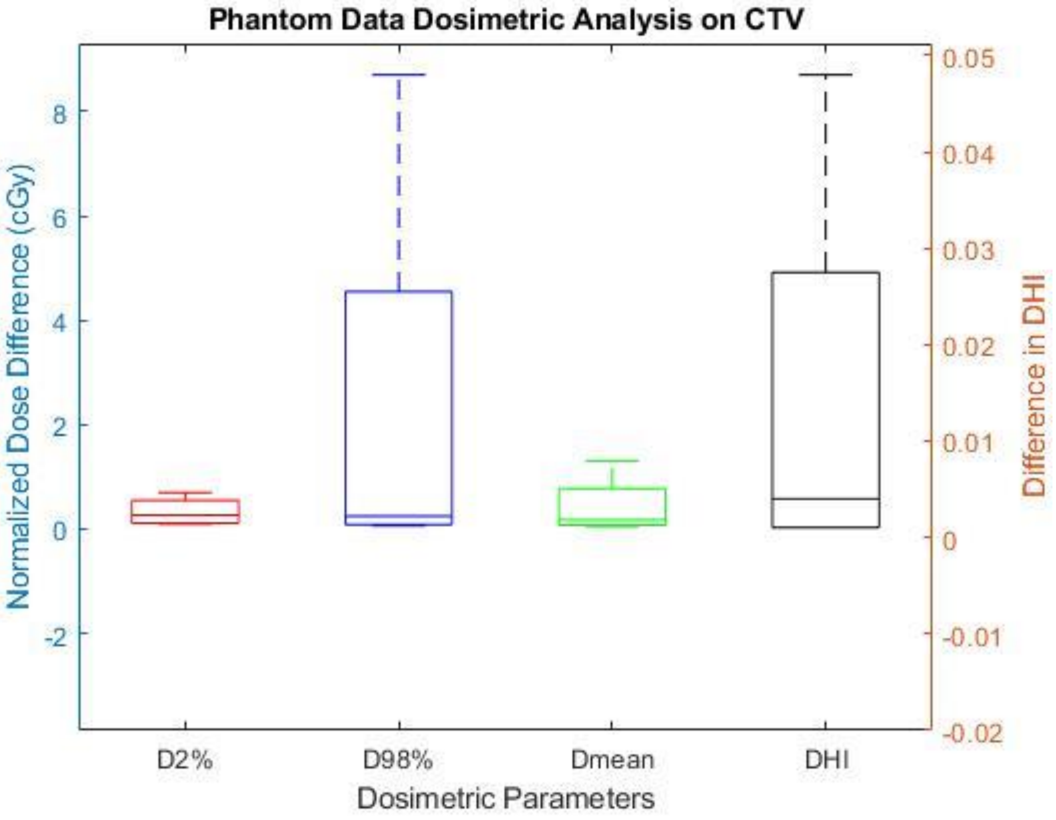

Figure 35 Box plot for the phantom dataset in which dose differences between undeformed and deformed target dose for $D_{2\%}$, $D_{98\%}$ and D_{mean} parameters, normalized with respect to the prescribed dose, are shown in red, blue and green respectively with their y-axis on the left and DHI difference is shown in black with its y-axis on the right

As it is shown in the box plot in Figure 35, $D_{98\%}$ has the highest median and mean absolute difference and is subject to the highest change among all of the phantoms with the greatest range in the phantom dataset. Indeed, while the absolute difference range varies between 0.067% and 8.70% of the prescribed dose in the $D_{98\%}$, dose parameter, it stays below 0.70% and 1.30% of the prescribed dose in the $D_{2\%}$ and D_{mean} parameters.

Results in Organs at Risk

The dosimetric effect of geometric distortions is assessed on the manually contoured organs at risk in each region with the D_{mean} and D_{max} dosimetric parameters.

Spinal cord, heart, and ipsilateral and contralateral lungs together, referred as total lungs, are evaluated in lung phantoms. In the liver phantom, the total liver volume itself, right kidney and right lung have been of concern whereas liver and kidneys are evaluated in the pancreas phantom.

Table 8, Table 9 and Table 10 report the results for OARs for lung phantoms, liver phantom, and pancreas phantom respectively with the values different than 0 indicated in bold.

Table 8 Normalized differences in mean and maximum dose in the percentage of target prescribed dose, 2 Gy, in organs at risk in the lung phantom

	Spinal Cord		**Heart**		**Total Lung**	
	Mean (%)	***Max (%)***	***Mean (%)***	***Max (%)***	***Mean (%)***	***Max (%)***
Lung Phantom (Tumor close to soft tissue)	0.0	0.0	0.0	0.0	**0.100**	0.0
Lung Phantom (Tumor isolated in lung parenchyma)	0.0	0.0	0.0	0.0	**0.300**	0.0

Table 9 Normalized differences in mean and maximum dose in the percentage of target prescribed dose, 2 Gy, in organs at risk in the liver phantom

	Liver		**Right Kidney**		**Right Lung**	
	Mean (%)	***Max (%)***	***Mean (%)***	***Max (%)***	***Mean (%)***	***Max (%)***
Liver Phantom	**0.050**	0.0	0.0	0.0	0.0	0.0

Table 10 Normalized differences in mean and maximum dose in the percentage of target prescribed dose, 3 Gy, in organs at risk in the pancreas phantom

	Liver		**Left Kidney**		**Right Kidney**	
	Mean (%)	***Max (%)***	***Mean (%)***	***Max (%)***	***Mean (%)***	***Max (%)***
Pancreas Phantom	**0.033**	**1.667**	**0.067**	0.0	**0.033**	0.0

D_{mean} and D_{max} dosimetric parameters show very small differences between the undeformed and deformed scans in the organs at risk being less than 0.30% of the prescribed dose, with the exception of maximum liver dose in the pancreas phantom, which reaches to 1.667% of the prescribed dose. However, these results being all below the constraints in the OARs indicate that the plans are optimized by satisfying the constraints. The difference is observed generally in the organ on which the tumor is located. Moreover, it has been observed that for the pancreas phantom, slightly higher differences are present in the kidneys and liver: in the pancreas treatment designs two oblique fields are used, so the dosimetric differences in the

OARs are seen mainly in the organs on the beam pathway, which are liver and kidneys in this case.

To sum up, in the phantoms, the geometric distortions lead to dosimetric differences in $D_{2\%}$, $D_{98\%}$, D_{mean} and DHI parameters with the highest influence observed on the $D_{98\%}$ dose with the greatest range and highest mean. Among all the regions where TP is simulated in the phantoms, it has been observed that the differences in the dosimetric parameters are higher in the lung phantoms. Indeed, when the tumor is isolated in the lung parenchyma far away from the soft tissue, the difference gets the highest since the beam encounters variations in the tissue density on its path. This hypothesis is going to be tested on the clinical dataset comprising abdominal and lung cases with the tumors at varying locations with respect to the soft tissue. With regards to the OARs, the geometric distortions do not lead to significant dosimetric changes in these organs, and the dosimetric differences range between 0.033% and 1.67% of the dose prescribed to the target volume.

5.3 Results of Dosimetric Analysis on Thorax Clinical Data

The dosimetric impact of geometric distortions in MRI-only workflow in the thorax region is tested on 10 clinical lung cancer cases. Tumors are at varying locations in the lungs and the treatment field set-up is designed for each case with the beams that have the shortest distance shoot on the tumor avoiding the nearby OARs. All the treatment plan design parameters, dose distributions and DVH results for the lung cases are reported in Appendix B.

Results in Target Structure

Table 11 shows the differences of the dosimetric parameters between the undeformed and deformed dose distributions in the CTV structure. Differences in $D_{2\%}$, $D_{98\%}$, and D_{mean} parameters are normalized to the prescribed dose in the lung treatment plans, which is 2 Gy. DHI is not normalized since it has the same scale in all of the regions. The values different than 0 are indicated in bold.

Table 11 Differences of dosimetric parameters in CTV region between undeformed and deformed dose distributions belonging to clinical lung cases ($D_{2\%}$, $D_{98\%}$, D_{mean} parameters are normalized with respect to the prescribed dose,2 Gy, and given in percentage)

	$D_{2\%}$ (%)	**$D_{98\%}$ (%)**	**D_{mean} (%)**	**Dose Homogeneity Index (DHI)**
Lung Patient 1	**0.800**	**15.900**	**3.400**	**0.102**
Lung Patient 2	**0.400**	**5.600**	**0.850**	**0.027**
Lung Patient 3	**0.400**	**21.500**	**3.250**	**0.132**
Lung Patient 4	**0.800**	**4.0**	**0.700**	**0.026**
Lung Patient 5	0.0	**1.700**	**0.400**	**0.012**
Lung Patient 6	**0.300**	**17.600**	**3.750**	**0.129**
Lung Patient 7	**0.200**	**1.400**	**0.200**	**0.009**
Lung Patient 8	0.0	**0.400**	**0.050**	**0.004**
Lung Patient 9	0.0	**0.600**	**0.250**	**0.003**
Lung Patient 10	0.0	**0.600**	**0.100**	**0.005**
Mean Difference	**0.290 %**	**6.930 %**	**1.295 %**	**0.045**

In the lung cases, the geometric distortions have the highest influence on the $D_{98\%}$ dosimetric parameter with a mean value of 6.930% of the prescribed dose over all patients, whereas it has the smallest influence on the $D_{2\%}$ with a mean value of 0.290%. These results agree with the results obtained on the phantoms. However, the clinical lung data show higher dosimetric changes, since tissue inhomogeneities are present in the clinical cases while not completely accounted for in the phantom simulations (Paganelli et al. 2017).

The results show high variations among different patients. The target dosimetric results belonging to the lung dataset are visualized in Figure 36 with the box plot on which the medians of the differences are also shown.

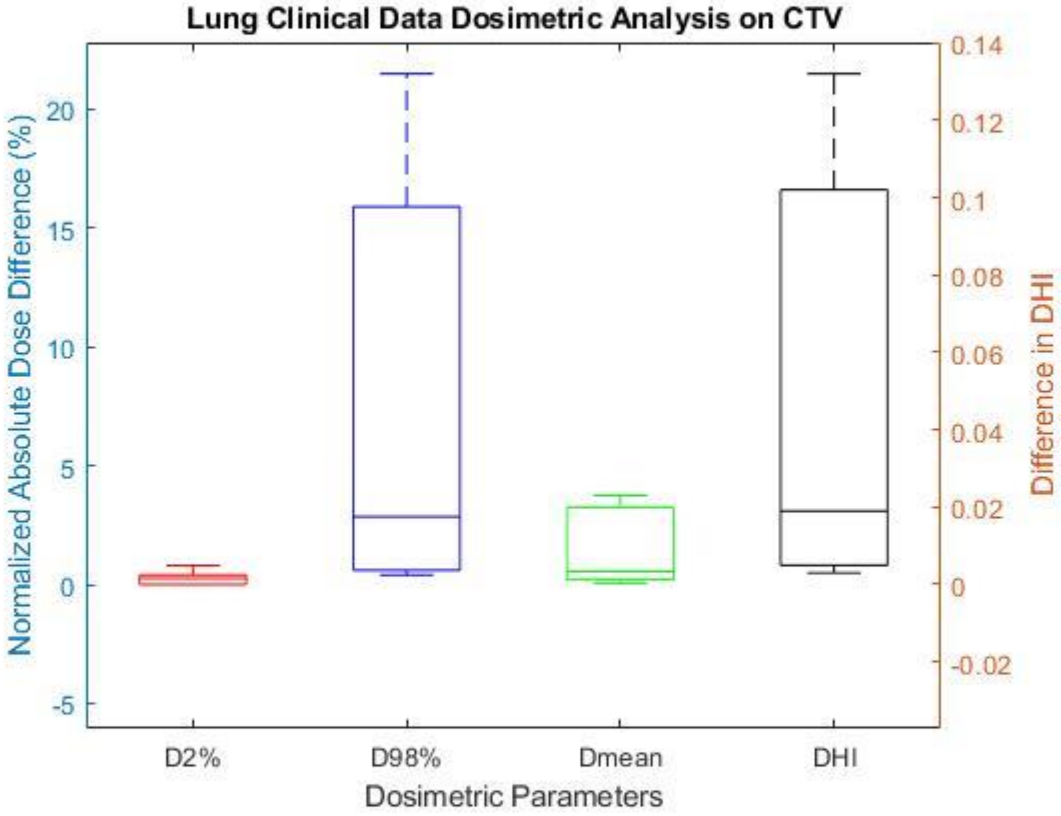

Figure 36 Box plot for lung clinical data in which dose differences between undeformed and deformed target dose for $D_{2\%}$, $D_{98\%}$ and D_{mean} parameters, normalized with respect to the prescribed dose, are shown in red, blue and green respectively with their y-axis on the left and DHI difference is shown in black with its y-axis on the right

The box plot visualizes that the ranges of dosimetric results are different in the target dosimetric parameters in the lung cases. Specifically, the ranges for the different dosimetric parameters are:

i. $D_{2\%}$ absolute difference ranges from 0.0 % to 0.8 % of the prescribed dose
ii. $D_{98\%}$ absolute difference ranges from 0.4 % to 21.5 % of the prescribed dose
iii. D_{mean} absolute difference ranges from 0.050 % to 3.750 % of the prescribed dose
iv. DHI absolute difference ranges from 0.003 to 0.132

$D_{98\%}$ has been concluded to have the highest mean. Moreover, the range of $D_{98\%}$ dose goes up to 21.1%, while the range of $D_{2\%}$ stays below 1%. These results indicate that $D_{98\%}$ is subject to the highest variation among different cases. Higher differences were observed for Patients 1,3 and 6, which are reported in Figure 37, Figure 38 and Figure 39, respectively with their dose distributions and DVH plots. The difference in these three patients with respect to the other lung cases is observed to be the position of the tumor in the lung.

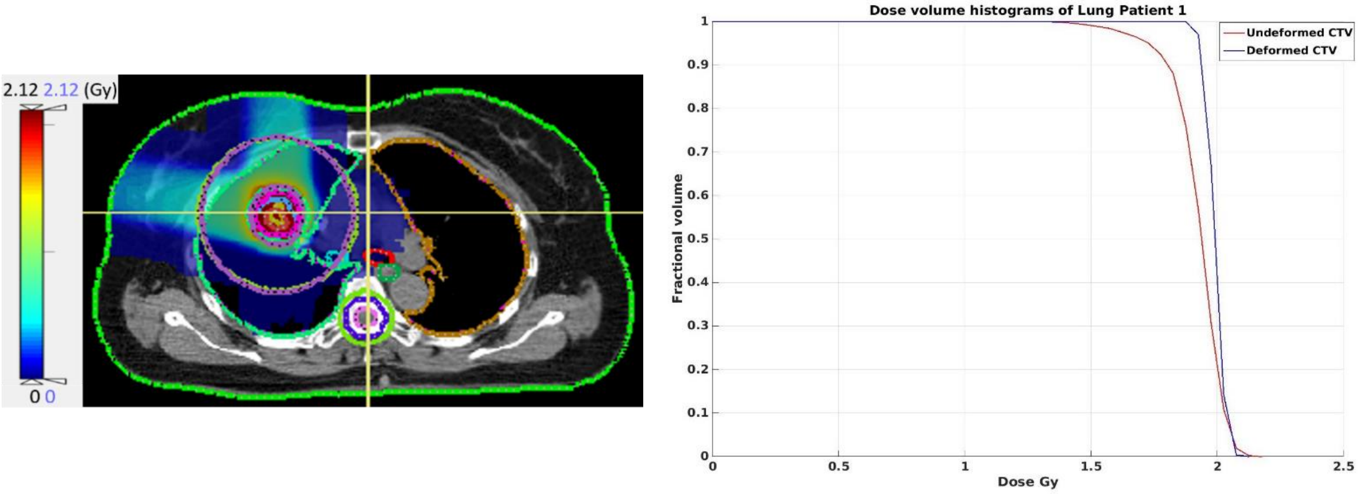

(a) (b)

Figure 37 Results for Lung Patient 1 with (a) Dose distribution for the deformed scan (b) DVH plot of undeformed, in red, and deformed scans, in blue with the x-axis representing the dose and y-axis representing the fractional volume

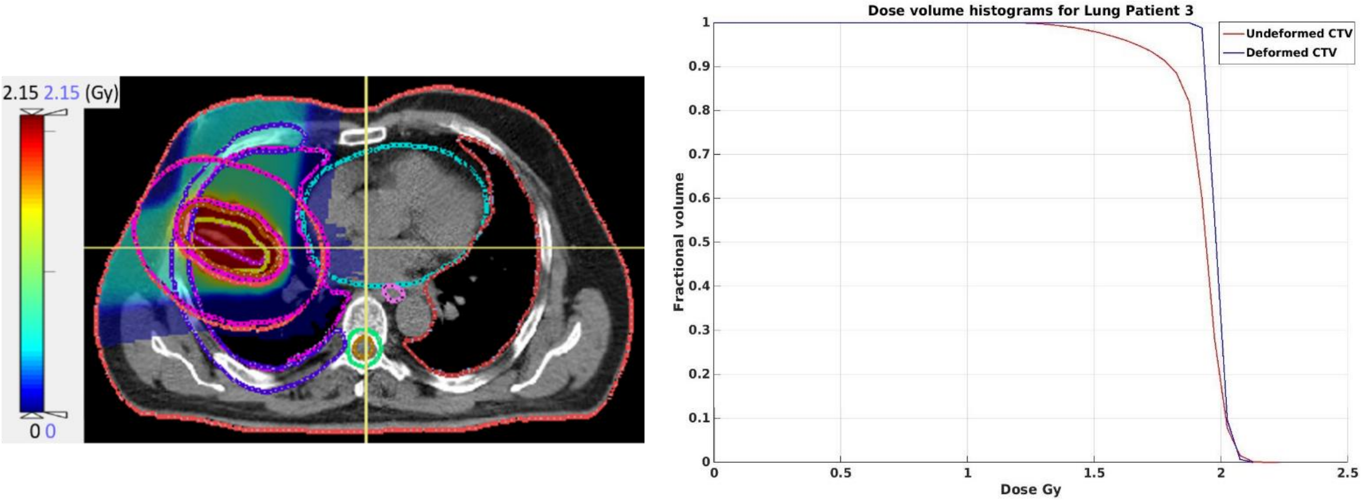

(a) (b)

Figure 38 Results for Lung Patient 3 with (a) Dose distribution for the deformed scan (b) DVH plot of undeformed, in red, and deformed scans, in blue with the x-axis representing the dose and y-axis representing the fractional volume

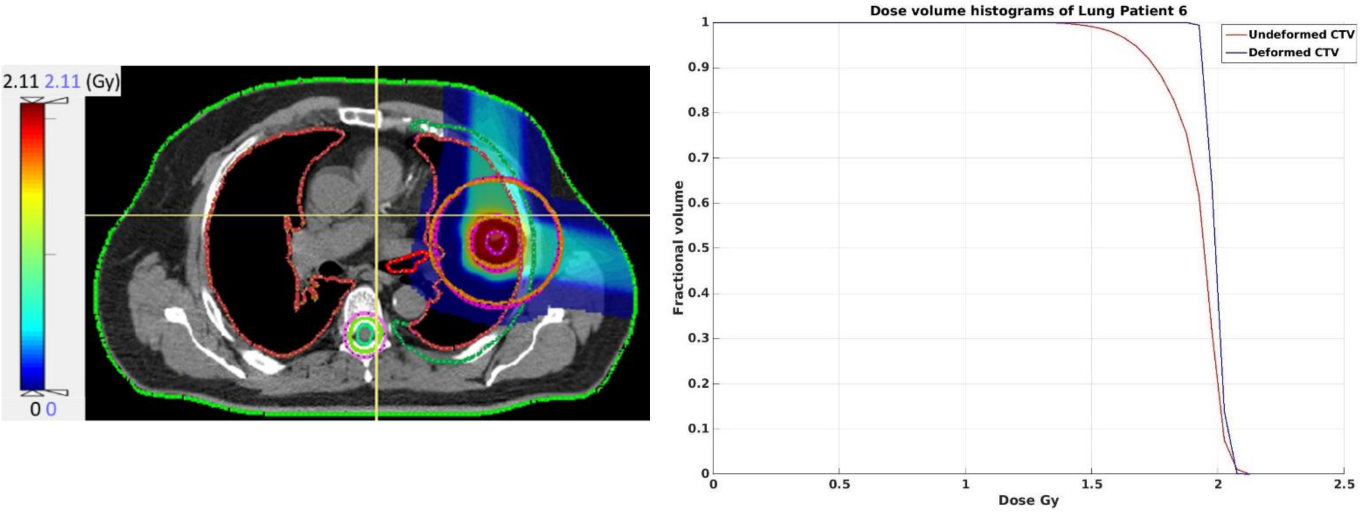

(a) (b)

Figure 39 Results for Lung Patient 6 with (a) Dose distribution for the deformed scan (b) DVH plot of undeformed, in red, and deformed scans, in blue with the x-axis representing the dose and y-axis representing the fractional volume

In these patients, it is observed that the DVH plots of undeformed and deformed scans show observable discrepancies especially in the region where the curve bends. The $D_{98\%}$ absolute dose difference in these three patients varies between 15.90% to 21.50% of the prescribed dose while it varies between 0.40% to 5.60% of the prescribed dose in the rest of the lung patients. The D_{mean} and DHI parameters show consistency with the $D_{98\%}$ dose such that they also have relatively higher values in these three patients.

As mentioned previously, these patients present an isolated tumor from the soft tissue in the lung parenchyma. In proton therapy, inhomogeneities in the density of the tissues along the beam path would potentially lead to miss of the target (Engelsman & Kooy, 2005) by the degradation of the Bragg peak (Szymanowski, Pflugfelder, Nill, & Oele, 2005), as the range calculation based on the water equivalent depth does not incorporate the position of inhomogeneities into the Bragg peak depth (Paganetti, 2012). Reflecting on this fact, since the tumor isolated in the lung parenchyma is subject to high density variations due to the presence of ribs and air around it, it has less correspondence of the Bragg peak to the tumor depth leading to higher dosimetric differences in these patients with respect to the other lung cases.

For other patients, as patients 7, 8 and 10, small absolute dosimetric differences were instead reported. It is observed that the tumors in these patients are very close to the soft tissue. Figure 40, Figure 41 and Figure 42 show the final dose distributions and their DVHs belonging to patients 7, 8 and 10 respectively.

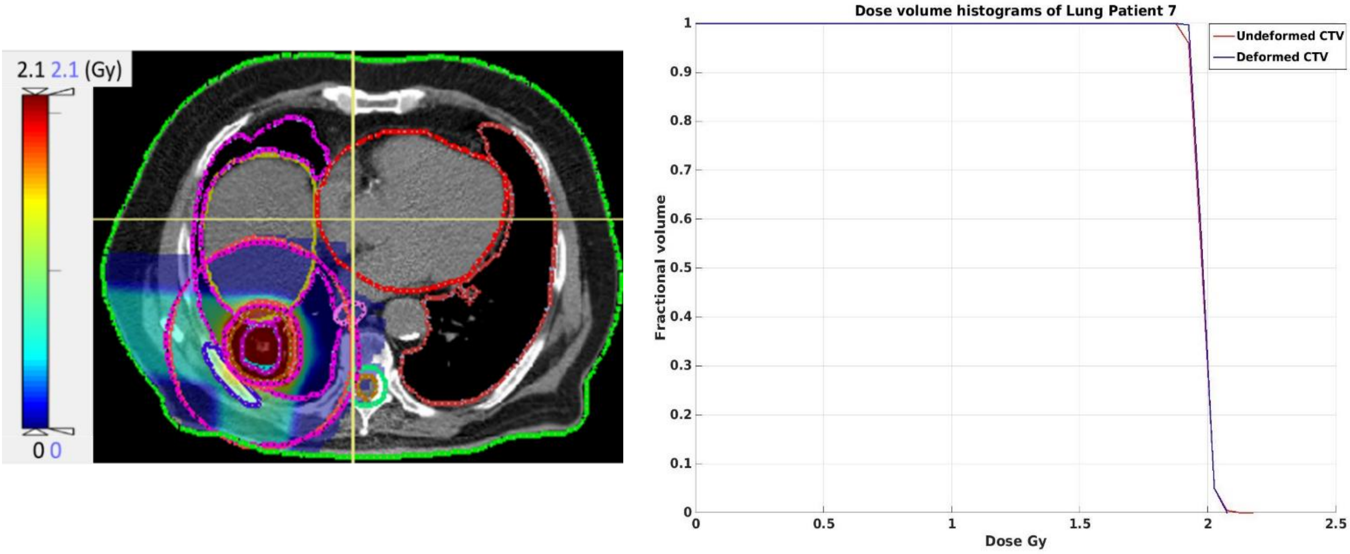

(a) (b)

Figure 40 Results for Lung Patient 7 with (a) Dose distribution for the deformed scan (b) DVH plot of undeformed, in red, and deformed scans, in blue with the x-axis representing the dose and y-axis representing the fractional volume

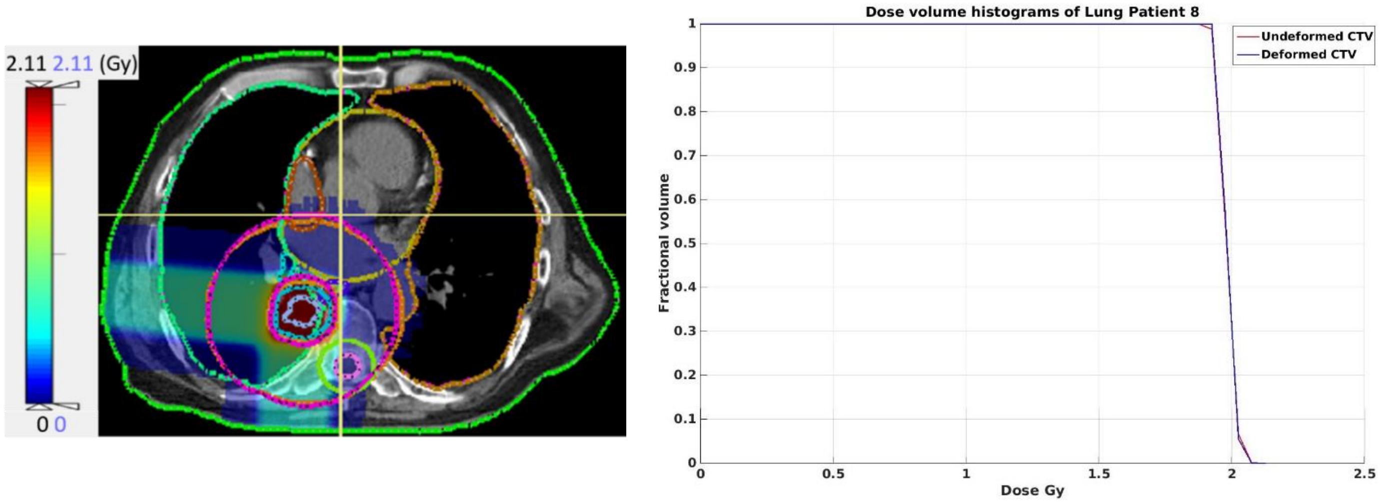

(a) (b)

Figure 41 Results for Lung Patient 8 with (a) Dose distribution for the deformed scan (b) DVH plot of undeformed, in red, and deformed scans, in blue with the x-axis representing the dose and y-axis representing the fractional volume

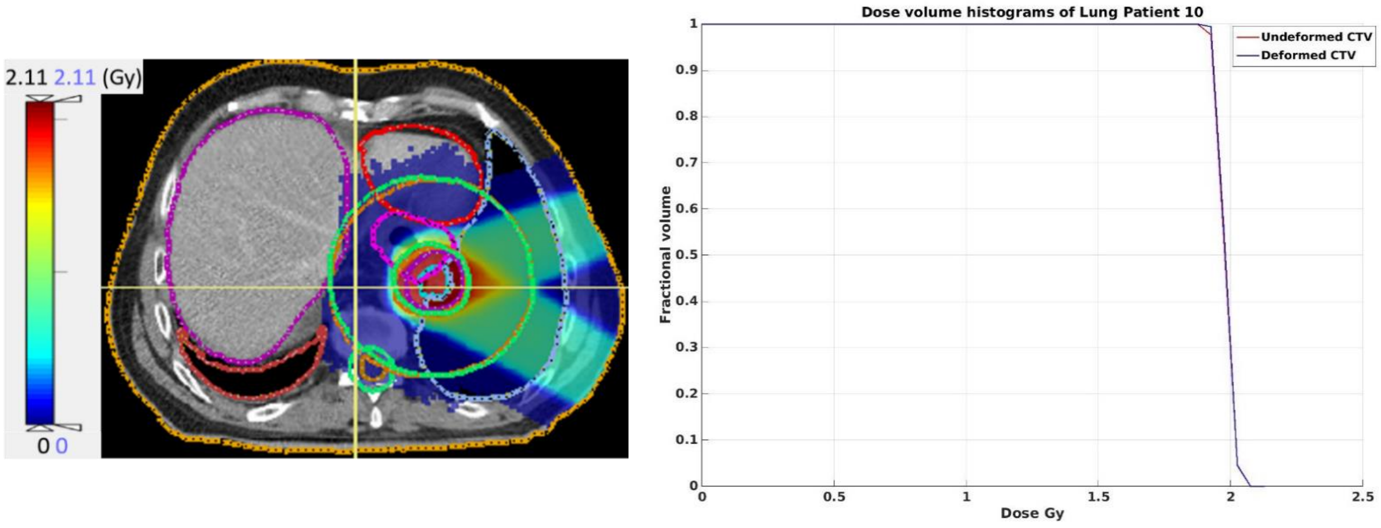

(a) (b)

Figure 42 Results for Lung Patient 10 with (a) Dose distribution for the deformed scan (b) DVH plot of undeformed, in red, and deformed scans, in blue with the x-axis representing the dose and y-axis representing the fractional volume

In these patients, the DVH curve plots of undeformed and deformed scans being in very close distance result in the absolute differences of dosimetric parameters $D_{2\%}$, D_{mean} to be small, going up to 0.80% and 0.850% of the prescribed dose, respectively. The DVH plots of the undeformed and deformed scans are very close to each other with slight differences observed only in the region where the curve bends. This confirms the fact that the geometric distortions have the highest influence on $D_{98\%}$ for which the dosimetric difference goes up to 5.60% of the prescribed dose. However, the differences in the $D_{98\%}$ dose in these patients being much smaller than that in patients 1, 3 and 6 reveals that the geometric distortions have a smaller dosimetric impact on the tumors nearby the soft tissue. This is mainly due to the fact that when the tumor in the lung is closer to the soft tissue, the density variations along the beam path are smaller.

Results in Organs at Risk

The dosimetric effect of geometric distortions is assessed on the organs at risk for each case in terms of mean dose, D_{mean}, and maximum dose, D_{max}. Spinal cord, heart, esophagus, contrary lung, and ipsilateral lung are the organs evaluated in common for all of the 10 cases. In some of the cases, due to the location and close distance of the tumor to another OAR, in addition to the common OARs, the dose at these nearby organs is also determined. In patients 7 and 10, since the tumors are on the lower side of the lung and very close to the abdomen, liver and stomach are also evaluated. Moreover, in patient 9, the tumor is very close to heart and aorta, thus, the dose at aorta is evaluated additionally in this case. The absolute difference results for OAR in lung patients are given in Table 12 with the values different than 0 indicated in bold.

Table 12 Normalized differences in mean and maximum dose in the percentage of target prescribed dose, 2 Gy, in organs at risk in the clinical lung data

	Spinal Cord		**Heart**		**Esophagus**		**Contrary Lung**		**Ipsilateral Lung**		**Additional OAR Close to Target**	
	Mean (%)	***Max (%)***	***Mean (%)***	***Max (%)***	***Mean (%)***	***Max (%)***	***Mean (%)***	***Max (%)***	***Mean (%)***	***Max (%)***	***Mean (%)***	***Max (%)***
Lung Patient 1	0.0	0.0	0.0	0.0	0.0	0.0	0.0	0.0	**0.400**	**2.500**		
Lung Patient 2	**0.050**	**25.0**	0.0	0.0	0.0	0.0	0.0	0.0	**0.300**	0.0		
Lung Patient 3	0.0	0.0	0.0	0.0	0.0	0.0	0.0	0.0	**0.800**	**5.0**		
Lung Patient 4	0.0	0.0	0.0	**7.500**	0.0	0.0	0.0	0.0	**0.050**	**2.500**		
Lung Patient 5	0.0	0.0	**0.050**	0.0	0.0	0.0	0.0	0.0	**0.100**	0.0		
Lung Patient 6	0.0	0.0	0.0	0.0	0.0	0.0	0.0	0.0	**1.050**	0.0		
Lung Patient 7	0.0	0.0	0.0	0.0	0.0	0.0	0.0	0.0	0.0	**5.0**	0.0 (Liver)	0.0
Lung Patient 8	**0.050**	0.0	0.0	**2.500**	**0.050**	0.0	0.0	0.0	**0.100**	0.0		
Lung Patient 9	0.0	0.0	0.0	0.0	**0.450**	0.0	0.0	0.0	**0.050**	0.0	**0.600** (Aorta)	0.0
Lung Patient 10	0.0	0.0	**0.050**	0.0	0.0	0.0	0.0	0.0	**0.100**	**2.500**	**0.250** (Stomach)	0.0

The results indicate that in the majority of the patients, the dosimetric difference between the undeformed and deformed scans on the OAR is close to 0. The difference appears mostly in the ipsilateral lung on which the tumor is present. Considering the results in OAR and also the conclusions made on the target structure in the previous section, it has been observed that the absolute difference mean dose in the ipsilateral lung is higher for the patients who have the tumor isolated inside the lung parenchyma, with the values ranging between 0.40%

to 1.050% of the prescribed dose whereas it ranges between 0.0% to 0.30% of the prescribed dose in the patients with the tumor close to the soft tissue. Nevertheless, the difference between these two patient groups is small being about 1%, confirming that TP optimization satisfied constraints on OARs.

5.4 Results of Dosimetric Analysis on Abdominal Clinical Data

The dosimetric impact of geometric distortions in the abdominal region is tested on 8 clinical cases comprising of 4 liver cancer cases and 4 pancreas cancer cases. All of the treatment plan design parameters, dose distributions and DVH results for the liver and pancreas cases are reported in Appendix C and Appendix D, respectively.

5.4.1 Liver Cases

Results in Target Structure

Table 13 shows the differences of the dosimetric parameters between the undeformed and deformed dose distributions in the CTV structure in the liver region. Differences in $D_{2\%}$, $D_{98\%}$, and D_{mean} parameters are normalized to the prescribed dose in liver treatment plans, 2 Gy. DHI is presented as an absolute difference.

Table 13 Differences of dosimetric parameters in CTV region between undeformed and deformed dose distributions belonging to clinical liver cases ($D_{2\%}$, $D_{98\%}$, D_{mean} parameters are normalized with respect to the prescribed dose, 2 Gy, and given in percentage)

	$D_{2\%}$ (%)	**$D_{98\%}$ (%)**	**D_{mean} (%)**	**Dose Homogeneity Index (DHI)**
Liver Patient 1	**0.100**	**0.100**	0.0	**0.001**
Liver Patient 2	**0.100**	0.0	**0.100**	**0.001**
Liver Patient 3	0.0	0.0	**0.050**	0.0
Liver Patient 4	0.0	0.0	**0.050**	**0.001**
Mean Difference	**0.050%**	**0.025%**	**0.050 %**	**0.001**

The dosimetric differences between the undeformed and deformed scans are very small in the liver cases, with a maximum value of 0.1% of the prescribed dose. Moreover, the dosimetric differences in different parameters are approximately at the same levels, differently from the lung cases. Figure 43 shows that both the ranges and values of the difference in dosimetric parameters are very small.

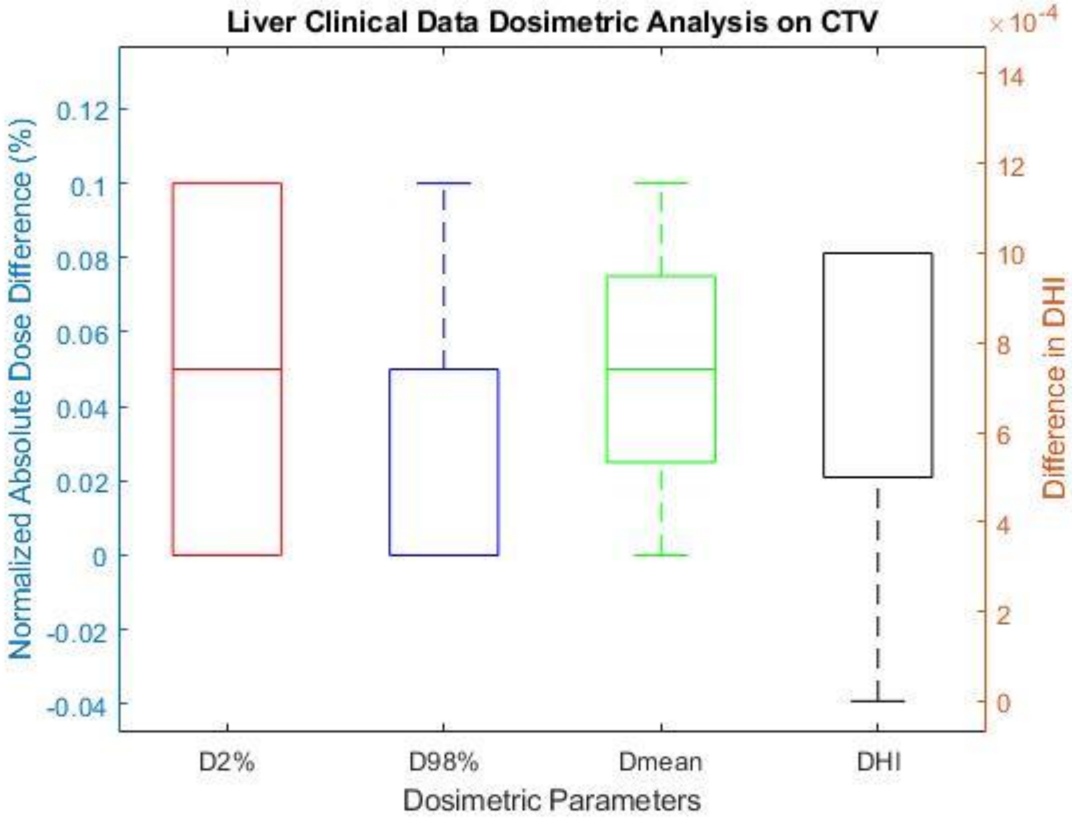

Figure 43 Box plot for liver clinical data in which dose differences between undeformed and deformed target dose for $D_{2\%}$, $D_{98\%}$ and D_{mean} parameters, normalized with respect to the prescribed dose, are shown in red, blue and green respectively with their y-axis on

DVH plots in all of the liver cases show also similar patterns. Figure 44 and Figure 45 show the dose distributions together with their DVH plots belonging to Patient 2 and 3 respectively.

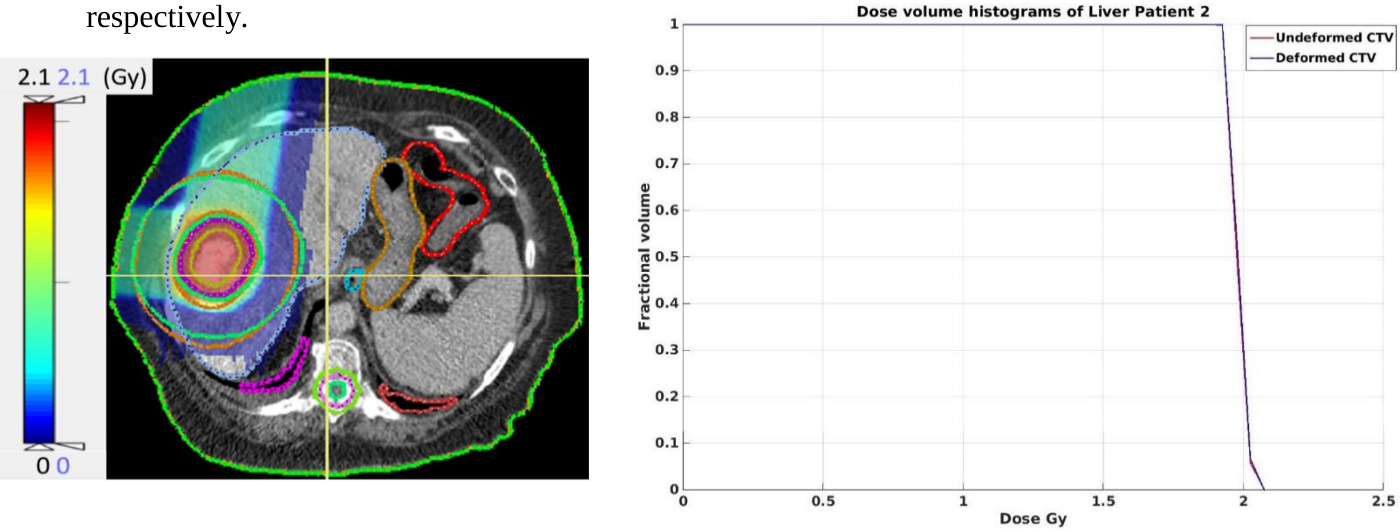

(a) (b)

Figure 44 Results for Liver Patient 2 with (a) Dose distribution for the deformed scan (b) DVH plot of undeformed, in red, and deformed scans, in blue with the x-axis representing the dose and y-axis representing the fractional volume

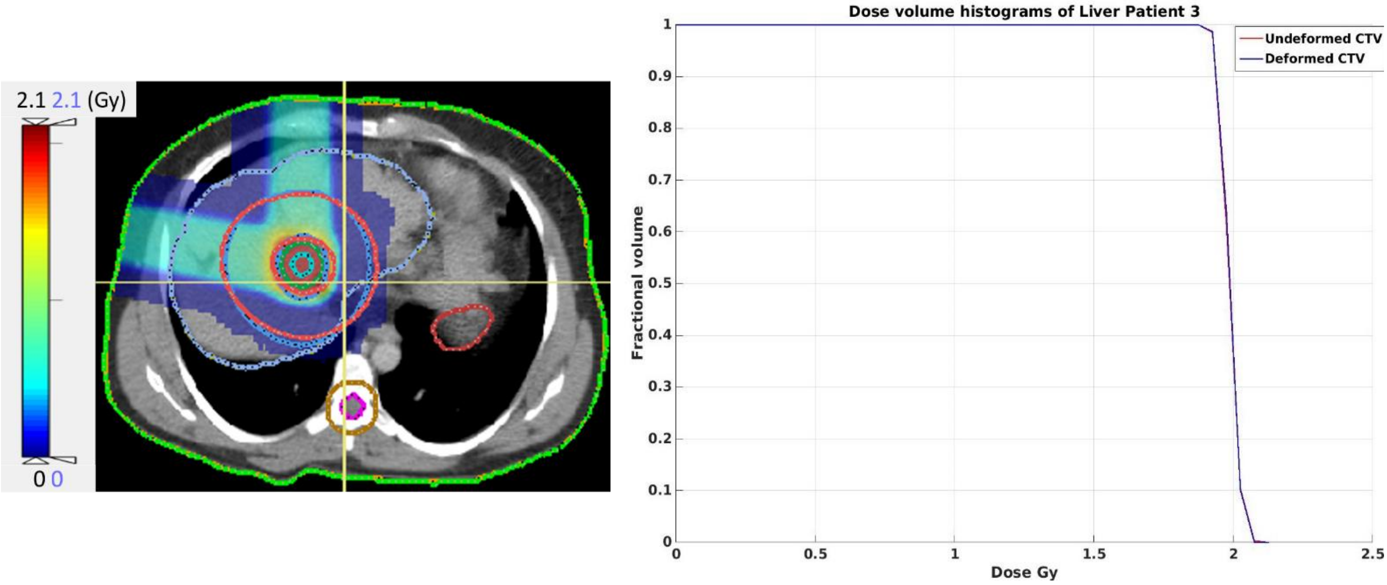

(a) (b)

Figure 45 Results for Liver Patient 3 with (a) Dose distribution for the deformed scan (b) DVH plot of undeformed, in red, and deformed scans, in blue with the x-axis representing the dose and y-axis representing the fractional volume

DVH plots of undeformed and deformed scans are very similar in behavior and very close to each other. Unlike in lung cases, there is almost no difference in the liver plots in the region where the curve bends. The numeric results and DVH plots agree with the results of the liver phantom. In all of the clinical liver data, tumors are close to other soft tissues and the beam does not encounter high density variations on its path. Therefore, the range is conformal to the target resulting in differences between undeformed and deformed scans going up to a maximum value of 0.1% of the prescribed dose.

Results in Organs at Risk

The dosimetric effect of geometric distortions is assessed on the OAR for each liver case in terms of mean dose, D_{mean}, and maximum dose, D_{max}. Since the liver is in the abdomen, organs in the abdominal region and spinal cord are considered as OARs for the liver case. Liver, right kidney, spinal cord, stomach, and large intestine are the organs evaluated in all of the liver patients to see the effect of geometric distortions on the dose in OAR. The absolute difference results for the OARs in liver patients are given in Table 14. The values different than 0 are indicated in bold.

Table 14 Absolute differences in mean and maximum dose in the percentage of target prescribed dose, 2 Gy, in organs at risk in the clinical liver data

	Liver		**Right Kidney**		**Spinal Cord**		**Stomach**		**Large Intestine**	
	Mean (%)	***Max (%)***	***Mean (%)***	***Max (%)***	***Mean (%)***	***Max (%)***	***Mean (%)***	***Max (%)***	***Mean (%)***	***Max (%)***
Liver Patient 1	**0.100**	0.0	**0.100**	**2.500**	0.0	0.0	0.0	0.0	0.0	**2.500**
Liver Patient 2	0.0	0.0	0.0	0.0	0.0	0.0	0.0	0.0	0.0	0.0
Liver Patient 3	**0.100**	0.0	0.0	0.0	0.0	0.0	0.0	0.0	0.0	0.0
Liver Patient 4	0.0	**2.500**	0.0	0.0	0.0	0.0	0.0	0.0	0.0	**2.500**

The dosimetric differences between the undeformed and deformed scans in the OARs are very small, i.e. 0.0 Gy in the majority of the OARs for both D_{mean} and D_{max}. It has a maximum of 0.1% and 2.5% of the prescribe dose for the D_{mean} and D_{max} respectively. In patients 1 & 4, the dosimetric differences are observed in large intestine only in the maximum dose. Unlike the mean dose, which is averaged across the volume of the region of interest, the maximum dose is a point dose. Therefore, these differences in the maximum dose with the value of 2.5% of the prescribed dose are interpreted to be arising due to locational hot spots. The same applies to the maximum liver dose for patient 4. On the other hand, it can be seen that the difference appears in the liver organ in 3 of the 4 cases. Since the treatment is planned on the liver, it is as expected to have the difference as the majority of the dose is spread mainly in this organ.

5.4.2 Pancreas Cases

Results in Target Structure

Table 15 shows the differences between the undeformed and deformed dose distributions in the CTV volume in the pancreas region. Differences in $D_{2\%}$, $D_{98\%}$, and D_{mean} parameters are normalized to the prescribed dose in pancreas treatment plans, which is 3 Gy. DHI is not normalized.

Table 15 Differences of Dosimetric Parameters in CTV region between undeformed and deformed dose distributions belonging to clinical pancreas cases ($D_{2\%}$, $D_{98\%}$, D_{mean} parameters are normalized to the prescribed dose,3 Gy, and given in percentage)

	$D_{2\%}$ (%)	$D_{98\%}$ (%)	D_{mean} (%)	Dose Homogeneity Index (DHI)
Pancreas Patient 1	0.0	**0.067**	**0.033**	0
Pancreas Patient 2	**0.067**	**0.133**	**0.133**	**0.003**
Pancreas Patient 3	**0.067**	**0.067**	0.0	0
Pancreas Patient 4	0.0	**0.133**	0.0	0
Mean Difference	**0.033**	**0.100**	**0.042**	**0.001**

The dosimetric differences of the undeformed and deformed scans in the pancreas cases are very small in terms of different dosimetric parameters, reaching up to 0.133% of the prescribed dose. Moreover, looking at the mean differences of different dosimetric parameters described as normalized to the prescribed dose, it can be concluded that there is not a comparable difference between $D_{2\%}$, $D_{98\%}$, and D_{mean} parameters. As it can be seen in the box plot in Figure 46, the dosimetric differences have a similar interquartile range and values for different parameters with the $D_{98\%}$ dose difference having slightly higher values.

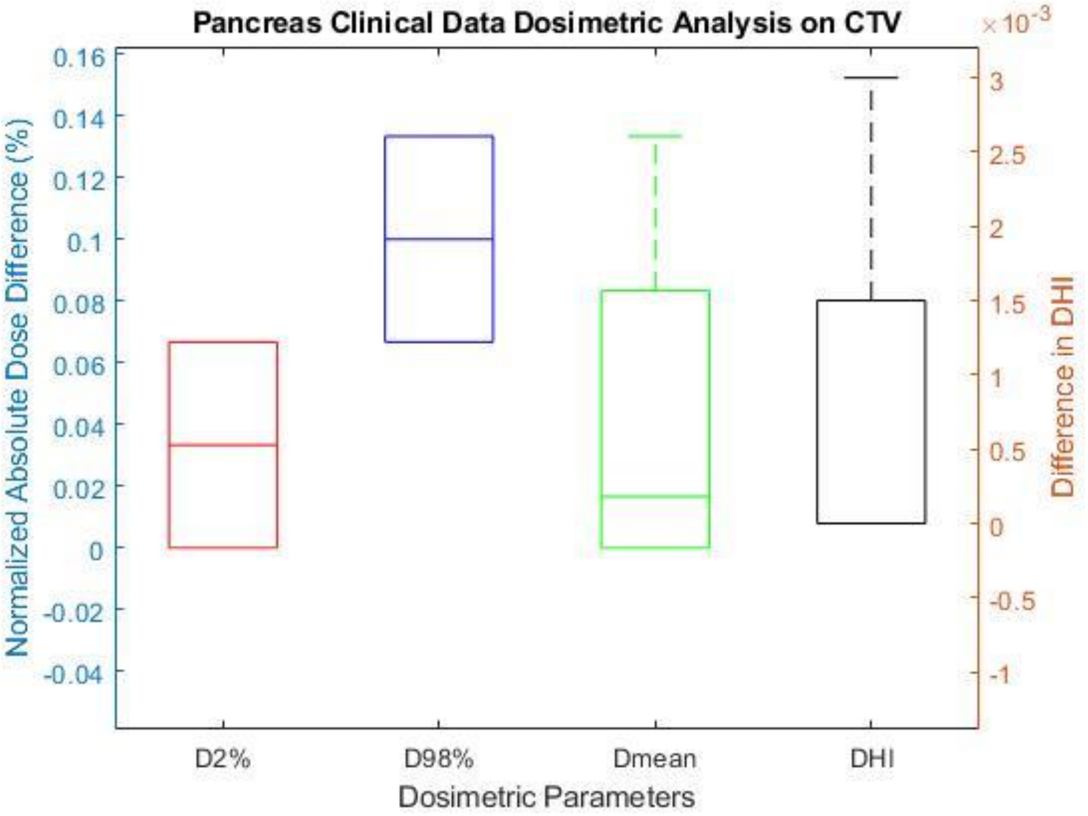

Figure 46 Box plot for pancreas clinical data in which dose differences between undeformed and deformed target dose for $D_{2\%}$, $D_{98\%}$ and D_{mean} parameters, normalized with respect to the prescribed dose, are shown in red, blue and green respectively with their y-axis

DVH plots in all of the pancreas cases show similar pattern as for liver. In Figure 47 and Figure 48, the dose distributions together with their DVH plots are presented for patients 2 and 3, respectively, for the evaluation of the dosimetric impact of geometric distortions in the pancreas region.

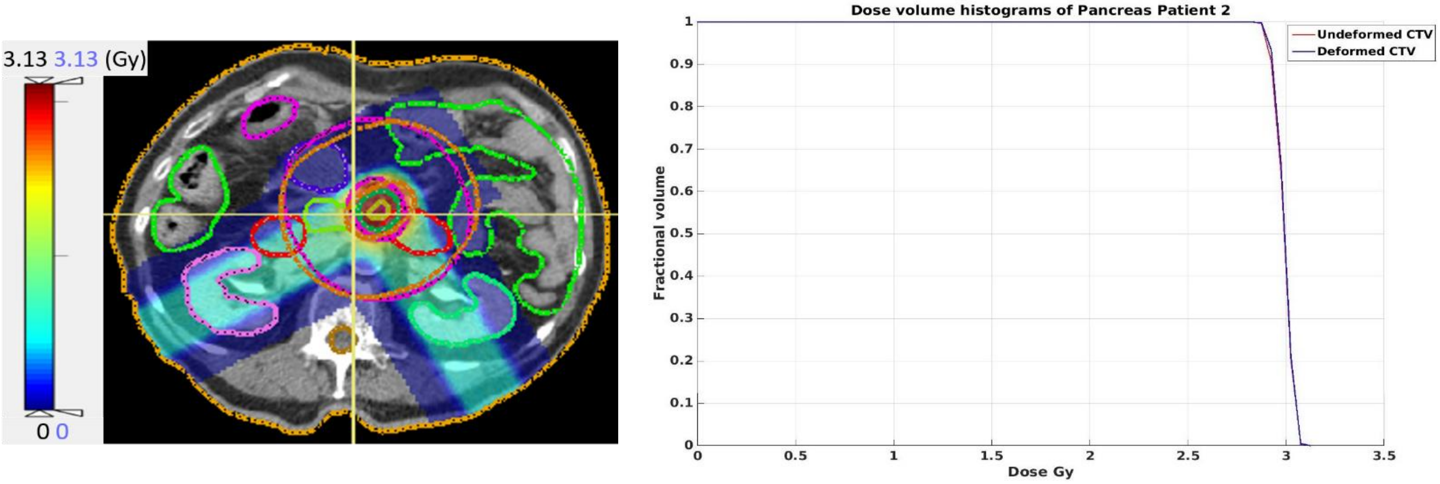

(a) (b)

Figure 47 Results for Pancreas Patient 2 with (a) Dose distribution for the deformed scan (b) DVH plot of undeformed, in red, and deformed scans, in blue with the x-axis representing the dose and y-axis representing the fractional volume

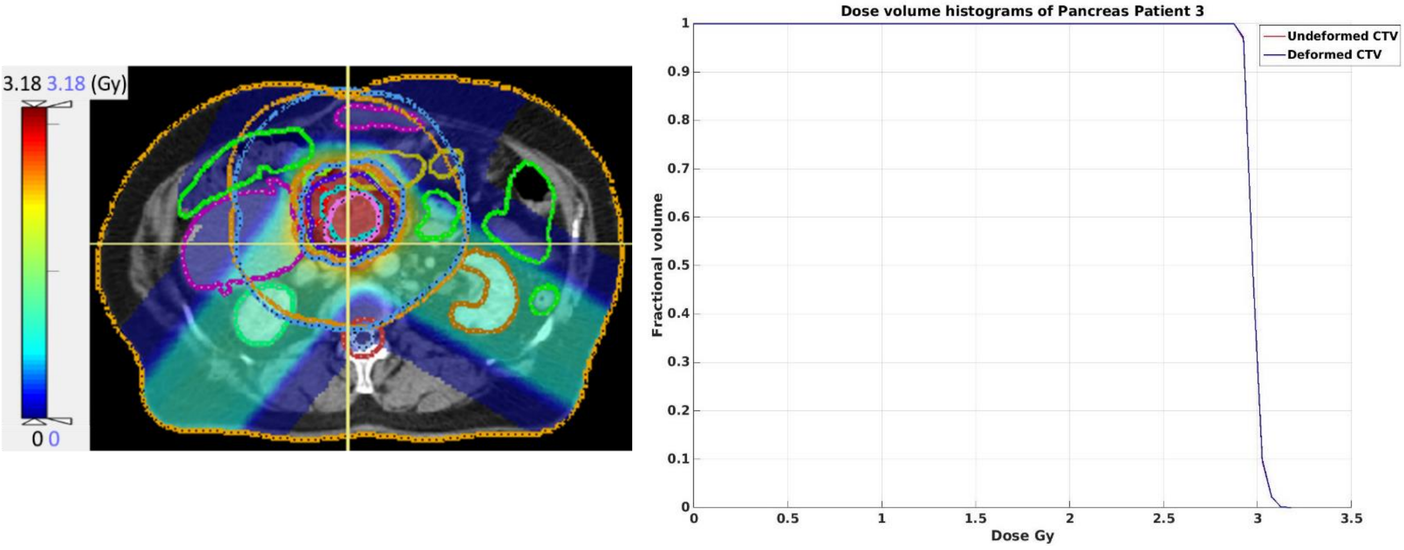

(a) (b)

Figure 48 Results for Pancreas Patient 3 with (a) Dose distribution for the deformed scan (b) DVH plot of undeformed, in red, and deformed scans, in blue with the x-axis representing the dose and y-axis representing the fractional volume

In the pancreas cases, the resulting dose distributions have very small differences between the undeformed and deformed scans. Therefore, their DVH plots have similar behavior and are very close to each other with slight differences as in the liver cases. The results are in agreement with the pancreas phantom results.

In the pancreas region, the tumor is present on the soft tissue. Like in the liver cases, the beam does not encounter high gradients in the density homogeneities on its path around the tumor resulting in small differences not reaching more than 0.133% of the prescribed dose in the pancreas region.

Results in Organs at Risk

The dosimetric effect of geometric distortions is assessed on the OARs for each pancreas case in terms of mean dose, D_{mean}, and maximum dose, D_{max}. The OARs evaluated in pancreas cases are spinal cord, liver, stomach, large intestine, and left and right kidneys. The absolute difference results for OARs are given in Table 16 with the values different than 0 indicated in bold.

Table 16 Normalized differences in mean and maximum dose in the percentage of target prescribed dose, 3 Gy, in organs at risk in the clinical pancreas data

	Spinal Cord		**Liver**		**Stomach**		**Large Intestine**		**Left Kidney**		**Right Kidney**	
	Mean (%)	***Max (%)***	***Mean (%)***	***Max (%)***	***Mean (%)***	***Max (%)***	***Mean (%)***	***Max (%)***	***Mean (%)***	***Max (%)***	***Mean (%)***	***Max (%)***
Pancreas Patient 1	**0.067**	0.0	**0.033**	0.0	**0.267**	0.0	**0.100**	**3.333**	**0.033**	0.0	**0.100**	0.0
Pancreas Patient 2	0.0	0.0	0.0	0.0	**0.033**	0.0	0.0	**1.667**	**0.033**	0.0	**0.233**	0.0
Pancreas Patient 3	0.0	0.0	**0.067**	0.0	**0.033**	0.0	**0.200**	0.0	**0.067**	0.0	**0.033**	0.0
Pancreas Patient 4	0.0	0.0	**0.033**	0.0	0.0	0.0	**0.100**	**1.667**	**0.067**	0.0	**0.200**	0.0

In all of the patients, the difference between undeformed and deformed scans can be seen in D_{mean} in the left and right kidneys reaching a maximum value of 0.233% of the prescribed dose, which is neglectable since it meets the constraints in OARs. Moreover, a difference is seen in the mean dose in the stomach for patients 1,2 and 3 and in the liver and large intestine for patients 1, 3 and 4, due to the design of TP with two oblique fields. Nevertheless, these differences are still within the constraints defined in OARs, in the organs on the beam path. These results are in agreement with what has been observed also in the pancreas phantom.

5.5 Statistical Analysis of the Results

With the aim of determining if the dosimetric differences between the undeformed and deformed scans are statistically significant, statistical analysis is performed separately on each dosimetric parameter in the target volume and organs at risk. Firstly, in order to determine if the dosimetric data has the same distribution among different regions for each dosimetric parameter, Kruskal-Wallis test is applied to the undeformed and deformed dosimetric results. The dosimetric results for the $D_{2\%}$, $D_{98\%}$, and D_{mean} parameters are normalized to the prescribed dose. The significance level to reject or accept the null hypothesis that the different regions have the same distribution is set to the default value, 5%. If the resulting ρ parameter of Kruskal-Wallis test is greater than 5%, the hypothesis is rejected and the group, which has a different rank, is determined. After the Kruskal-Wallis test, paired, two-sided Wilcoxon signed-rank test is applied to the undeformed-deformed result pairs. According to the results of Kruskal-Wallis test, if different regions are found to have the same distribution, Wilcoxon signed-rank test is applied on a single dataset including the undeformed-deformed dose pairs of all of the regions. If the hypothesis is rejected as a result of Kruskal-Wallis test for any dose parameter, groups are separated according to their distribution, and Wilcoxon signed-rank test for that parameter is performed separately on the groups, which have been determined to have different distributions. The significance level is set as 5 % also in Wilcoxon signed-rank test with the null hypothesis that the difference between undeformed and deformed scans come from a distribution with zero median.

5.5.1 Analysis on Target Structure

Statistical analysis is applied on parameters $D_{2\%}$, $D_{98\%}$, and D_{mean} normalized with respect to the prescribed dose, which is 2 Gy in lung and liver and 3 Gy in the pancreas region. The difference in the DHI parameter is not normalized since it is in the 0-1 scale. Resulting ρ parameters as a result of the Kruskal-Wallis test applied to the dosimetric parameters used for CTV is given in Table 17.

Table 17 Kruskal-Wallis test results for CTV dosimetric parameters performed on undeformed and deformed dose results in different regions where $D_{2\%}$, $D_{98\%}$, D_{mean} parameters are normalized with respect to the prescribed dose

Dosimetric Parameter	**ρ Parameter**
$D_{2\%}$	0.147
$D_{98\%}$	0.066
D_{mean}	0.101
Dose Homogeneity Index	0.300

The returned values of ρ parameters as a result of Kruskal-Wallis test performed on the normalized undeformed and deformed dosimetric results in different regions indicate that in all of the dosimetric parameters regarding the target structure, different regions come from the same distribution at a 5 % significance level. Therefore, according to the results of this test, it is concluded that there is no need to separate the dosimetric results belonging to different regions and Wilcoxon signed-rank test can be performed on the undeformed-deformed result pairs on a single dataset comprising 3 region groups all together. The results of Wilcoxon signed-rank test applied separately on the CTV dosimetric parameters are given in Table 18.

Table 18 Wilcoxon signed-rank test results for CTV dosimetric parameters performed on undeformed and deformed pairs, where $D_{2\%}$, $D_{98\%}$, D_{mean} parameters are normalized with respect to the prescribed dose, on single dataset comprising of 3 investigated anatomical regions

Dosimetric Parameter	**ρ Parameter**
$D_{2\%}$	0.022
$D_{98\%}$	6.104×10^{-5}
D_{mean}	6.104×10^{-5}
Dose Homogeneity Index	8.545×10^{-4}

All of the ρ parameters belonging to different dosimetric parameters in the target structure are below the significance level of 5%. Therefore, the test rejects in all of the dosimetric parameters in the CTV the null hypothesis, which states that the distribution of difference of undeformed and deformed scans has the zero median. Therefore, according to the Wilcoxon signed-rank test, the dosimetric impact of geometric distortions are found statistically different in the target volume for all of the examined dosimetric parameters. However, it should be also highlighted at this point that the returned ρ parameter for $D_{2\%}$ is very close to 5% significance level and if the significance level was chosen as 1%, it could meet the null hypothesis. Therefore, regarding this parameter, a comparison with a larger dataset would give a more accurate conclusion.

5.5.2 Analysis on Organs at Risk

Wilcoxon signed-rank test is applied to the undeformed-deformed dose result pairs separately for the dosimetric parameters D_{mean} and D_{max}, on the single dataset comprising 3 region groups. The ρ parameters are returned to be 0.094 and 0.333 for the D_{mean} and D_{max} respectively. As both of these ρ parameter values are greater than 5%, it can be concluded that undeformed and deformed doses in the OARs have an identical median so that the distribution of difference of undeformed and deformed doses has a zero-median and the test fails to reject the null hypothesis at the default 5% significance level. Therefore, the geometric distortions wouldn’t lead to considerable dosimetric changes in OARs.

5.6 Comparison of Target Results Among Different Regions

After the statistical analysis of the undeformed and deformed scans in the whole dataset to conclude statistically on the effect of the geometric distortions in the CTV, another comparison is carried out in order to determine if the dosimetric impact of the geometric distortions on the target structure differs in between and among the lung, liver and pancreas regions. The variance of dosimetric differences between the undeformed and deformed doses in different regions is tested only in the target structure since the Wilcoxon signed-rank test results in statistically significant differences only in the target structure, and not in OARs. The analysis is performed separately on the dosimetric parameters $D_{2\%}$, $D_{98\%}$, D_{mean}, and DHI in the CTV volumes.

In order to test if the variance in the range of the dosimetric parameters is statistically different among different regions, Kruskal-Wallis test is performed separately for each parameter. The significance level for this test is set to 5% to indicate if the absolute differences in each dosimetric parameter have a statistically significant different distribution in different regions. Table 19 presents the results of the Kruskal-Wallis test for each target dosimetric parameter.

Table 19 Kruskal-Wallis test results for target dosimetric parameters performed on differences of undeformed and deformed dose results in different regions where $D_{2\%}$, $D_{98\%}$, D_{mean} parameters are normalized with respect to the prescribed dose

Dosimetric Parameter	**ρ Parameter**
$D_{2\%}$	0.317
$D_{98\%}$	0.001
D_{mean}	0.063
Dose Homogeneity Index	0.002

The Kruskal-Wallis tests returning ρ parameters greater than 5% significance level for $D_{2\%}$ and D_{mean} dose parameters accept the null hypothesis that the dose difference data for $D_{2\%}$ and D_{mean} come from the same distribution in different regions. It indicates that the dosimetric differences between the undeformed and deformed scans do not demonstrate a statistically significant different distribution in different regions for these parameters. However, the test performed on $D_{98\%}$ and DHI parameters resulting in ρ values smaller than 5% significance level rejects the null hypothesis that the absolute difference dose data have the same distributions in different regions for these parameters. Therefore, it indicates that there are statistically significant differences between the regions for the ranges of $D_{98\%}$ and DHI absolute dose differences. In order to identify which region comes from a different distribution, a multiple comparison follow-up test is conducted. Figure 49 shows the distribution of mean ranks of the three regions for the $D_{98\%}$ and DHI parameters.

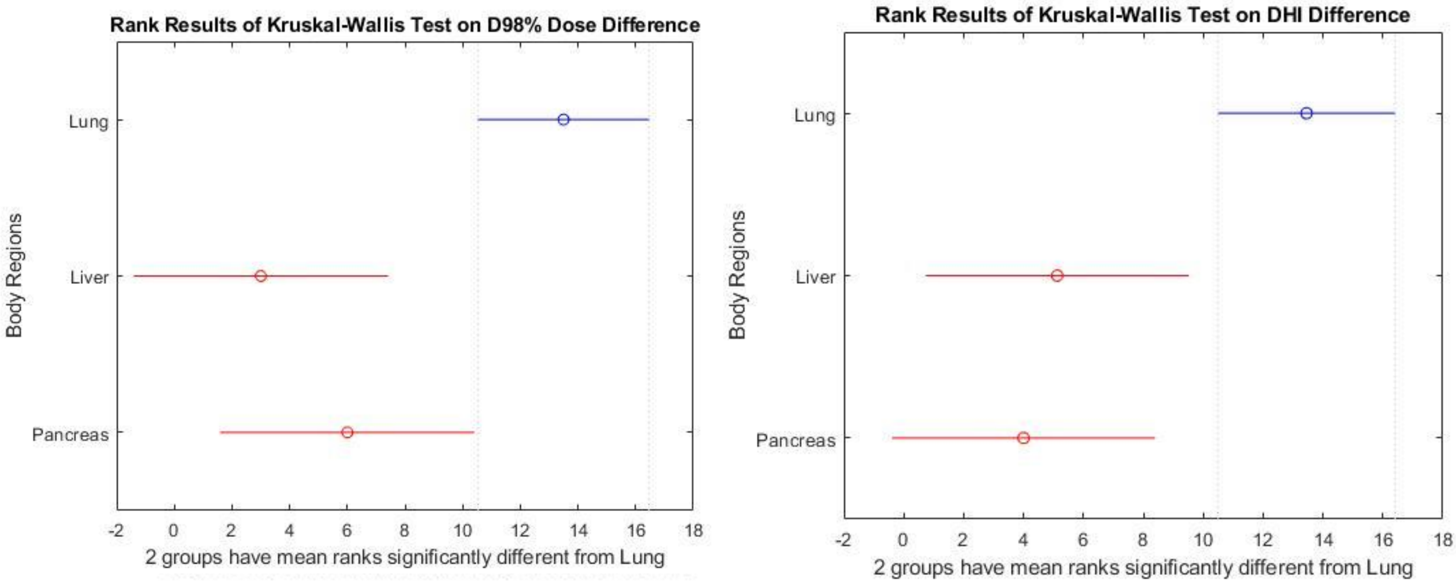

(a) (b)

Figure 49 Rank Results of Kruskal-Wallis test performed on (a)$D_{98\%}$ normalized dose difference and (b) DHI difference results in different anatomical regions

As it is visualized in the rank plots of different regions for the $D_{98\%}$ and DHI parameters, as a result of Kruskal-Wallis and multiple comparison follow-up test, it has been found that there is not a significant difference between the liver and pancreas regions, so that the test accepts the null hypothesis that the absolute dose difference in these two groups come from the same distribution. However, the dose difference in terms of the $D_{98\%}$ and DHI parameters in the lung comes from a different distribution than the other regions. Higher dose difference ranges in the lung region for these parameters are visualized in Figure 50 and confirmed to be statistically different from other regions.

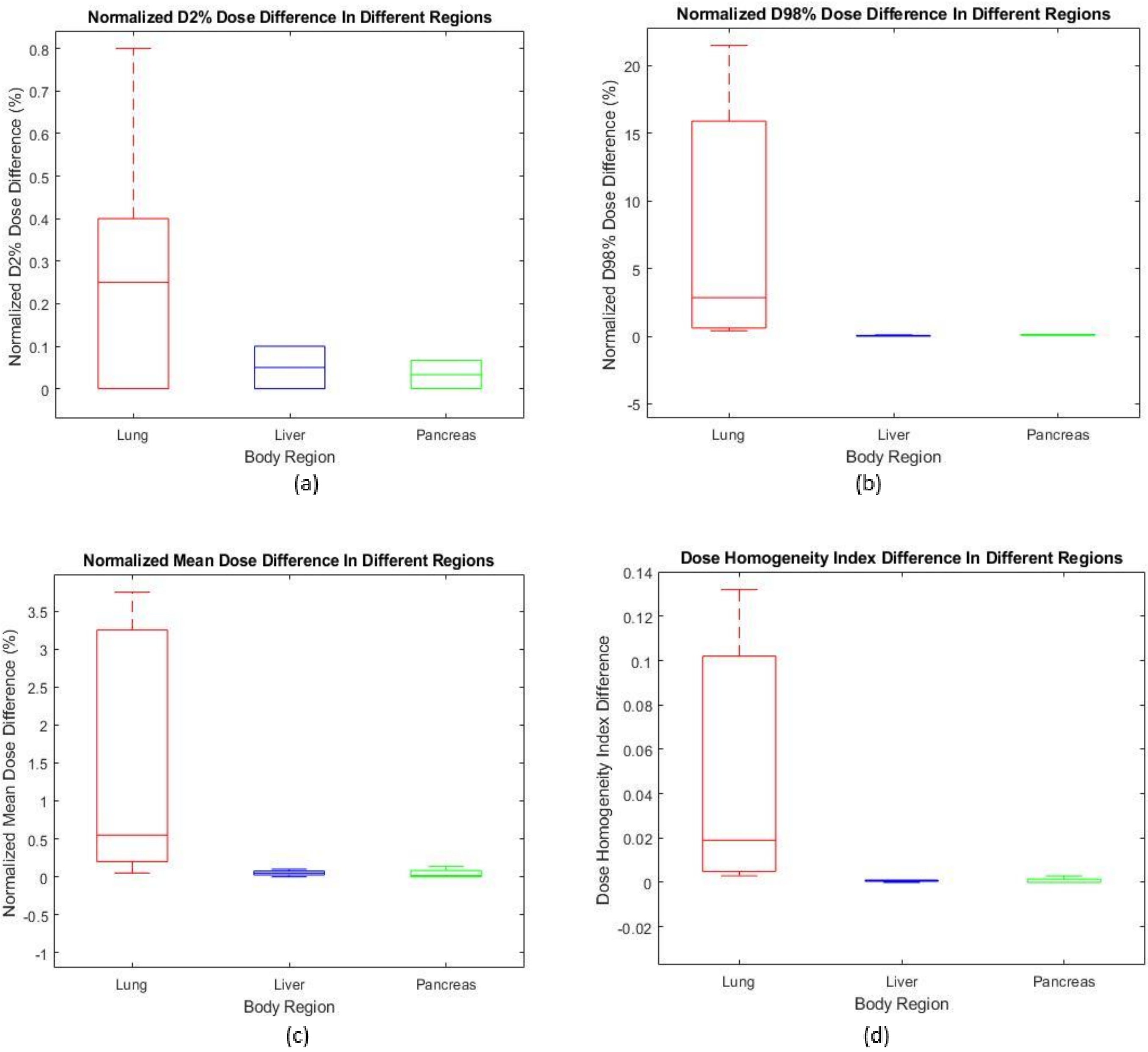

Figure 50 Box plot of the (a) $D_{2\%}$ differences normalized with respect to the prescribed dose (b) $D_{98\%}$ differences normalized with respect to the prescribed dose (c) D_{mean} differences normalized with respect to the prescribed dose (d) DHI differences in different anatomical regions

As mentioned in 'Results of Dosimetric Analysis on Thorax Clinical Data' section, higher dose difference ranges in the lung region is due to the fact that density variations along the beam path can cause higher dose differences as seen for lung patients with the tumor located in lung parenchyma with respect to cases in which the tumor is close to soft tissues. Therefore, as demonstrated by the Kruskal-Wallis test, due to the high variability of the tumor location in the lung patients, the dose difference in terms of $D_{98\%}$ and DHI parameters comes from a different distribution in the lung cases.

6 CONCLUSIONS

In the clinically used current practice, CT/MRI hybrid workflow used for the treatment planning has several limitations including the introduction of systematic spatial uncertainties due to CT/MRI image registration, inter-scanner differences between two imaging sessions, patient exposure to ionizing radiation, and overall cost considerations. In this context, MRI-only workflows would stand as a solution eliminating the limitations arising from the CT/MRI hybrid workflow. However, at the same time, MRI introduces system-dependent and patient-dependent geometric distortions. A method has been implemented in this thesis to determine and quantify the dosimetric uncertainties arising from the geometric distortions in MRI-only proton therapy in extra-cranial sites, in collaboration with Ludwig Maximilians University, Munich. The developed methodology is based on describing the geometric distortions arising from MRI by applying a displacement map quantified in a previous study by Kroll (2018) on the CT images. The demonstrated geometric distortions in the FLASH sequence has a maximal mean landmark deformation per image slice of up to 3 mm in slice selection direction at a slice shifted 105 mm away from the isocenter and mean in-slice landmark deformation up to 1 mm. This workflow has allowed us to quantify and analyze the dosimetric changes arising from the system- and patient-induced geometric distortions without any need for a clinical trial and synthetic CT generation.

In order to determine the dosimetric impact of geometric distortions, treatment plan simulations are performed on 4D-CT/MRI digital phantoms and 4D-CT clinical dataset of the thoracoabdominal site. Since the extracranial sites are of concern in this study, usage of 4D CT data has played a crucial role in motion compensation through the gating technique (i.e. planning and treatment in a specific respiratory phase). Moreover, the dataset comprising of phantoms enabled us to demonstrate the dosimetric changes on a realistic human model and provide a reference from which to evaluate and verify the results in clinical data. As mentioned in the results, the dosimetric results in phantoms and clinical data are in agreement with each other in each body region studied in the scope of this work. Thus, the conclusions on the dosimetric impact reached in the clinical dataset are confirmed by the phantom results, which stand as a gold standard.

As a result of the analysis performed on the final dose distributions of the clinical dataset, the dosimetric differences between undeformed and deformed dose pairs were found to go up to 0.8%, 21.5%, and 3.750% of the prescribed dose in terms of the dose parameters $D_{2\%}$, $D_{98\%}$ and D_{mean}, respectively. For the DHI parameter, the difference was found to have a maximum value of 0.132. In order to determine if the differences, found in terms of $D_{2\%}$, $D_{98\%}$, D_{mean}, and DHI dosimetric parameters, between the paired undeformed and deformed dose (normalized with respect to the prescribed dose in $D_{2\%}$, $D_{98\%}$, D_{mean} parameters) were statistically significant, Wilcoxon signed-rank test was performed on the clinical dataset comprising all of the investigated anatomical regions. According to this test, the paired undeformed and deformed dosimetric results were found to be statistically different at the 5% significance level, thus confirming that system- and patient-induced geometric distortions lead to statistically significant dosimetric changes in the target structure. However, since the returned ρ parameter for $D_{2\%}$ with the value of 0.022 is very close to 5% significance level, regarding this parameter a comparison with a larger dataset would give a more accurate conclusion. On the contrary, dosimetric differences were negligible on organs at risk and did not result significant. This result confirms the advantage of proton therapy in the delivery of conformal dose to the target and sparing of surrounding tissues over conventional radiotherapy. Indeed, in this study, treatment planning on the beam specific PTV margins, which is brought with the advantage of proton therapy over conventional radiotherapy, contributed to the delivery of conformal dose to the target.

Determining that the undeformed and deformed doses are statistically different, the analysis has been narrowed down to each anatomical site and their comparison. As regards the results in the specific anatomical sites, the dosimetric impact of geometric distortions in the CTV structure was found to be the smallest in the abdomen regions rather than the thorax. Indeed, Kruskal-Wallis test performed on the difference of the undeformed and deformed target dose (normalized with respect to the prescribed dose) has concluded that the difference dose in lung has different distributions than liver and pancreas in terms of $D_{98\%}$ and DHI parameters: a dose difference range in $D_{98\%}$ parameter of 0.40% to 21.5%, 0.0% to 0.10%, and 0.067% to 0.13% of the prescribed dose was quantified for thorax, liver, and pancreas, respectively. Specifically, we noticed that geometric distortions cause a smaller dosimetric change in the target structure for the tumors located close to or covered by the soft tissue. This is not the case for the lung site, where the tumor can be either close to soft tissue or isolated inside the lung parenchyma. As higher dose differences were found in this latter case, it leads to higher dose difference ranges among the lung cases. While for the lung patients with the tumor close to soft tissue, the normalized dose differences stay in the levels of maximum 0.4%, 5.60%, and 0.85% of the prescribed dose for the dose parameters $D_{2\%}$, $D_{98\%}$, and D_{mean}, respectively and go up to 0.0270 in DHI, for the other patients with tumor isolated inside the lung parenchyma, highest dosimetric differences were observed going up to 0.80%, 21.50% and 3.750% of the prescribed dose for the $D_{2\%}$, $D_{98\%}$, and D_{mean} parameters, respectively and 0.132 for the DHI parameter. As covered in the Results & Discussion section, this difference is mainly due to the fact that the beam travels on a path with high density variations in the lung region and thus potentially leading to miss of the target (Engelsman & Kooy, 2005) by the shift of the Bragg peak. As the tissue density variations around the tumor are higher in the case where the tumor is isolated inside the lung parenchyma, the dosimetric differences are found to be higher for these cases.

Up to the current knowledge, all of the studies on the investigation of the effect of system- and patient-induced image distortions in MRI-only workflow on the radiation dose are made in conventional radiation therapy (Adjeiwaah et al., 2018, Gustafsson, Nordström, Persson, Brynolfsson, & Olsson, 2017, Yan et al., 2018, Sun et al., 2015, Bolard & Bulling, 2016). Although a direct comparison between our study (related to MRI-only proton therapy) and the previous studies in the literature is not possible since they use conventional radiotherapy and evaluate different body regions, their results are in line with our findings. In a study by Gustafsson aimed to investigate the dosimetric effects of MRI system-specific distortion in a prostate MRI-only radiotherapy workflow, the mean dose deviation and dosimetric impact on OARs are found to be negligible (Gustafsson et al., 2017) supporting the results of our work. Another study conducted by Yan et al. (2018) to investigate the impact of hardware-related geometric distortion of MRI when using MR images for planning in IMRT, the analysis was performed on CT-based treatment plans of 14 patients with gastrointestinal, genitourinary, thoracic, head and neck, or spinal tumors. It has been concluded that distortions did not result in clinically meaningful dose deviations relative to the prescribed plans for 9 out of 14 patients. For the other 5 patients, including liver, prostate and head and neck cases, MRI distortions caused up to 3.6 % loss of target coverage (Yan et al., 2018). Relying on the fact that dosimetric impact is found clinically important in terms of loss of target coverage in a liver case, it can be suggested that distortions in MRI-only workflow in this region can be better compensated with proton therapy. However, more trials are needed for a valid comparison.

In conclusion of the present study, while the dosimetric impact of system- and patient-induced geometric distortions in MRI-only proton therapy workflow has been found to be higher for the lung cases where the tumor is isolated inside the lung parenchyma away from the soft tissue, it is reported to be much smaller in the abdominal and thorax cases where the tumor is closed or covered by the soft tissue. This study, therefore, suggests the potential applicability of MRI-only proton therapy, provided that more clinical trials would be required to conclude on the dosimetric impact of MRI distortions when the tumor is isolated from soft tissue in the lung parenchyma.

As the studies based on MRI-only proton therapy workflow in the thoracoabdominal regions are limited in the literature, in light of the found results and conclusions, we put forward this study as a starting point for further research to carry MRI-only proton therapy workflow into clinical practice.

7 IMPROVEMENTS & FUTURE DEVELOPMENTS

Although we provided promising results for MRI-only proton therapy, further work is still required to strengthen our findings.

Firstly, an analysis on a larger dataset including different body regions with more samples would definitely contribute to taking the effectiveness of an MRI-only workflow safely into the clinical practice. The effect of geometric distortions in the thorax cases where the tumor is isolated inside the lung parenchyma away from the soft tissue has been found to be significantly higher than other cases reflecting on 3 lung patients. In order to be able to conclude more accurately on this hypothesis, analysis with more cases is required.

In the treatment planning, pencil beam-based optimization approaches are used in this study. According to different studies, the introduction of Monte Carlo (MC) algorithms may provide more robust and accurate planning and can improve therapeutic benefit (Sasidharan et al., 2019, Maes et al., 2018, Liang et al, 2018) since the analytical dose calculation algorithms typically neglect the position of the inhomogeneities relative to the Bragg peak depth by calculating the range based on the water-equivalent depth (Urie, Goitein & Wagner, 1984, Paganetti, 2012). In order to provide a more robust and accurate treatment planning especially for the lung, MC optimization is worth to be investigated (Maes et al., 2018). Therefore, the dosimetric impact of geometric distortions can be evaluated with a further study using MC algorithms.

Lastly, in the designed study, the dosimetric impact was not influenced by any errors that could originate from synthetic CT generation in an MRI-only workflow. In order to consider all the real-life application aspects of MRI-only proton therapy and test the feasibility of this workflow in the clinical practice, this study requires to be continued with a further analysis including the uncertainties introduced by the synthetic CT generation methods in the workflow. Earlier studies aimed to study the dose difference in generated synthetic CTs compared to conventional CTs in Intensity Modulated Radiotherapy report dose differences typically below 1% when atlas-based or voxel-based synthetic CT generation methods are used (Johnstone et al., 2018). Moreover, in several studies with heterogeneous bulk density override, the dose difference is reported to be below 2% (Doemer et al., 2015, Karotki, Mah, Meijer & Meltsner, 2011, Chen et al., 2004).

8 Appendix A - Treatment Plan Simulations for COMBAT Phantoms

Table 20 Treatment planning design parameters for phantoms

	Beam Angles	**OAR Sparing Ring Radius (cm)**
Lung Phantom (Tumor close to soft tissue)	0° - 280°	3
Lung Phantom (Tumor isolated in lung parenchyma)	0° - 280°	3
Liver Phantom	10° - 275°	3
Pancreas Phantom	150° - 200°	4

Lung Phantom with Tumor Close to Soft Tissue

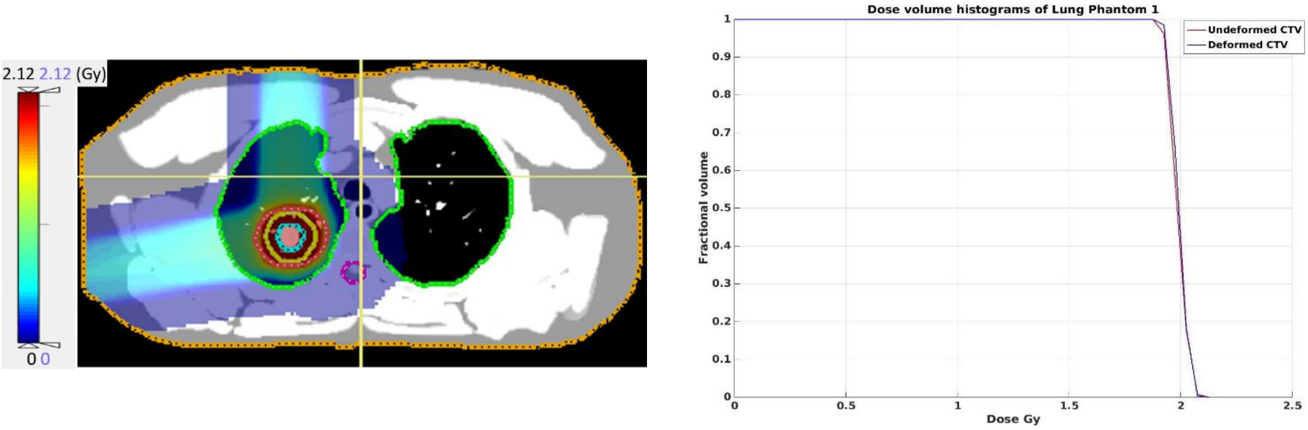

(a) (b)

Figure 51 Dose distribution of deformed scan (on the left) and DVH plot (on the right with red line belonging to undeformed scan and blue line belonging to deformed scan) of Lung phantom with tumor close to soft tissue

Lung Phantom with Tumor Isolated in the Lung Parenchyma

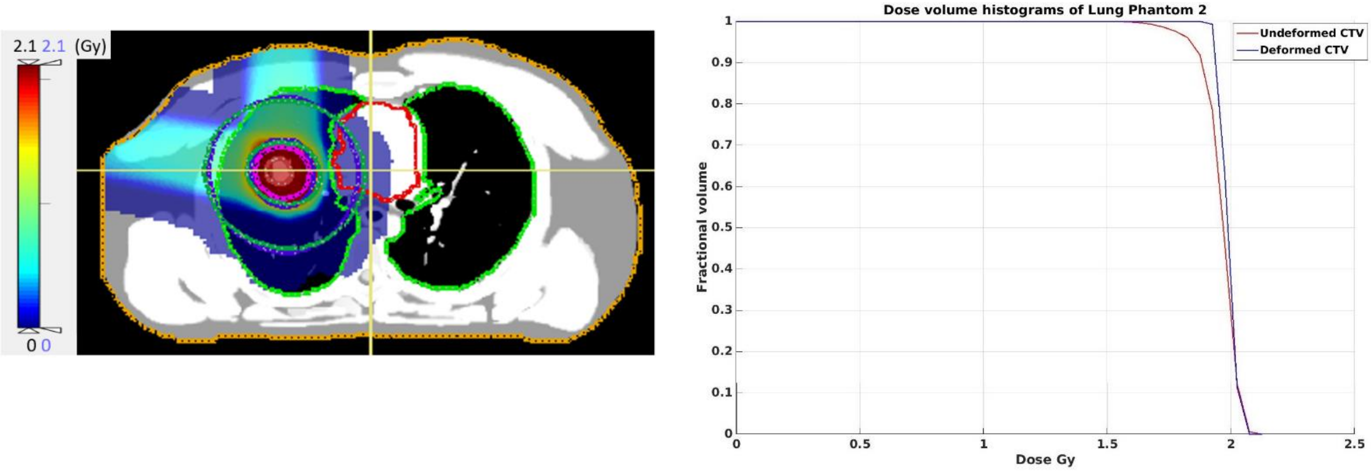

(a) (b)

Liver Phantom

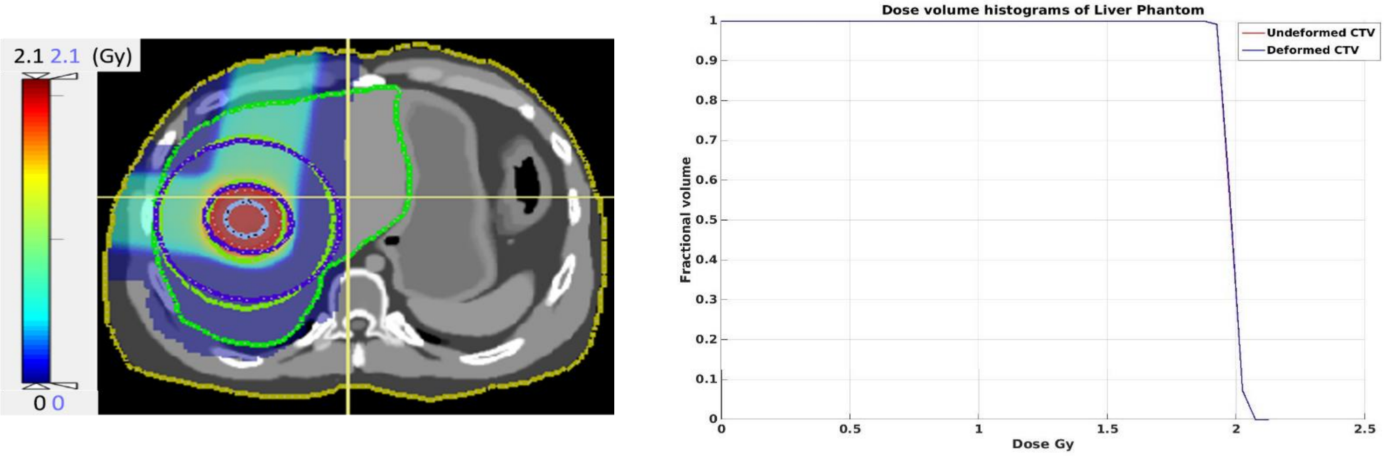

(a) (b)

Pancreas Phantom

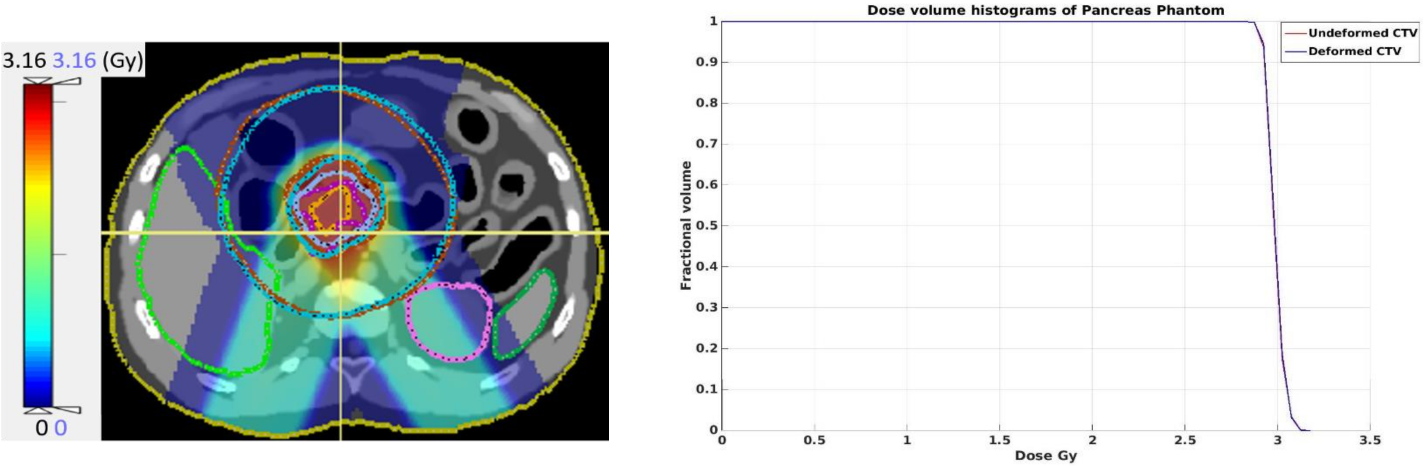

(a) (b)

Figure 52 Dose distributions of deformed scans (on the left) and DVH plots (on the right with red line belonging to undeformed scan and blue line belonging to deformed scan) of Lung phantom with tumor isolated inside lung parenchyma, liver phantom and pancreas phantom (from top to bottom)

9 Appendix B - Treatment Plan Simulations for Lung Cancer Patients

Table 21 *Treatment planning design parameters for lung cancer patients*

	Beam Angles	**OAR Sparing Ring Radius (cm)**
Lung Patient 1	0° - 280°	3
Lung Patient 2	200° - 300°	3
Lung Patient 3	10° - 260°	3
Lung Patient 4	0° - 275°	4
Lung Patient 5	50° - 340°	3
Lung Patient 6	0° - 100°	3
Lung Patient 7	185° - 275°	4
Lung Patient 8	185° - 275°	4
Lung Patient 9	80° - 100°	4
Lung Patient 10	70° - 120°	4

Lung Patient 1

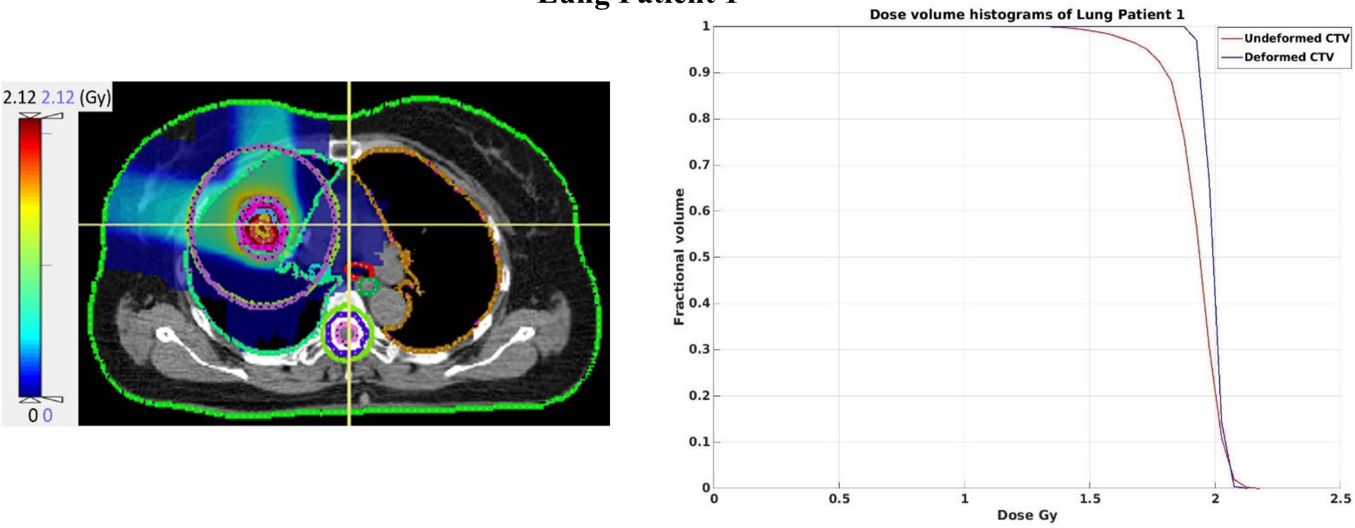

(a) (b)

Figure 53 Dose distribution of deformed scan (on the left) and DVH plot (on the right with red line belonging to undeformed scan and blue line belonging to deformed scan) of Lung patient 1

Lung Patient 2

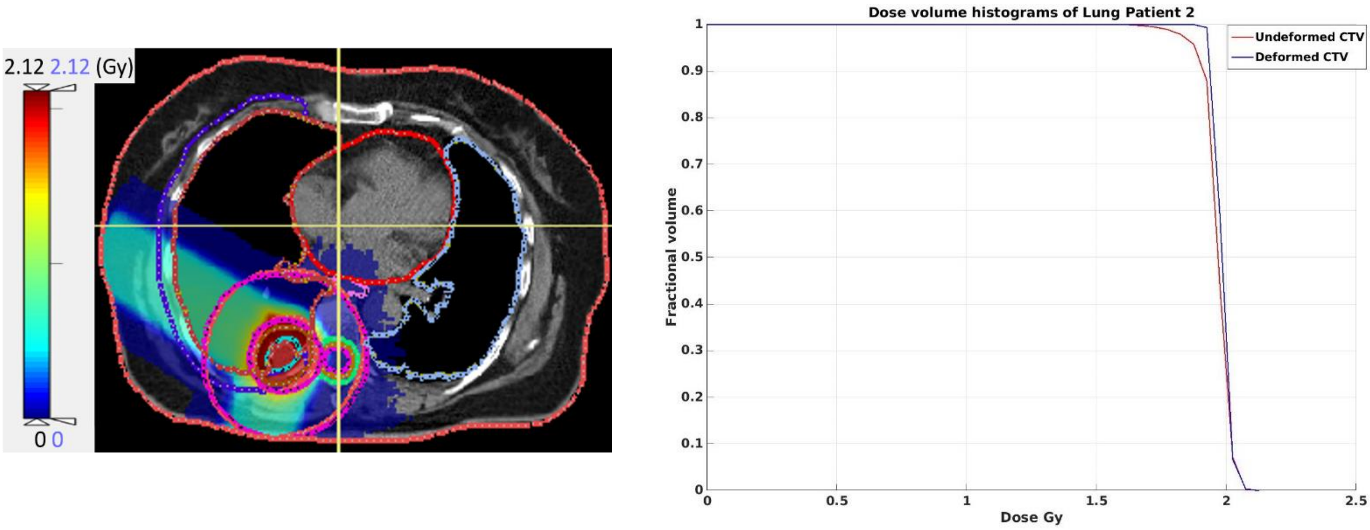

(a) (b)

Lung Patient 3

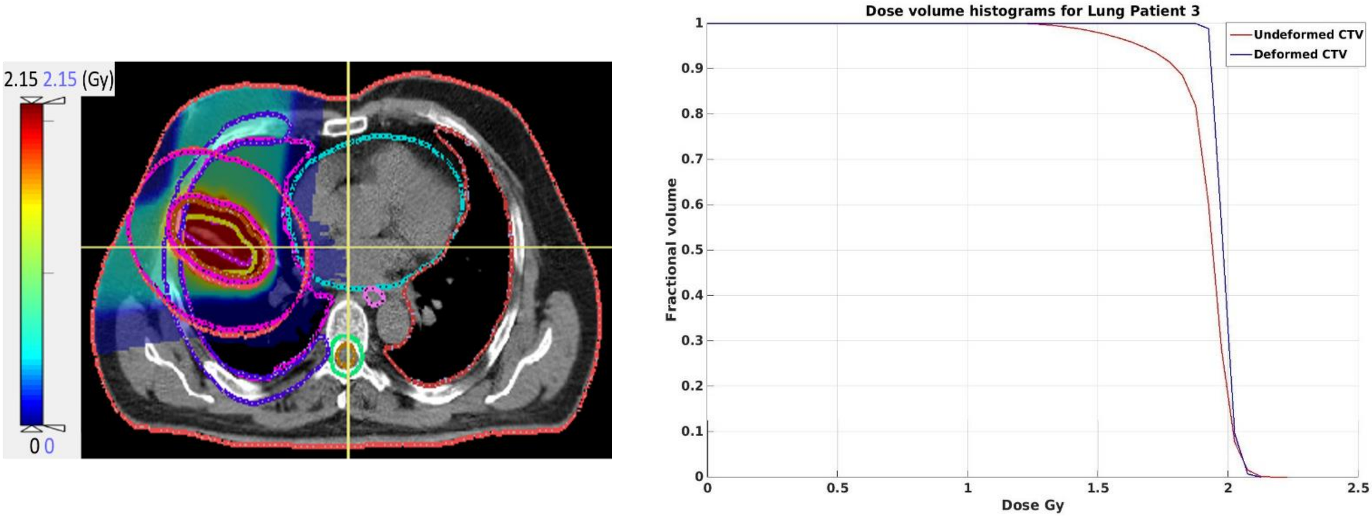

(a) (b)

Lung Patient 4

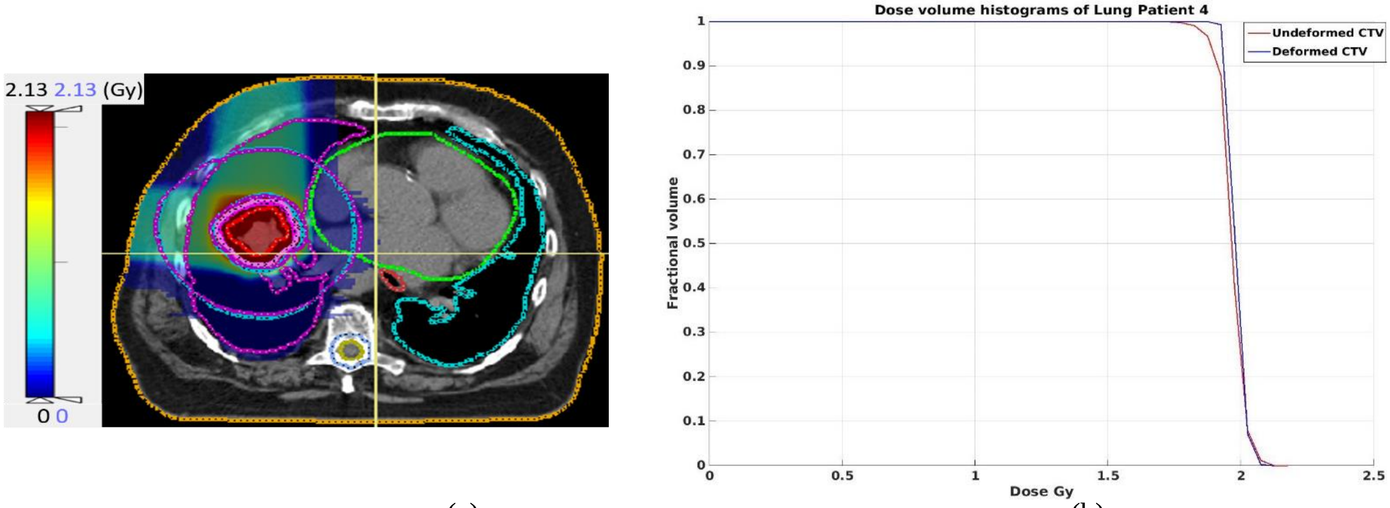

(a) (b)

Figure 54 Dose distributions of deformed scans (on the left) and DVH plots (on the right with red line belonging to undeformed scan and blue line belonging to deformed scan) of Lung Patients 2, 3 & 4

Lung Patient 5

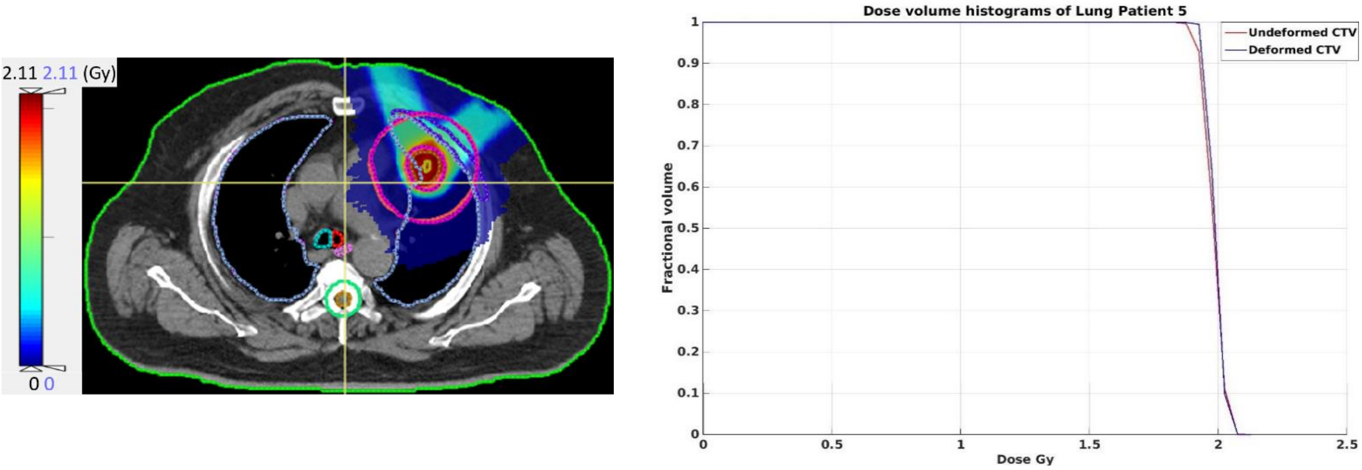

(a) (b)

Lung Patient 6

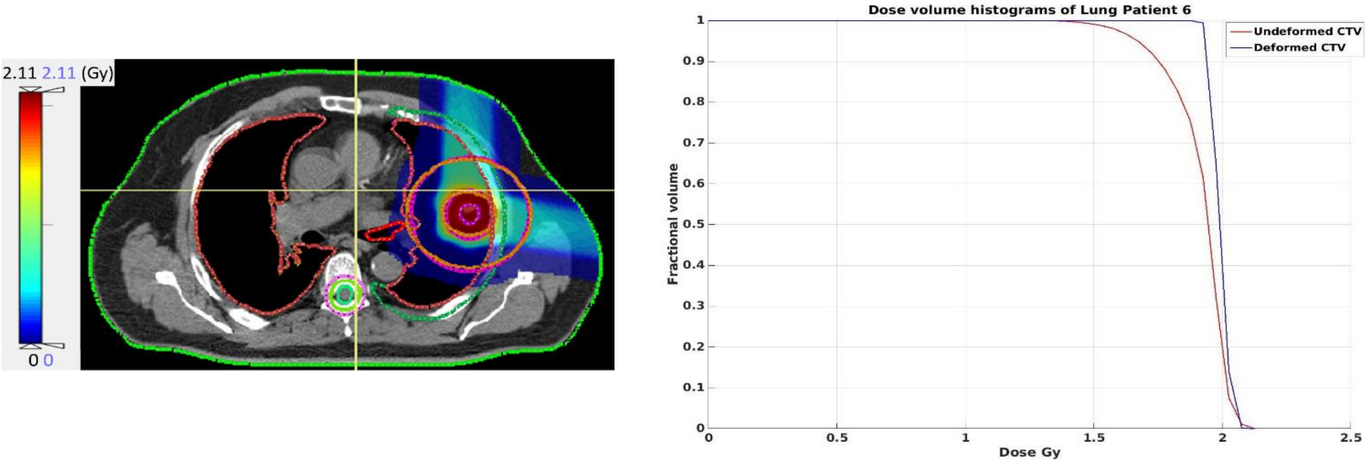

(a) (b)

Lung Patient 7

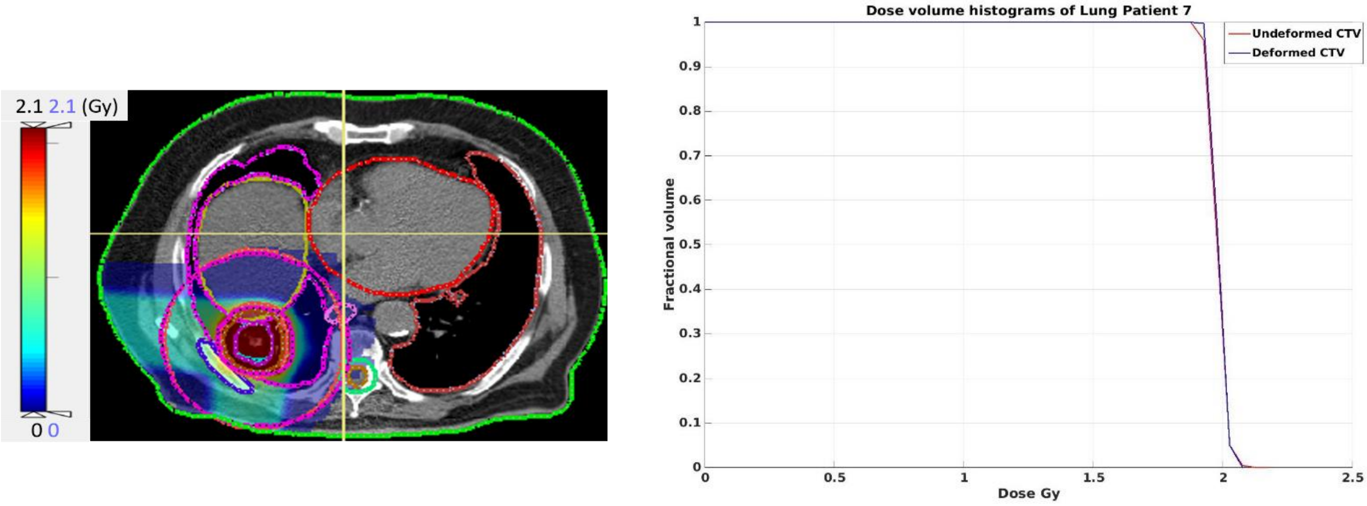

(a) (b)

Figure 55 Dose distributions of deformed scans (on the left) and DVH plots (on the right with red line belonging to undeformed scan and blue line belonging to deformed scan) of Lung Patients 5, 6 & 7

Lung Patient 8

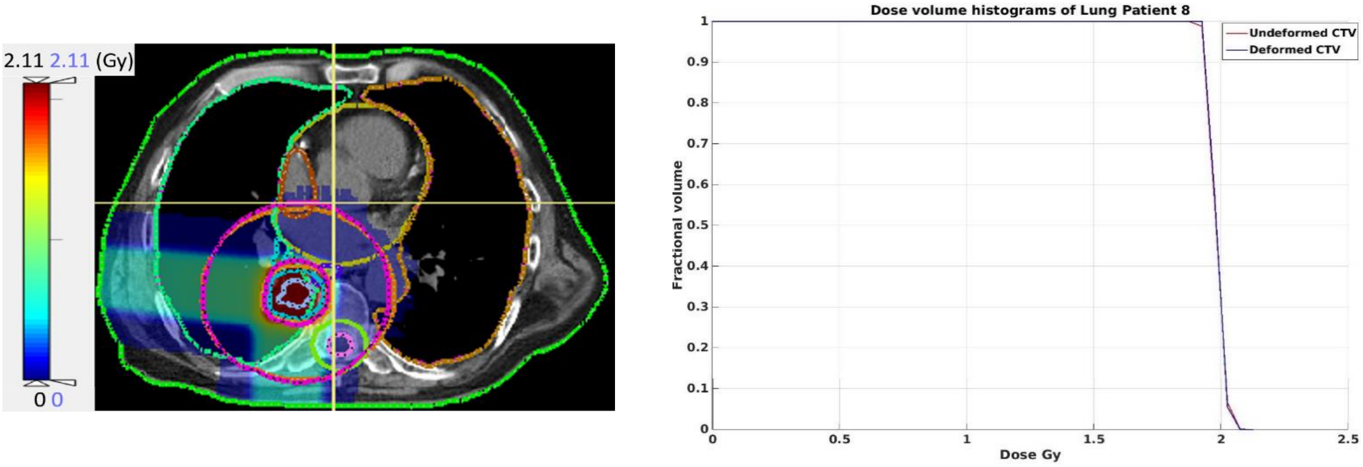

(a) (b)

Lung Patient 9

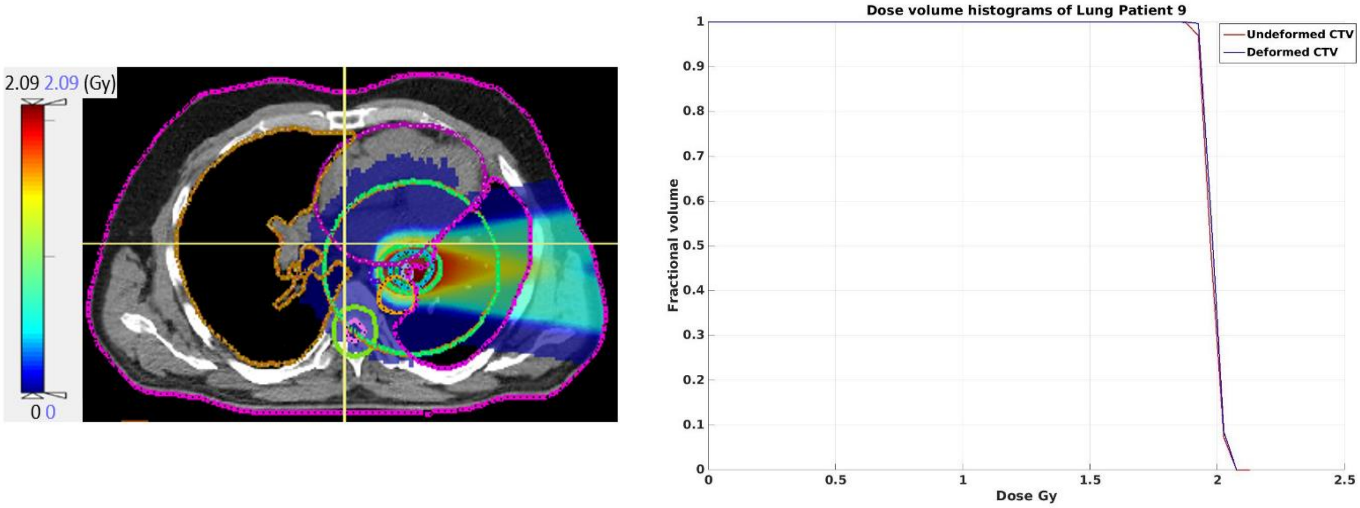

(a) (b)

Lung Patient 10

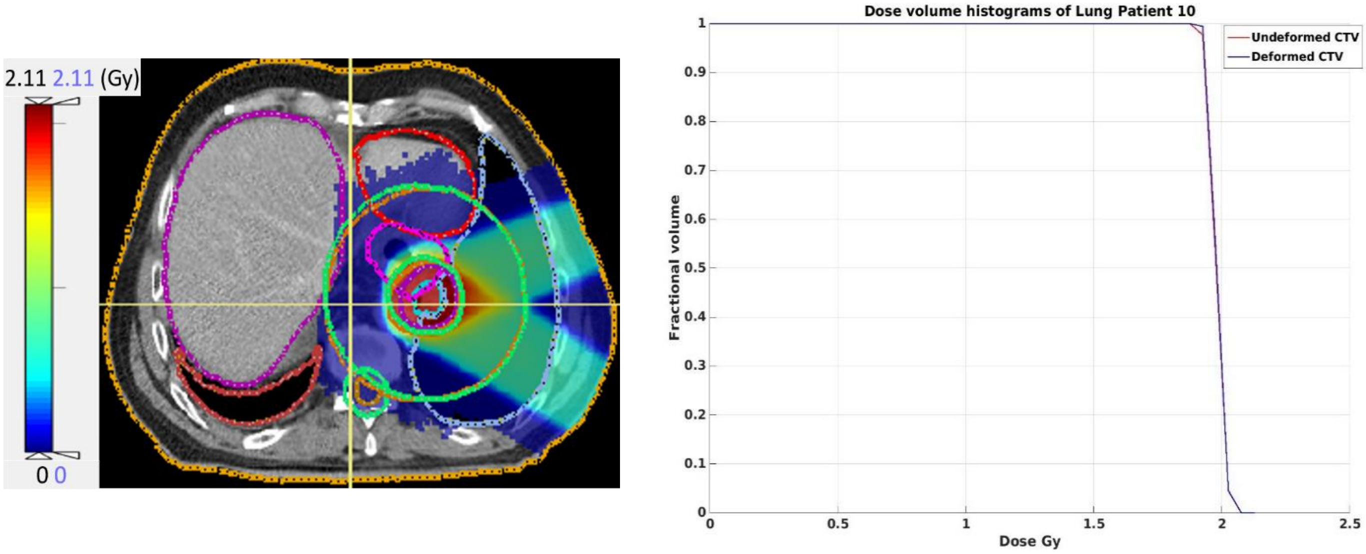

(a) (b)

Figure 56 Dose distributions of deformed scans (on the left) and DVH plots (on the right with red line belonging to undeformed scan and blue line belonging to deformed scan) of Lung Patients 8, 9 & 10

10 Appendix C - Treatment Plan Simulations for Liver Cancer Patients

Table 22 Treatment planning design parameters for liver cancer patients

	Beam Angles	OAR Sparing Ring Radius (cm)
Liver Patient 1	0° - 275°	3
Liver Patient 2	10° - 275°	3
Liver Patient 3	0° - 280°	3
Liver Patient 4	0° - 280°	3

Liver Patient 1

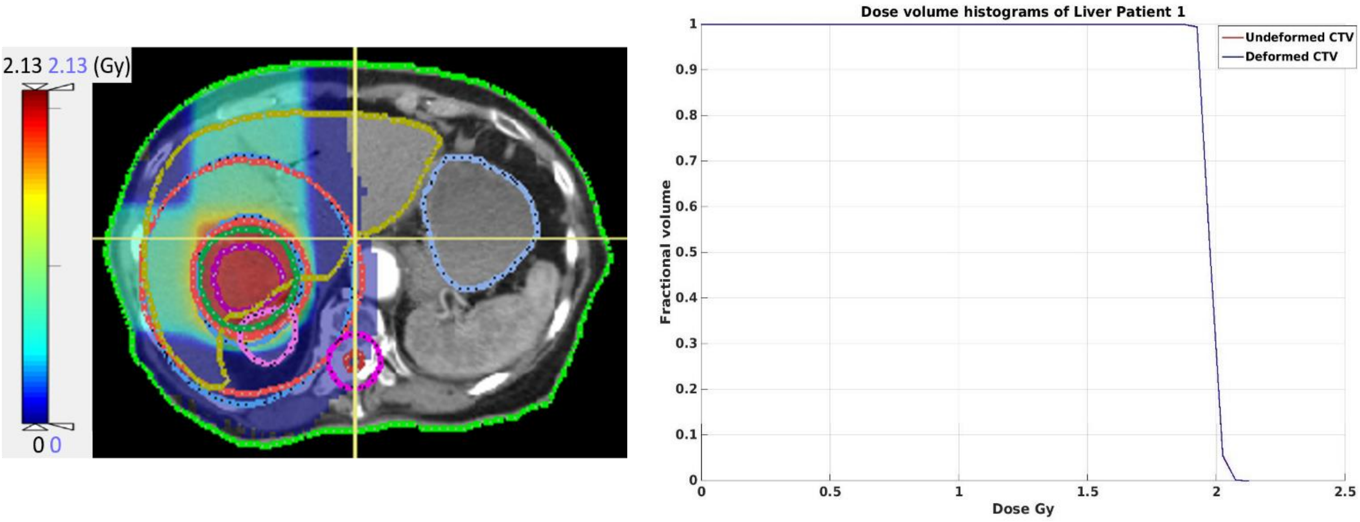

(a) (b)

Figure 57 Dose distribution of deformed scan (on the left) and DVH plot (on the right with red line belonging to undeformed scan and blue line belonging to deformed scan) of Liver patient 1

Liver Patient 2

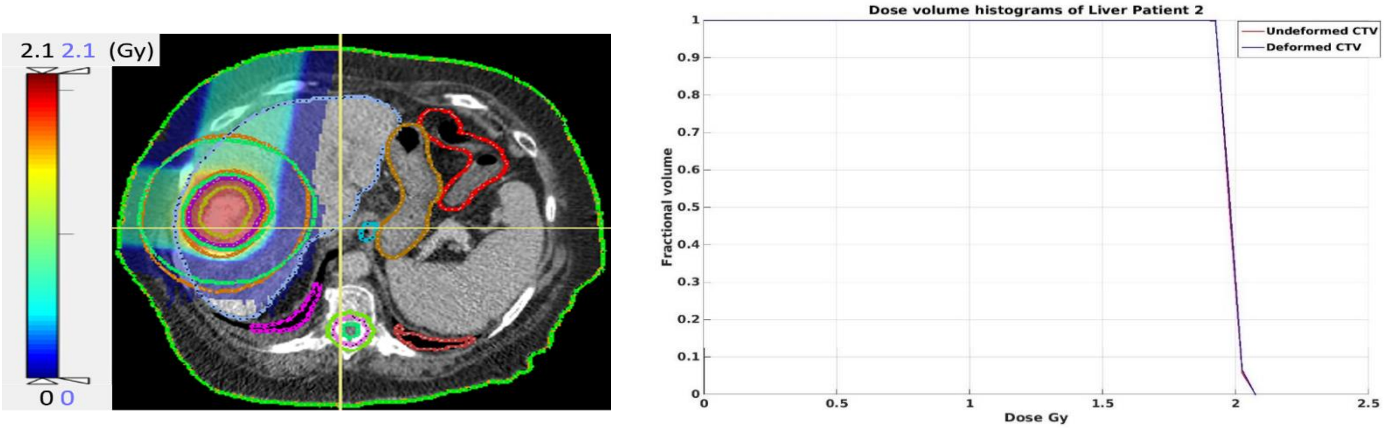

(a) (b)

Liver Patient 3

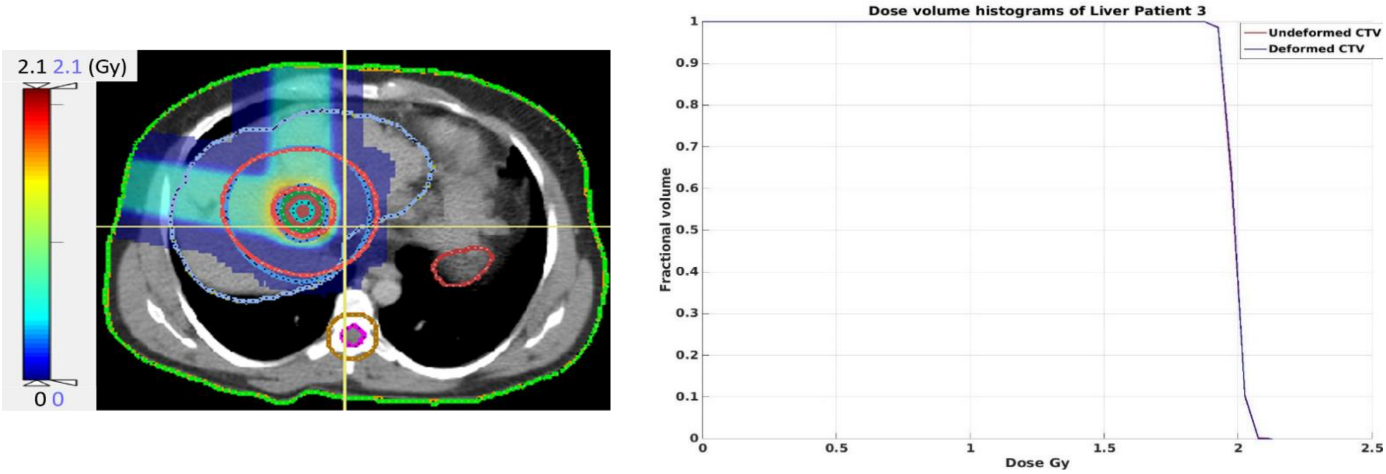

(a) (b)

Liver Patient 4

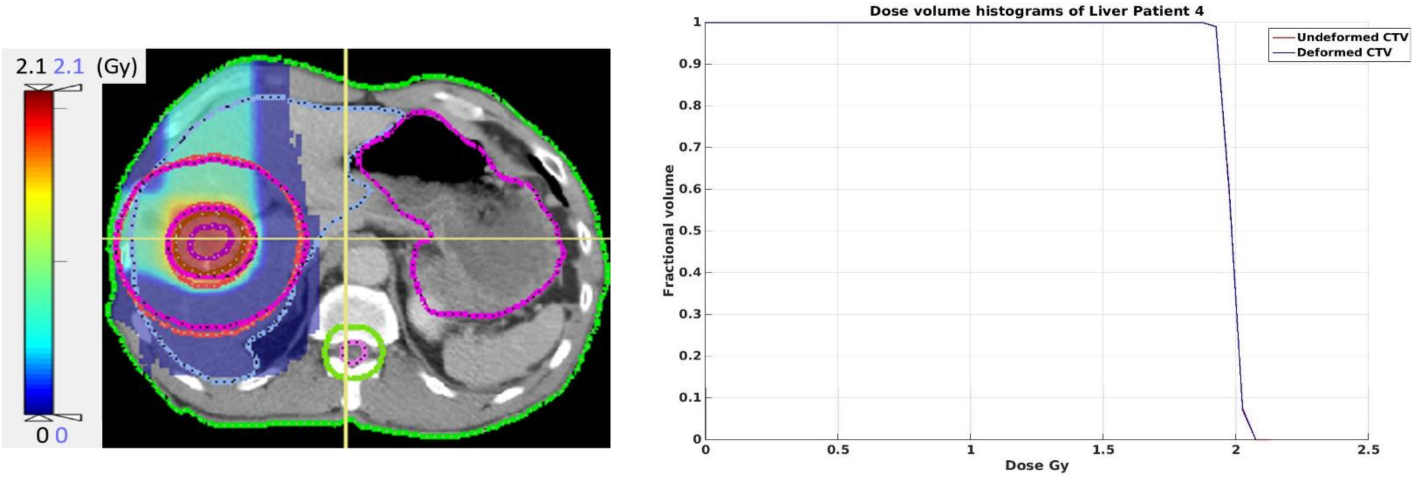

(a) (b)

Figure 58 Dose distributions of deformed scans (on the left) and DVH plots (on the right with red line belonging to undeformed scan and blue line belonging to deformed scan) of Liver Patients 2, 3 & 4

11 Appendix D – Treatment Plan Simulations for Pancreas Cancer Patients

Table 23 Treatment planning design parameters for pancreas cancer patients

	Beam Angles	**OAR Sparing Ring Radius (cm)**
Pancreas Patient 1	150° - 240°	3
Pancreas Patient 2	150° - 240°	4
Pancreas Patient 3	120° - 220°	4
Pancreas Patient 4	120° - 240°	3

Pancreas Patient 1

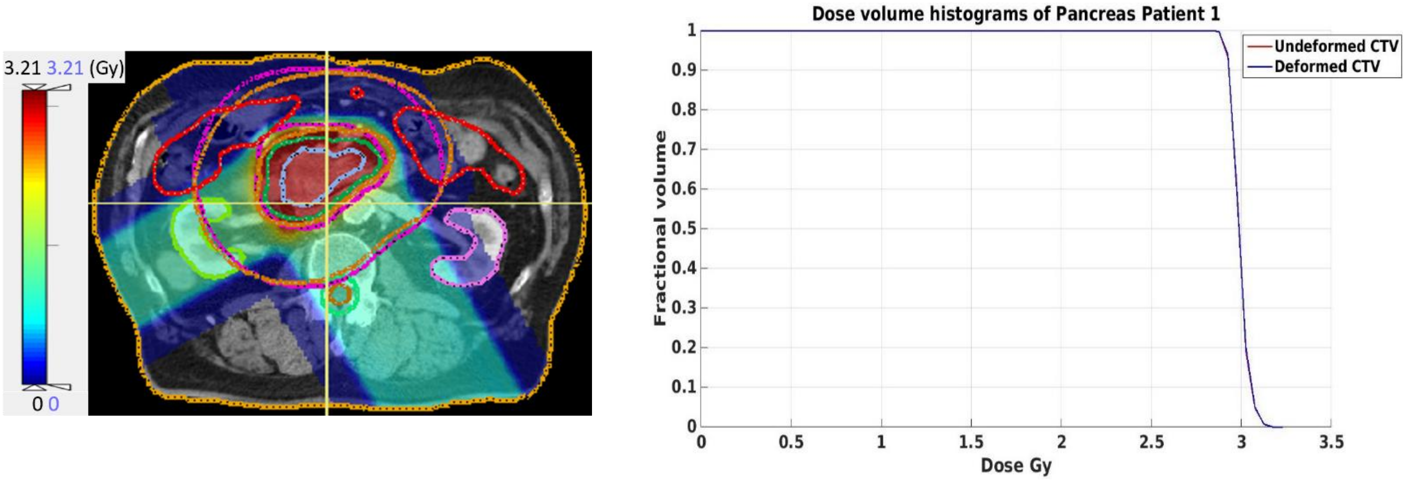

(a) (b)

Figure 59 Dose distribution of deformed scan (on the left) and DVH plot (on the right with red line belonging to undeformed scan and blue line belonging to deformed scan) of Pancreas patient 1

Pancreas Patient 2

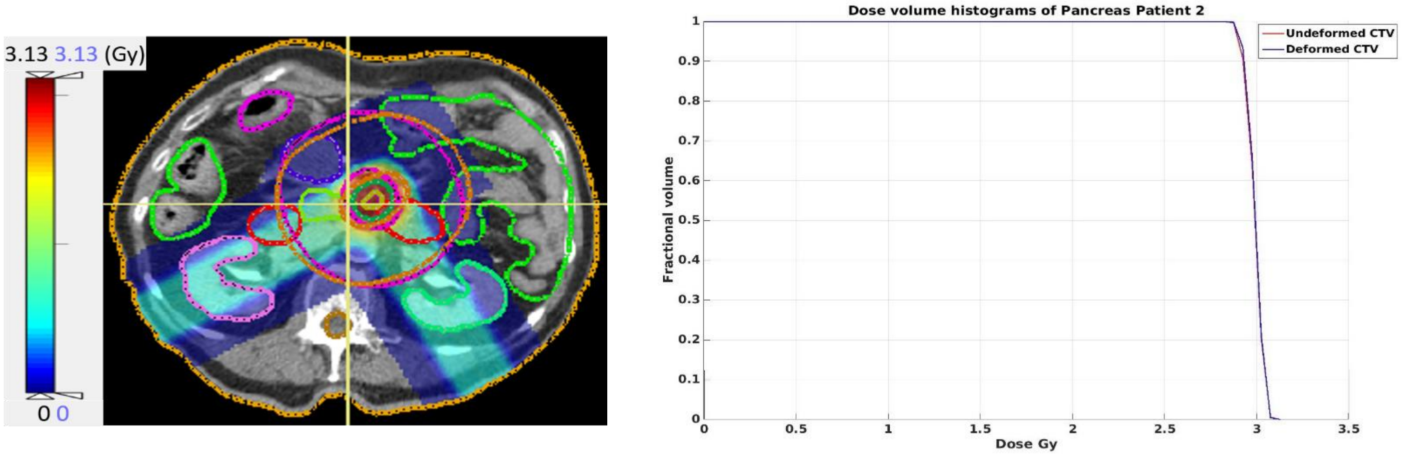

(a) (b)

Pancreas Patient 3

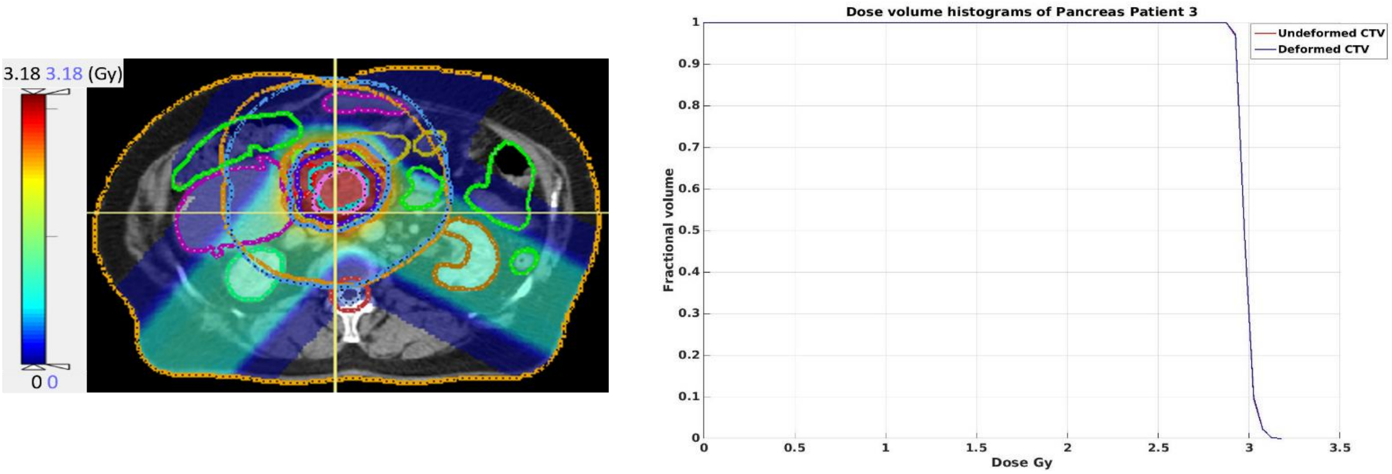

(a) (b)

Pancreas Patient 4

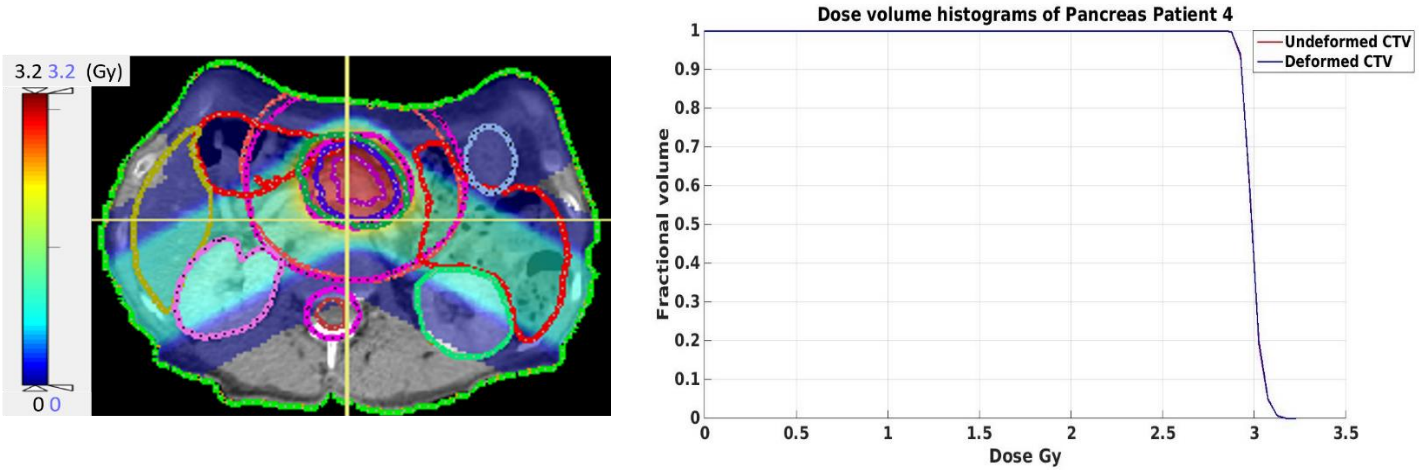

(a) (b)

Figure 60 Dose distributions of deformed scans (on the left) and DVH plots (on the right with red line belonging to undeformed scan and blue line belonging to deformed scan) of Pancreas Patients 2, 3 & 4

12 BIBLIOGRAPHY

Adjeiwaah et al. (2019). Dosimetric impact of MRI distortions: A case study on head and neck cancers. *Int J Radiation Oncol Biol Phys,103(4), 994-1003.*

Agostinelli, S., et al. (2003). Geant4 - a simulation toolkit. *Nuclear Instruments and Methods in Physics Research A, 506, 250-303.*

Baldwin, L. N., Wachowicz, K., & Fallone, B. G. (2009). A two-step scheme for distortion rectification of magnetic resonance images. *Med Phys, 36, 3917-3926.*

Baldwin, L. N., Wachowicz, K., Thomas, S. D., Rivest, R. & Fallone, B. G. (2007). Characterization, prediction, and correction of geometric distortion in 3 T MR images. *Med Phys, 34, 388-99.*

Beavis, A. W., Gibbs, P., Dealey, R. A., & Whitton, V. J. (1998). Radiotherapy treatment planning of brain tumors using MRI alone. *Brit. J. Radiol., 71(845), 544–548.*

Berger, M. (1963). Monte Carlo calculation for the penetration and diffusion of fast charged particles. *Meth. Comp. Phys., 1, pp. 135-215.*

Bernstein, M. A., King, K. F. & Zhou, X. J. (2004). *Handbook of MRI Pulse Sequences.* 1st ed. Burlington, San Diego USA, and London, UK: Elsevier Academic Press.

Bert, C., & Durante, M. (2011). Motion in radiotherapy: particle therapy. *Phys Med Biol 56, pp. R113–R144.*

Bolard, G. & Bulling, S. (2016). MO-FG-CAMPUS-JeP2-03: clinical commissioning of MR-only prostate treatment planning workflow. *Med. Phys., 43(6), 3721.*

Bouilhol, G., et al. (2013). Is abdominal compression useful in lung stereotactic body radiation therapy? A 4DCT and dosimetric lobe-dependent study. *Phys. Med., 29(4), 333-40.*

Chandarana, H., Wang, H., Tijssen, R. H. N. & Das, I. J. (2018). Emerging role of MRI in radiation therapy. *Technol Cancer Res Treat, 14, 298-304.*

Chen, L. et al. (2004). MRI-based treatment planning for radiotherapy: Dosimetric verification for prostate IMRT. *Int. J. Radiation Oncology Biol. Phys., 60 (2), 636-47.*

Chvetsov, A.V., & Paige, S.L. (2010). The influence of CT image noise on proton range calculation in radiotherapy planning. *Physics in medicine and biology, 55(6), N141–9.*

Coutrakon, G., Hubbard, J., Johanning, J., Maudsley, G., Slaton, T., & Morton, P. (1994). A performance study of the Loma Linda proton medical accelerator. *Med Phys. 1994; 21:1691–1701.*

Deasy, J. O., Blanco, A. I., & Clark, V. H. (2003). CERR: A computational environment for radiotherapy research. *Med Phys, 30 (5).*

DeLaney, T. F., & Kooy, H. M. (2008). Proton and Charged Particle Radiotherapy. *Lippincott Williams & Wilkins, vol. 83, 87 pp.*

Desplanques, M. (2015). *An open-source software for proton treatment planning. A dissertation for Doctor of Philosophy.* Politecnico di Milano, Milan.

Dirix, P., Haustermans, K. & Vandecaveye, V. (2014). The value of magnetic resonance imaging for radiotherapy planning. *Semin Radiat Oncol, 24, 151-9.*

Doemer, A. et al. (2015). Evaluating organ delineation, dose calculation and daily localization in an open-MRI simulation workflow for prostate cancer patients. *Radiat Oncol 10 (37).*

Drzymala, R. E., Mohan, R., Brewster, L., Chu, J., Goitein, M., Harms, W., & Urie, M. (1991). Dose-Volume Histograms. *Int. J. Radiation Oncology Biol. Phys., 21, 71-78.*

Edmund, J. M., & Nyholm, T. (2017). A review of substitute CT generation for MRI-only radiation therapy. *Radiat Oncol., 12 (1), 12-28.*

Engelsman, M., & Kooy, H.M. (2005). Target volume dose considerations in proton beam treatment planning for lung tumors. *Med Phys., 32, 3549-3557.*

España, S., & Paganetti, H. (2010). The impact of uncertainties in the CT conversion algorithm when predicting proton beam ranges in patients from dose and PET-activity distributions. *Physics in medicine and biology, 55(24), 7557–71.*

Evans, P.M. (2008). Anatomical imaging for radiotherapy. *Phys Med Biol, 53, pp. R151.*

Eyges, L. (1948). Multiple scattering with energy loss. *Phys. Rev. 74, pp. 1534-1535.*

Fokas, E., Kraft, G., An, H., & Engenhart-Cabillic, R. (2009). Ion beam radiobiology and cancer: Time to update ourselves. *Biochim. Biophys. Acta, 1796.*

Gong, Y., Wang, J., Bai, S., Jiang, X., & Xu, F. (2008). Conventionally-fractionated image-guided intensity modulated radiotherapy (IG-IMRT): a safe and effective treatment for cancer spinal metastasis. *Radiat Oncol., 3(11).*

Guerreiro, F. et al. (2019). Feasibility of MRI-only photon and proton dose calculations for pediatric patients with abdominal tumors. *Phys. Med. Biol., 64.*

Gustafsson, C., Nordström, F., Persson, E., Brynolfsson, J., & Olsson, L. E. (2018). Assessment of dosimetric impact of system-specific geometric distortion in an MRI only based radiotherapy workflow for prostate. *Phys. Med. Biol., 62, 2976–89.*

Haberer, T., Becher, W., Schardt, D. & Kraft, G. (1993). Magnetic scanning system for heavy ion therapy. *Nuclear Instruments and Methods in Physics Research Section A: Accelerators, Spectrometers, Detectors, and Associated Equipment, 330(1-2), 296–305.*

Hong, T. S. et al. (2014). A prospective feasibility study of respiratory gated proton beam therapy for liver tumors. *Pract Radiat Oncol., 4(5), 316–322.*

Huang, K. C., Cao, Y., Baharom, U., & Balter, J. M. (2016). Phantom-based characterization of distortion on a magnetic resonance imaging simulator for radiation oncology. *Phys. Med. Biol., 61 (2).*

International Commission on Radiation Units and Measurements, (1993). Quantities and units in radiation protection dosimetry (Report 51). Retrieved from https://icru.org/home/reports/quantities-and-units-in-radiation-protection-dosimetry-report-51.

International Commission on Radiation Units and Measurements, (1999). Prescribing, recording and reporting photon beam therapy. *ICRU Report 50*.

International Commission on Radiation Units and Measurements, (1993). Prescribing, recording and reporting photon beam therapy. *ICRU Report 62*.

International Commission on Radiation Units and Measurements, (2010). Prescribing, recording and reporting photon-beam intensity modulated radiation therapy. *ICRU Report 83*.

Jaffray, D. A. (2012). Image-guided radiotherapy: from current concept to future perspectives. *Nat Rev Clin Oncol., 9 (12), 688-99.*

Jamtheim Gustafsson, C. (2019). MRI-Only Radiotherapy of Prostate Cancer. Development and Evaluation of Methods to Assess Fiducial Marker Detection, Geometric Accuracy and Dosimetric Integrity. Lund: Lund University, Faculty of Medicine.

Jethwa, K. R. et al. (2018). Initial experience with intensity modulated proton therapy for intact, clinically localized pancreas cancer: Clinical implementation, dosimetric analysis, acute treatment-related adverse events and patient-reported outcomes. *Advances in Radiation Oncology, 3, 314-321.*

Johnstone, E., et al. (2018). Systematic review of synthetic Computed Tomography generation methodologies for use in magnetic resonance imaging-only radiation therapy. *Radiat Oncol Biol Phys., 100(1), 199-217.*

Jonsson, J. (2013). Integration of MRI into the Radiotherapy Workflow. Umeå: Umeå University, Medical Dissertations.

Jonsson, J. H., Johansson, A., Söderström, K., Asklund, T. & Nyholm, T. (2013). Treatment planning of intracranial targets on MRI derived substitute CT data. *Radiother. Oncol., 108, 118–22.*

Kang, Y. et al. (2006). 4D proton treatment planning strategy for mobile lung tumors. *Int. J. Radiation Oncology Biol. Phys., 67(3), 906–914.*

Karotki, A., Mah, K., Meijer, G., & Meltsner, M. (2011). Comparison of bulk electron density and voxel-based electron density treatment planning. *J Appl Clin Med Phys, 12, 3522.*

Keall, P.J., et al. (2006). The management of respiratory motion in radiation oncology report of AAPM Task Group 76. *Med Phys, 33, 3874-3900.*

Keil, E., Trbojevic, D., & Sessler, A. M. (2006). *Fixed Field Alternating Gradient Accelerators (FFAG) for Hadron Cancer Therapy*, Paper presented at the Proceedings of the 2005 Particle Accelerator Conference. 10.1109/PAC.2005.1590871.

Khoo, V. S., Dearnaley, D. P., Finnigan, D. J., Padhani, A., Tanner, S. F., & Leach, M.O. (1997). Magnetic resonance imaging (MRI): considerations and applications in radiotherapy treatment planning. *Radiother. Oncol., 42(1), 1–15.*

Korsager, A. S., Carl, J. & Riis Ostergaard, L. (2016). Comparison of manual and automatic MR-CT registration for radiotherapy of prostate cancer. *J Appl Clin Med Phys, 17, 294-303.*

Kroll, C. A. (2018). Spatial Distortion Artifacts in MR-guided Radiation Therapy, B0 Inhomogeneities, Gradient Nonlinearities and Susceptibility Effects. Munich: Ludwig-Maximilians University, Faculty of Physics.

Kroll, C. et al. (2019). Improving the modeling of susceptibility-induced spatial distortions in MRI-guided extra-cranial radiotherapy. *Phys Med Biol., 64(20).*

Lambert, J. et al. (2011). MRI-guided prostate radiation therapy planning: investigation of dosimetric accuracy of MRI-based dose planning. *Radiother. Oncol. 98, 330–4.*

L'Annunziata. M. F. (2012). Radiation Physics and Radionuclide Decay. In F. M. L'Annunziata (Ed.), *Handbook of Radioactivity Analysis* (3rd ed.). Academic Press.

Lee, E. S. & Lee, J. M. (2014). Imaging diagnosis of pancreatic cancer: a state-of-the-art review. *World J Gastroenterol., 20 (24), 7864-77.*

Lee, Y. K. et al. (2003). Radiotherapy treatment planning of prostate cancer using magnetic resonance imaging alone. *Radiother. Oncol., 66(2), 203–216.*

Lev, M.H., & Gonzalez, R.G. (2002). CT angiography and CT perfusion imaging. In Brain Mapping: The Methods, 2nd edition, Academic Press.

Li, H., Dong, L., Zhang, L., Yang, J. N., Gillin, M. T., & Zhu, X. R. (2011). Toward a better understanding of the gamma index: investigation of parameters with a surface-based distance method. *Med Phys., 38, 6730–6741.*

Liang, X., Li, Z., Zheng, D., Bradley, J. A., Rutenberg, M., & Mendenhall, N. (2019). A comprehensive dosimetric study of Monte Carlo and pencil-beam algorithms on intensity-modulated proton therapy for breast cancer. *J Appl Clin Med Phys., 20, 128– 36.*

Lomax, A.J. (2008a). Intensity modulated proton therapy and its sensitivity to treatment uncertainties 1: the potential effects of calculational uncertainties. *Physics in medicine and biology, 53(4), 1027–42.*

Lomax, A.J. (2008b). Intensity modulated proton therapy and its sensitivity to treatment uncertainties 2: the potential effects of inter-fraction and inter-field motions. *Physics in medicine and biology, 53(4), 1043–56.*

Maes, D., Saini, J., Zeng, J., Rengan, R., Wong, T., & Bowen, S. R. (2018). Advanced proton beam dosimetry part II: Monte Carlo *vs.* pencil beam-based planning for lung cancer. *Trans Lung Cancer Res., 7 (2), 114-21.*

Maintz, J., & Viergever, M. (1998). A survey of medical image registration. *Medical Image Analysis, 2(1):1–36.*

Maspero et al., (2017). Feasibility of MR-only proton dose calculations for prostate cancer radiotherapy using a commercial pseudo-CT generation method. *Phys. Med. Biol. 62, 9159–9176.*

Maspero, M. (2018). MR-only radiotherapy of prostate cancer. (2018). Utrecht: Utrecht University, Graduate School of Life Sciences & Faculty of Medicine.

McGowan, S. E. (2015). *Incorporating Range Uncertainty into Proton Therapy Treatment Planning (Doctoral Thesis)*. University of Cambridge, Cambridge.

Meschini, G. (2015). Integration of Imaging Data and Non-Invasive Measures for the Evaluation of Respiratory Gated Treatments in Particle Therapy. Milan: Politecnico di Milano, Scuola di Ingegneria Industriale e dell'Informazione.

Mohan, R., Grosshans, D. (2017). Proton therapy- Present and future. *Adv Drug Deliv Rev, 109.*

Moyers, M. F., Miller, D. W., Bush, D. A., & Slater, J. D. (2001). Methodologies and tools for proton beam design for lung tumors. *Int J Radiat Oncol Biol Phys, 49(5), 1429-1438.*

National Cancer Institute. (n.d.,a) About Cancer. Retrieved from https://www.cancer.gov/about-cancer.

National Cancer Institute. (n.d.,b) Cancer Types. Retrieved from https://www.cancer.gov/types.

Newhauser, W. D., & Zhang, R. (2009). Calculation of water equivalent thickness of materials of arbitrary density, elemental composition and thickness in proton beam irradiation. *Physics in Medicine & Biology, 54(6).*

Newhauser, W. D., & Zhang, R. (2015). The physics of proton therapy. *Physics in Medicine & Biology, 60(8).*

Nyholm, T., Nyberg, M., Karlsson, M. G. & Karlsson, M. (2009). Systematization of spatial uncertainties for comparison between a MR and a CT-based radiotherapy workflow for prostate treatments. *Radiat. Oncol. 4(54).*

Oh, S, & Kim, S. (2017). Deformable image registration in radiation therapy. *Radiat Oncol J., 35 (2), 101-111.*

Orecchia, R., Zurlo, A., Loasses, A., Krengli, M., Tosi, G., Zurrida, S., & Zucali, P. (1998). Particle beam therapy (hadrontherapy): basis for interest and clinical experience. *European Journal of Cancer, 34(4).*

Owrangi, A. M., Greer, P. B., & Glide-Hurst, C. K. (2018). MRI-only treatment planning: benefits and challenges. *Phys. Med. Biol, 63, 05TR01.*

Paganelli, C., Meschini, G., Molinelli, S., Riboldi, M., & Baroni, G. (2018). Patient-specific validation of deformable image registration in radiation therapy: Overview and caveats. *Med Phys, 45(10), 908-922.*

Paganelli, C., Summers, P., Gianoli, C., Bellomi, M., Baroni G., & Riboldi, M. (2017). A tool for validating MRI-guided strategies: a digital breathing CT/MRI phantom of the abdominal site. *Medical & biological engineering & computing, 55(11), 2001–2014.*

Paganetti, H. (2012). Range uncertainties in proton therapy and the role of Monte Carlo simulations. *Phys Med Biol., 57(11).*

Paganetti, H., Bortfeld, T., Kooy, H. (2005). Proton beam radiotherapy- The state of the art. *The International Journal of Medical Physics Research and Practice, 32(6).*

Park, P. C., Zhu, X. R., Lee, A. K., Sahoo, N., Melancon, A. D., Zhang, L., Dong, L. (2012). A beam-specific Planning Target Volume (PTV) design for proton therapy to account for setup and range uncertainties. *Int J Radiat Oncol Biol Phys., 82(2), 329-36.*

Particle Therapy Co-operative Group. (2019). Facilities in Operation. Retrieved from https://www.ptcog.ch/index.php/facilities-in-operation.

Particle Therapy Co-operative Group. (2019). Facilities under construction. Retrieved from https://www.ptcog.ch/index.php/facilities-under-construction.

Pereira, G.C, Traughber, M. & Muzic, R.F. (2014). The role of imaging in radiation therapy planning: past, present, and future. *Biomed. Res. Int., Article ID: 231090.*

Plastimatch. (n.d.). Retrieved from http://www.plastimatch.org/.

Prabhakar, R., Julka, P. K., Ganesh, T., Munshi, A., Joshi, R. C. & Rath, G. K. (2007). Feasibility of using MRI alone for 3D radiation treatment planning in brain tumors. *Japan. J. Clin. Oncol. 37, 405–11.*

Raldow, A., Lamb, J., & Hong, T. (2019). Proton beam therapy for tumors of the upper abdomen. *Br J Radiol , 92, 20190226.*

Ramsey, C. R. & Oliver, A. L. (1998). Magnetic resonance imaging based digitally reconstructed radiographs, virtual simulation, and three-dimensional treatment planning for brain neoplasms. *Med.Phys.,25(10),1928–1934.*

Roberson, P. L., McLaughlin, P. W., Narayana, V., Troyer, S., Hixson, G. V. & Kessler, M.L. (2005). Use and uncertainties of mutual information for computed tomography/ magnetic resonance (CT/MR) registration post permanent implant of the prostate. *Med Phys, 32, 473-82.*

Rogstrom, K.R., Mills, M.D., & Almond, P.R. (1981). Electron beam dose calculations. *Phys. Med. Biol., 26(3), 445-459.*

Saini, J., Traneus, E., Maes, D., Regmi, R., Bowen, S. R., Bloch, C., & Wong, T. (2018). Advanced proton beam dosimetry part I: review and performance evaluation of dose calculation algorithms. *Trans Lung Cancer Res., 7(2), 171-179.*

Sasidharan, B. K. et al. (2019). Clinical Monte Carlo versus Pencil Beam Treatment Planning in Nasopharyngeal Patients Receiving IMPT. *Int. Journal of Particle Therapy, 5(4), 32-40.*

Schaffner, B., & Pedroni, E. (1998). The precision of proton range calculations in proton radiotherapy treatment planning: experimental verification of the relation between CT-HU and proton stopping power. *Physics in medicine and biology, 43(6), 1579–92.*

Schardt, D., Elsässer, T., & Schulz-Ertner, D S.. (2010). Heavy-ion tumor therapy: Physical and radiobiological benefits. *Reviews of modern physics, 82.*

Schmidt, M.A., & Payne, G.S. (2015). Radiotherapy planning using MRI. *Physics in Medicine & Biology, 60, R323-361.*

Schulte, R., et al. (2004). Conceptual design of a proton computed tomography system for applications in proton radiation therapy. *IEEE Transactions on Nuclear Science, 51(3), 866–872.*

Segars, P., Sturgeon, G., Mendonca, S., Grimes, S., & Tsui, B. M. (2010). 4D XCAT phantom for multimodality imaging research. *Med Phys 37(9), 4902-15.*

Spees, W. M., Buhl, N., Sun, P., Ackerman, J. J., Neil, J. J. & Garbow, J. R. (2011). Quantification and compensation of eddy-current-induced magnetic-field gradients. *J. Magn Reson, 212, 116-23.*

Sun, J. et al. (2015). MRI simulation: end-to-end testing for prostate radiation therapy using geometric pelvic MRI phantoms. *Phys. Med. Biol., 60 (8), 3097.*

Szymanowski, H., Pflugfelder, D., Nill, S., & Oele, U. (2005) Practical implementation of an improved proton dose algorithm for heterogeneous media. *Radiother Oncol, 76, S56.*

Tenhunen et al. (2018). MRI-only based radiation therapy of prostate cancer: workflow and early clinical experience. *Acta Oncol., 57(7), 902-907.*

Turner, J. E. (2007). *Atoms, Radiation and Radiation Protection*. Germany: Wiley-VCH Verlag GmbH & Co. KGaA.

Tyagi, N., et al. (2017). Clinical workflow for MR-only simulation and planning in prostate. *Radiat Oncol, 12, 119.*

Urie, M., Goitein, M. & Wagner, M. (1984). Compensating for heterogeneities in proton radiation therapy. *Phys. Med. Biol., 29, 553–66.*

van Herk, M. (2004). Errors and margins in radiotherapy. *Semin Radiat Oncol, 14, 52-64.*

Vedam, S.S., Keall, P.J., Kini, V.R., Mostafavi, H.,Shukla, H.P., Mohan, R. (2003). Acquiring a four-dimensional computed tomography dataset using an external respiratory signal. *Phys Med. Biol., 48(1), 45-62.*

Veninga, T., Huisman, H., Van Der Maazen, R.W., & Huizenga, H. (2004). Clinical validation of the normalized mutual information method for registration of CT and MR images in radiotherapy of brain tumors. *J Appl Clin Med Phys 5, pp. 66-79.*

Walker, A., Liney, G., Holloway, L., Dowling, J., Rivest-Henault, D. & Metcalfe, P. (2015). Continuous table acquisition MRI for radiotherapy treatment planning: distortion assessment with a new extended 3D volumetric phantom. *Med Phys, 42, 1982-91.*

Walker, A., Liney, G., Metcalfe, P. & Holloway, L. (2014). MRI distortion: considerations for MRI based radiotherapy treatment planning. *Australas. Phys. Eng. Sci. Med. 37 103–13.*

Wegener, D., Zips, D., Thorwarth, D., Weiss, J., Othman, A. E., Grosse, U. Notohamiprodjo, M., Nikolaou, K. & Muller, A. C. (2019). Precision of T2 TSE MRICT-image fusions based on gold fiducials and repetitive T2 TSE MRI-MRI-fusions for adaptive IGRT of prostate cancer by using phantom and patient data. *Acta Oncol, 58, 88-94.*

Weygand, J. et al. (2016). Spatial precision in magnetic resonance imaging-guided radiation therapy: the role of geometric distortion *Int. J. Radiat. Oncol. Biol. Phys. 95, 1304–16.*

Wisenbaugh, E. S., Andrews, P.E., Ferrigni, R.G., Schild, S. E., Keole, S.R., Wong, W.W., & Vora, S.A. (2014). Proton beam therapy for localized prostate cancer 101: basics, controversies, and facts. *Rev Urol., 16(2):67-75.*

Wissmann, L., Santelli, C., Segars. P., Kozerke, S. (2014) MRXCAT: realistic numerical phantoms for cardiovascular magnetic resonance. *J Cardiovasc Magn Reson 16(63).*

Withers, HR. (1985). Biologic Basis for Altered Fractionation Schemes, *Cancer, 55(9): 2086-2095.*

World Health Organization. (2019a). Cancer (Health Topics). Retrieved from https://www.who.int/health-topics/cancer#tab=tab_1.

World Health Organization. (2019b). Cancer (Newsroom). Retrieved from https://www.who.int/news-room/fact-sheets/detail/cancer.

Yan, Y. et al. (2018). A methodology to investigate the impact of image distortions on the radiation dose when using magnetic resonance images for planning. *Phys. Med. Biol., 63.*

Yepes, P., Mirkovic, D., & Taddei, P.J. (2010). A GPU implementation of a track-repeating algorithm for proton radiotherapy dose calculations. *Phys. Med. Biol. 55, 7107-7120.*

Yixiu, K. et al. (2007). 4D Proton treatment planning strategy for mobile lung tumors, *Int. J. Radiation Oncology Biol. Phys*., 67 (3), 906–914.

Zaremba, T., Jakobsen, A. R., Thøgersen, A. M., Oddershede, L., & Riahi, S. (2014). The effect of radiotherapy beam energy on modern cardiac devices: an *in vitro* study. *EP Europace, 16 (4), 612–616.*